

Electronic Spectroscopy of Molecules

OF ASTROPHYSICAL INTEREST

*Towards improving our
knowledge of the DIB carriers*

X L Bacalla

Electronic Spectroscopy of Molecules of Astrophysical Interest

Towards improving our knowledge of the DIB carriers

Lea ...
Hebben een veilige reis!
Tot de volgende keer.

Electronic Spectroscopy of Molecules of Astrophysical Interest

Towards improving our knowledge of the DIB carriers

PROEFSCHRIFT

ter verkrijging van
de graad van Doctor aan de Universiteit Leiden,
op gezag van Rector Magnificus prof. mr. C. J. J. M. Stolker,
volgens besluit van het College voor Promoties
te verdedigen op dinsdag 2 juli 2019
klokke 15:00 uur

door

Xavier L. Bacalla
geboren te Cebu City, Filipijnen
in 1989

Promotiecommissie

Promotores: Prof. dr. Harold Linnartz
Prof. dr. Wim Ubachs (Vrije Universiteit Amsterdam)

Overige leden: Prof. dr. Huub Röttgering
 Prof. dr. Paul van der Werf
 Prof. dr. Andy Ruth (University College Cork)
 Prof. dr. Lex Kaper (Universiteit van Amsterdam)
 Dr. Giel Berden (Radboud Universiteit Nijmegen)

ISBN: 000-00-00000-00-0

© 2019 Xavier L. Bacalla

Cover design by author: Composite image of ‘Lux’ by Johannes Takanen and Walter Runeberg (1894, as part of the monument of Alexander II at the Senate Square in Helsinki) and the panorama of the Milky Way galaxy (ESO / Serge Brunier). Title design with inspiration from the works of Barbara Kruger.

Contents

1	Introduction	1
	The interstellar medium	2
	The diffuse interstellar bands	5
	The ESO diffuse interstellar bands large exploration survey	10
	This thesis	12
2	Cavity-enhanced absorption spectroscopy of plasma jets	15
2.1	Introduction	16
2.2	Cavity-enhanced absorption spectroscopy	17
2.2.1	Incoherent broadband CEAS	18
2.2.2	Cavity ring-down spectroscopy	21
2.3	Plasma production	24
2.3.1	Pinhole- and slit nozzle	25
2.3.2	Electron impact ionization source	27
2.4	Results	28
2.4.1	Optical absorption spectra of a hydrocarbon plasma	28
2.4.2	Optical emission spectra of a hydrocarbon plasma	32
2.5	Summary	35
3	The $B^2\Pi-X^2\Pi$ electronic origin band of $^{13}C_6H$	37
3.1	Introduction	38
3.2	Experiment / method	38
3.3	Results and analysis	39
4	Spectroscopic survey of electronic transitions of the hexatriynyl radical	45
4.1	Introduction	46
4.2	Experiment	47
4.3	Results	49
4.4	Discussion	67

4.4.1	$^2\Pi$ levels	70
4.4.2	$^2\Sigma$ levels	73
4.4.3	Isotope shifts	75
4.5	Conclusion	76
5	Cosmic ray ionization rates in diffuse clouds from near-UV observations of interstellar OH^+	81
5.1	Introduction	82
5.2	Observations and data processing	83
5.3	OH^+ as a probe of the cosmic ray ionization rate	85
5.4	Results	88
5.4.1	Equivalent widths and column densities of OH^+	88
5.4.2	Complementary methods for deriving $N(\text{H}_{\text{tot}})$	92
5.5	Discussion	93
5.6	Conclusions	99
A	EDIBLES targets with very weak OH^+ absorptions	101
B	Compilation of estimates of ζ_p derived from OH^+ detections in the near-UV	103
C	Linear regression results for $N(\text{OH}^+)$	104
D	Compilation of ζ_p -values derived from OH^+ and H_3^+ studies	106
	Bibliography	107
	Summary	123
	Samenvatting	125
	List of publications	127
	Curriculum Vitae	129
	Acknowledgments	131

“There is nothing more deceptive than an obvious fact.”
Sherlock Holmes

CHAPTER 1

Introduction



ESO / Adhemar M. Duro Jr.

The motion of stars and other celestial bodies along the sky has long been used by our ancestors as an indicator of change. Careful tracking of these objects enabled agricultural societies to know, for instance, when it was best to sow seeds for a bountiful harvest. They have served as beacons for navigating on both land and sea. Apart from keeping time and direction, they have also been associated with the divine and were consulted for guiding various forms of human activity. Charting the position of celestial objects has, in many ways, put us in our place in the cosmos. And in the span of recorded history, this has been the whole deal of the study of astronomy.

A major break from the tradition of ‘positional’ astronomy came in the early 1800s, lead by Willam Hyde Wollaston and Joseph von Fraunhofer. They took notice of the dark lines that appear in the spectrum of the sun¹ and cataloged them systemati-

¹ Prior to 19th-century Europe, it was already known that sunlight, when passed through a

cally. Soon thereafter, scientists began to incorporate prisms into their telescopes and pointed these instruments towards other stars which also showed dark lines in their spectra as well as towards the moon and the planets. In the laboratory, various chemicals were burned and the light they gave off was examined through similar prisms that produced unique emission features. With their invention of the spectroscope and an improved flame source around the 1860s, Gustav Kirchhoff and Robert Bunsen were able to deduce a correspondence between the spectrum produced by the flame of burning specific substances and the dark lines found in the solar spectrum—uncovering the material composition of the sun. This development gave rise to a new analytical technique, known as spectroscopy, applicable to atoms and molecules, which has revolutionized the way how astronomy is practiced and has essentially added another set of eyes to the human observer.

Spectrochemical analysis relies on the premise that different substances carry unique spectral signatures. Through the spectroscope, a [hot and] glowing object will produce a continuous spectrum of colors whose intensity is defined by its temperature. A flame will produce bright lines in its emission spectrum with colors (measured in terms of the wavelength of light) which are characteristic of the burning chemical. Likewise, substances such as gases may absorb certain wavelengths from a light source and leave out specific dark lines, producing an absorption spectrum. In the context of astronomical spectroscopy, a star is one example of such light source which produces a combination of a continuous spectrum masked with the absorption (and, in some cases, emission) features from the gases in its atmosphere.² Besides identifying chemical composition, spectroscopy can also be used for determining the star's motion along the line-of-sight, known as its radial velocity. In accordance with the Doppler effect, the absorption lines of a star will shift to longer (red) or shorter (blue) wavelengths depending on whether the star is moving away or towards the observer. For instance, a gravitationally-bound (i.e., mutually orbiting) star system having radial velocity components will exhibit spectral features that oscillate over time along the wavelength scale. With this the spectral signatures of the stars can be discriminated from any other that comes from some intervening material along the sightline. It was through this method that further evidence was found for the existence of an 'interstellar medium', instigated in 1904 by Johannes Hartmann with his discovery of a stationary calcium absorption line in the spectrum of the multiple star system δ Orionis (Mintaka).

The interstellar medium. The interstellar medium (ISM) is an integral component of our galaxy which pervades the space in between the stars. Since the pioneering

prism, disperses into a band of colors commonly known as a 'spectrum' (*pl.* spectra), as seen in a rainbow. In the solar spectrum the features that manifest as dark lines are actually missing colors.

² This has been the basis for the categorization of stars, from the Secchi classes to the Morgan-Keenan classification which is used as the standard today.

work of Hartmann, our knowledge of the ISM has significantly increased with the development of laboratory and astronomical instrumentation, and of [big] data handling and analysis. The ISM is now known to be composed of various environments that result from the close interplay among its main constituents of ordinary matter and [ultraviolet] radiation, cosmic rays (high-energy charged particles), and magnetic fields. A large fraction of its material composition is in the form of atomic and molecular gas (both neutral and ionized) which takes up the bulk of its total mass whereas only about 0.5–1% exists as tiny solid particles of silicate- and carbonaceous dust (Ferrière 2001). The ISM is further divided into generalized ‘phases’ which are based on the kinetic temperature T , number density n , and ionization state of hydrogen, being overwhelmingly abundant, in these interstellar environments (Table 1.1).

Table 1.1: Phases of the interstellar medium (Wooden et al. 2004, Snow & McCall 2006).

ISM component	common name	T [K]	n [cm ⁻³] ^a	A_V ^b	H state ^c
Hot ionized	coronal gas	10 ⁶	0.003		H ⁺
Warm ionized	diffuse ionized gas	10 ⁴	> 10		H ⁺
Warm neutral	inter-cloud H I	10 ³ –10 ⁴	0.1		H ⁰
Cold neutral					
Atomic	diffuse clouds	30–150	1–100	< 0.2	H ⁰
Molecular	diffuse clouds	30–100	100–500	~ 0.2–1	H ⁰ + H ₂
	translucent clouds	15–50	500–5000	~ 1–5	H ₂
	dense/dark clouds	10–50	10 ⁴ –10 ⁶	> 5	H ₂
Mol. hot cores	protostellar cores	100–300	> 10 ⁶		H ₂

^a For molecular environments, n is the density of H₂.

^b Extinction A_V is the absorption and scattering of light traversing through dust and gas particles. The higher the value, the more opaque the environment is to optical/visible wavelengths.

^c Neutral atomic hydrogen is written as H, H⁰, or H I, and its singly-ionized cation as H⁺ or H II.

The predominant state of carbon in the cold medium also distinguishes each cloud type: C⁺ in diffuse, C⁰ in translucent, and CO in dense clouds (Snow & McCall 2006). This division into components, however, curtails the complexity of the ISM as the distribution of interstellar matter is rather continuous, with both rarefied and clumpy regions having no sharp boundary (i.e., exhibiting ‘phase transition fronts’), and is far from homogeneous as different types of clouds could be present along a sightline or even coexist within a single structure. Thermal instability and turbulent processes cause the aggregation and mixing of material that lead to temperature and density fluctuations in the various phases. Nevertheless, the classification can be used for describing the thermodynamic conditions in localized areas of much larger, heterogeneous structures (Vázquez-Semadeni 2012).

As alluded to before, hydrogen constitutes a sizable portion (90.8% by number n , 70.4% by mass m) of the elemental composition of the ISM, followed by helium (9.1% n ; 28.1% m), and trace amounts (0.12% n ; 1.5% m) of heavier elements (labeled in astronomy as ‘metals’) such as oxygen, carbon, and nitrogen which exist in the gas phase and may well be locked up in dust grains; this partition is only slightly different to the ‘cosmic composition’ based on spectral measurements of the sun, stars, and meteorites (Ferrière 2001, Spitzer 1978 p.4). In the cores of the densest and coldest clumps of interstellar material, hydrogen becomes shielded from the ionizing and dissociating ultraviolet radiation of stars which allows for the formation of molecular hydrogen through H recombination on dust grain surfaces (Solomon & Wickramasinghe 1969, Carruthers 1970). Cosmic rays with sufficient energy can penetrate the interior of these clouds and produce H_2^+ , H^+ , and He^+ ; these ions react with abundant neutral species (e.g., CO, O, N, O_2 , N_2) which trigger the synthesis of other ions and complex molecules (Herbst & Klemperer 1973, Smith 2011, Indriolo & McCall 2013). Equally important is the presence of icy mantles on interstellar solid particles that serve as catalytic sites and promote more complex molecule formation which would otherwise take time, if at all, to happen purely in the gas phase in these relatively dilute environments (Allen & Robinson 1977, Tielens & Hagen 1982, Herbst & van Dishoeck 2009, Linnartz et al. 2011, 2015, Öberg 2016). As these dark clouds become larger and denser, the inward self-gravity of the cloud overcomes its outward gas pressure which leads to gravitational collapse – sometimes set off by perturbing forces such as galactic tides or the shockwaves generated from the explosive death of a nearby star (supernova) – giving birth to new stars (Jog 1999). The same supernova provides energy and material enrichment to its surroundings, initiating chemical reactions and spewing out metals which further contribute to the molecular diversity in these interstellar regions. Thus, much more than just a substance where stars are embedded, the ISM also plays a significant role in the processes that govern star and planet formation and in the overall recycling of matter in our galaxy.

Currently circa 200 different molecules³ (McGuire 2018) (excluding isotopologues) have been identified in the ISM or in circumstellar envelopes (i.e., the shell of material surrounding a star that is shed off as it evolves). These range from simple, diatomic species, with CH, CN, and CH^+ being the first molecules detected in space (Swings & Rosenfeld 1937, McKellar 1940, Adams 1941, Douglas & Herzberg 1942), to ‘complex’ molecules of six or more atoms, such as the $c\text{-C}_2\text{H}_4\text{O}$ ring (Dickens et al. 1997), the first detected interstellar anion C_6H^- (McCarthy et al. 2006), the branched $i\text{-C}_3\text{H}_7\text{CN}$ (Belloche et al. 2014), the chiral $\text{CH}_3\text{CHCH}_2\text{O}$ (McGuire et al. 2016), the large fullerenes⁴ C_{60} and C_{70} (Cami et al. 2010), and the C_{60}^+ cation

³ <https://cdms.astro.uni-koeln.de/classic/molecules> (accessed on 6 March 2019).

⁴ Fullerenes are a stable form of molecular carbon having a hollow, cage-like structure (C_{60} , also known as buckminsterfullerene or buckyball, has a shape of a truncated icosahedron, similar to that of a soccer ball) with carbon atoms at the vertices of each pentagonal- and hexagonal face.

(Berné et al. 2013). Inorganic (i.e., non-carbon-based) molecules have been found as well, like OH (Weinreb et al. 1963), H₂O (Cheung et al. 1969), NaCl (Cernicharo & Guélin 1987), and ArH⁺ (Barlow et al. 2013); however, all of the complex ones are organic, which is telling of the propensity of carbon to ‘catenate’ (or link with other C atoms to form a [branched] chain or ring) and the durability of its covalent bonds against the harsh environments of interstellar space. A large majority of these molecules are identified through their characteristic emission features typically at radio and submillimeter wavelengths, and a few are seen in absorption in the infrared (IR), optical/visible, and in the ultraviolet (UV) regions of the electromagnetic spectrum (Menten & Wyrowski 2011). Radio and, to a good extent, optical observations can be done from the ground whereas IR and UV detections largely require space-based telescopes which are free from telluric features⁵ that severely contaminate astronomical spectra. Moreover, it should be noted that firm detections require a set of criteria (see e.g., Herbst & van Dishoeck 2009) and that there still exists a surplus of spectral signatures without a specific chemical (or ‘carrier’) attributed to them. These include the anomalous microwave emission (AME) (Kogut et al. 1996, Leitch et al. 1997), the unidentified infrared emission (UIE) (Russell et al. 1977, Bregman et al. 1983), the extended red emission (ERE) (Cohen et al. 1975, Furton & Witt 1992), and the 2175-Å UV bump in the interstellar extinction curve (Stecher 1965, Cardelli et al. 1989). But perhaps the most enduring of all the unknown features are the diffuse interstellar bands (DIBs)—an enigma that in December of this year (2019) will exactly be 100 years old.

The diffuse interstellar bands. The DIBs (Fig. 1.1) are some 500 absorption features that are observed in the line-of-sight to many stars, whose continuum emission is reddened due to interstellar dust and gas particles.⁶ These features are broader, with full width at half maximum values of around 0.4–23 Å (2–120 cm⁻¹), compared to those produced by interstellar atomic species with FWHM less than 0.1 Å (Hobbs et al. 2009). Some of them (Fig. 1.2), primarily the stronger ones, can be approximated with a Lorentzian lineshape (Snow et al. 2002) or with multiple Gaussian functions (Sonnentrucker et al. 2018) while others have multifaceted structures resembling the band profiles of molecules (Sarre et al. 1995, Galazutdinov et al. 2008). Indeed, the strongest bands first discovered appeared hazy on the edges when recorded using a photographic plate (hence the name ‘diffuse’) which reinforces the hypothesis that the DIB carriers have a molecular nature. DIBs can be found mostly in the cold neutral component of the ISM (diffuse and translucent clouds) and in ex-

⁵ From the Latin *tellus*, or ‘earth’. These are absorption features from the Earth’s atmosphere.

⁶ [Interstellar] reddening is a phenomenon caused by a predominant extinction of short-wavelength visible light which leaves over longer wavelengths and makes a glowing object appear redder than it actually is (related to the reddening of our sun during sunrise and sunset). This is quantified by comparing the object’s observed and hypothetical/true color, known as the astronomical ‘color excess’ E_{B-V} .

tragalactic sources such as the Magellanic clouds (Ehrenfreund et al. 2002), the Andromeda galaxy (Cordiner et al. 2008), and in moderately redshifted ($z \sim 0.5$) objects (Junkkarinen et al. 2004). Some narrow DIBs also seem to converge to the wavelengths and structures of the emission bands seen towards the Red Rectangle nebula (Sarre 1991, van Winckel et al. 2002). Inter-DIB correlation is not strongly pronounced, if at all, (Moutou et al. 1999) which favors the ‘one DIB, one carrier’ hypothesis. On average, they tend to correspond with the amount of reddening, except for lines-of-sight through dense clouds where UV radiation is effectively shielded (also known as the ‘skin-effect’); this observation implies that carrier formation is inhibited in dense cloud interiors and is only concentrated on the edges (Snow & Cohen 1974). Notwithstanding their weak correlation with each other, DIBs may be classified into families of species based on, for example, their intensity ratios among each other (Krelowski & Walker 1987, Cami et al. 1997) or their correlation with the column density of C_2 (Thorburn et al. 2003, Elyajouri et al. 2018). A number of DIBs have also been detected in the near-IR (Geballe et al. 2011, Cox et al. 2014), and much fewer in the UV (Watson 2001, Bhatt & Cami 2015). (For detailed DIB reviews, see also Herbig 1975, 1995, Sarre 2006, Cami & Cox 2014, and Geballe 2016.)

The identification of the DIB carriers has remained elusive for nearly a century now⁷ since the discovery of the first two DIB features ($\lambda\lambda 5780$ and 5797) around the early 1920s by Mary Lea Heger in her PhD work on interstellar sodium.⁸ Around a decade after this serendipitous finding, Merrill (1934), Beals & Blanchet (1937), and Merrill & Wilson (1938), as part of a series of the first systematic investigations on DIBs in the 1930s, confirmed their interstellar nature based on how they remain fixed relative to the wavelength shifts of stellar lines caused by the orbital motion of a stellar binary (as was noticed by Heger) and how their absorption intensities scale generally with distance and amount of reddening (which implies that more of the interstellar material, including those that produce the DIBs, is being probed). Merrill & Wilson proposed micron-sized solid particles as the carrier, because it was already known that dust in interstellar clouds correlated with the reddening of background stars (Trumpler 1930). Clouds containing dust grains that have partially aligned with the interstellar magnetic field contribute a linear and circular polarization to the background starlight (Hall 1949, Hiltner 1949, Davis & Greenstein 1951, Martin et al. 1972); however, no polarization is observed in the DIB features (Walker 1962, Greenberg & Stoeckly 1971, Cox et al. 2011), which is a strong argument against the dust carrier hypoth-

⁷ In 2015, the singly-ionized buckminsterfullerene cation C_{60}^+ was reported as a carrier of two near-IR DIBs ($\lambda\lambda 9577$ and 9632 , approximate central wavelengths in Å) (Campbell et al. 2015) and confirmed by observations using the Hubble Space Telescope (HST) (Cordiner et al. 2019).

⁸ In 1919–1920, Heger measured the spectra of various binary stars, including ζ Persei and ρ Leonis where the two DIBs were seen the strongest. Although she focused primarily on the search for interstellar sodium lines, she was the first to record and notice these DIB features and had it published in 1922. (See McCall & Griffin 2013 for a thorough historical account.)

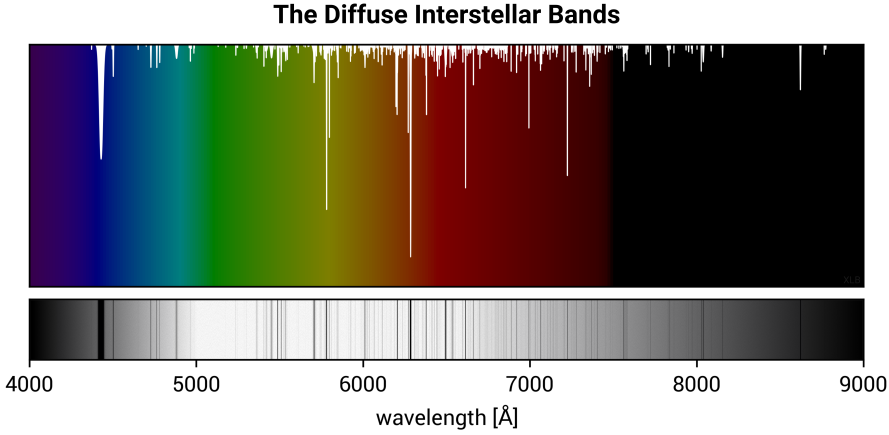


Figure 1.1: DIBs absorption spectrum towards HD 183143 (upper panel, white trace), simulated using band profile measurements from Hobbs et al. (2009). The bottom panel shows an approximation of how these features might have looked like on an exposed photographic plate detector, with the stellar lines removed. The ‘near-IR DIBs’, including the two attributed to C_{60}^+ (Campbell et al. 2015, Kuhn et al. 2016, Cordiner et al. 2019), are not shown. Data available online: <http://dibdata.org/> (accessed on 26 June 2017).

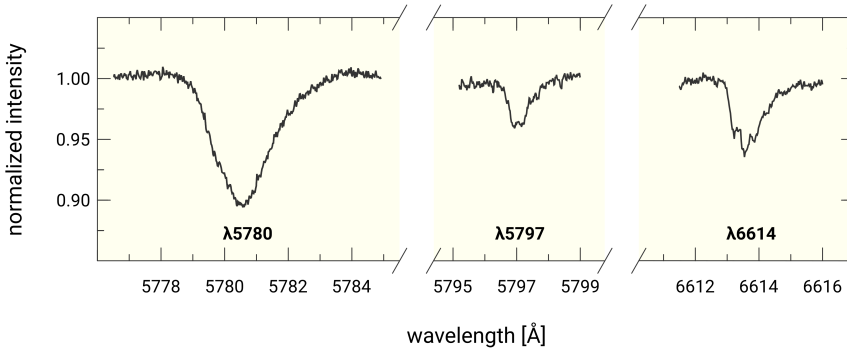


Figure 1.2: Examples of DIB features seen in the spectra toward HD 147165 (wavelength axes are spliced). Notice the difference of their band profiles and the presence of some fine structure, suggesting a molecular origin. *Figure adapted from (Cox et al. 2017).*

esis. One of the other earlier suggestions were simple molecules, which was also stimulated by their recent discovery in the ISM at that time. Candidates such as CO_2 , Na_2 , O^- , C^- , solid O_2 , metastable H_2 embedded in dust grains, CH_4^+ , and NH_4 were put forward on the basis of near coincidences of available laboratory spectra to the DIB wavelengths or on theoretical considerations on the possible features that the molecules would produce (see e.g., [Swings 1937](#), [Saha 1937](#), [McKellar 1960](#), [Herbig 1963](#), and [Herzberg 1967](#)). Likewise, these early proposals did not survive as more results came out from the laboratory as well as from astronomical observations that, for instance, have constrained the interstellar chemical routes that dictate their abundances in these DIB environments. Molecular hydrogen, being an abundant molecule in the ISM, had led [Sorokin & Glowina \(1995\)](#) to propose highly-excited (Rydberg-state) H_2 as a possible carrier, which was complemented with laboratory work ([Ubachs et al. 1997](#)). It remains a challenge, however, to explain the spectroscopic processes necessary to produce these exotic species in the diffuse ISM ([Sorokin et al. 1998](#), [Holmlid 2004](#)).

Overall, free (or unbound) molecules are among the strongest contenders for DIB carriers to date, in contrast to spectra produced in the solid phase which exhibit varying wavelength shifts. The broadness and shape of DIBs may be explained by unresolved lines due to the short lifetime of molecular excitation (e.g., through ‘predissociation’ or ‘internal conversion’) or as a result of unresolved rotational patterns. Attention was given to large molecular carriers after [Danks & Lambert \(1976\)](#) showed that certain spectral parameters for heavier species can be chosen to match the features of a couple of DIBs. For this, [Douglas \(1977\)](#) proposed as carriers the yet-to-be-detected (in the diffuse ISM) bare linear carbon chains of 5–15 atoms, as these would produce bands in the visible region⁹ and would be protected from UV photodissociation through radiationless transitions between their energy states. Around this time, carbon chains of a different variety (cyanopolynes and monohyrides / carbon chain radicals and ions) were also detected in dense clouds and circumstellar envelopes through their rotational transitions in (sub)millimeter and IR wavelengths. Experimental work to support [Douglas’](#) idea was initiated by [Krätschmer \(1986\)](#), albeit done with solid matrices which induced wavelength distortions. Subsequent studies employed similar matrix-isolation techniques together with time-of-flight mass spectroscopy to record the electronic spectra of these exotic molecules. Gas-phase laboratory spectra came later with the development of molecule production such as using hollow cathode discharges, supersonic plasma expansions, and electron-impact ionization sources that were coupled with sensitive detection schemes, including, but not limited to, cavity ring-down (CRD), laser-induced fluorescence (LIF), and two-color resonant photodetachment spectroscopy. (See [Nagarajan & Maier 2010](#) for a list of carbon chains that have been studied and the corresponding references.) This now allowed for a direct comparison of laboratory data on carbon chains to astronomical spectra, which re-

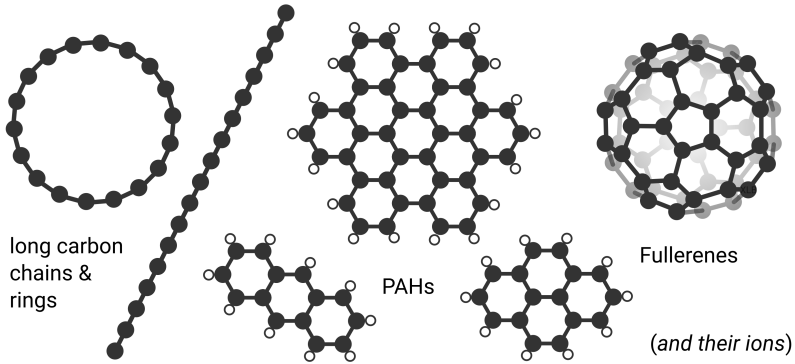
⁹ As the molecule becomes larger (or longer, in the case of linear carbon chains), its (fundamental) electronic transitions situate to the red or at longer wavelengths.

sulted in many data that, in the end, were proven not to match DIB features. Notable examples of near identifications include the C_7^- anion (Tulej et al. 1998) with at least five bands coinciding with DIBs (this was dismissed through follow-up high-resolution astronomical observations by McCall et al. 2001), the NC_4N^+ cation with a rotational contour that looks similar but is slightly offset compared to the double-peaked $\lambda 5959$ DIB (Motylewski et al. 2000), a then newly detected DIB at 5069 \AA attributed to HC_4H^+ (Krełowski et al. 2010b) which was refuted by arguments on band profile mismatch (Maier et al. 2011b), and the $I-C_3H_2$ chain having two features coincident with the $\lambda 44881$ and 5450 DIB (Maier et al. 2011a) which was quickly challenged for discrepancies in its band intensity ratio that yielded an anomalous abundance in comparison to what is derived from the DIBs themselves (Krełowski et al. 2011) and from its observed interstellar abundance (Liszt et al. 2012). These investigations have led to the conclusion that small chains containing ≤ 12 carbon atoms are not responsible for at least the strongest of the DIB features; longer bare carbon chains and rings still qualify as candidates (Jochnowitz & Maier 2008, Rice & Maier 2013).

Another class of organic molecules of interest are the polycyclic aromatic hydrocarbons (PAHs) which are made up of carbon atoms arranged in a honeycomb-like lattice that are terminated by hydrogen atoms on the edges. These molecules were first proposed as potential DIB carriers by van der Zwet & Allamandola (1985), Leger & d’Hendecourt (1985), and Crawford et al. (1985), owing to their tenacity to UV photodissociation and, consequently, their relative high abundance in the ISM as inferred from their ‘collective’ mid-IR emission (with Puget et al. 1985 and Allamandola et al. 1985 attributing the ubiquitous UIR bands to the PAHs), and for their ions to exhibit their ‘species-specific’ absorption features in the DIB wavelength range. Laboratory data in both the solid- and gas-phase are available (Salama et al. 1999, 2011, and references therein); however, this has not yielded a convincing match with the DIBs. Much of these individual PAH signatures are still being searched for in space in the visible and UV which also adds to the challenge of pinning down a unique PAH-DIB carrier. The detection of interstellar naphthalene ($C_{10}H_8^+$) and anthracene ($C_{14}H_{10}^+$) cations by Iglesias-Groth et al. (2008, 2010) towards one star was contested by Searles et al. (2011) and Galazutdinov et al. (2011) and remains an open issue.

Alongside the PAH-DIB hypothesis, the fullerene family (C_{60} , C_{70} , their ions and derivatives) is also considered as an attractive solution to the DIB mystery, being a stable configuration of carbon that is highly robust against photofragmentation (Kroto 1987, Leger et al. 1988, Kroto & Jura 1992). These carbon cages have been detected in space through their mid-IR emission in planetary nebulae and star-forming regions (see e.g., Cami et al. 2010, Sellgren et al. 2010) and, much recently, in the diffuse ISM (Berné et al. 2017). Results from matrix experiments (Fulara et al. 1993a) had led Foing & Ehrenfreund (1994, 1997) to [inconclusively] attribute two bands of the C_{60}^+ cation to a then new pair of near-IR DIBs at $\lambda 9577$ and 9632 on the basis of a comparably consistent band separation and intensity ratio. This finding was later con-

DIB carrier candidates



firmed by [Campbell et al. \(2015\)](#) using a helium atom-tagging technique that allowed for an extrapolation of the gas-phase electronic spectrum, in addition to finding three more absorption bands, of C_{60}^+ ([Campbell et al. 2016a,b](#)). A similarly indirect measurement using ultracold helium droplets corroborated the tagging experiment ([Kuhn et al. 2016](#), [Spieler et al. 2017](#)). Follow-up astronomical observations have revealed DIBs corresponding to the newly recorded electronic bands ([Walker et al. 2015, 2016](#)), which were questioned ([Galazutdinov et al. 2017](#), [Galazutdinov & Kr  owski 2017](#)) and defended ([Walker et al. 2017](#)) on grounds of telluric pollution and inconsistent band intensity ratios. Clearly, more [space-based] observations are needed to settle the matter ([Cordiner et al. 2017](#), [Lallement et al. 2018](#)). In the most recent HST study ([Cordiner et al. 2019](#)) it has been possible now to identify two of the weaker C_{60}^+ bands, besides the two already known stronger bands, and proof is accumulating that C_{60}^+ is indeed a DIB carrier. This does not explain, however, how such large species can form under the harsh conditions in the diffuse interstellar medium.

Other candidates have also been suggested based on calculated electronic transitions, such as tubular PAHs (carbon nanotubes) ([Zhou et al. 2006](#)), the CH_2CN^- anion ([Cordiner & Sarre 2007](#)), and proflavine and its ions ([Bonaca & Bilalbegovi   2010](#)), which all still await confirmation from laboratory spectroscopy. The current consensus favoring carbon-based molecules (and setting aside the other candidates) has definitely benefited from the synergy of observational, experimental, theoretical, and computational work. As our knowledge of the DIBs broadens, the criteria become more stringent (see e.g., [Snow 2014](#)) for better constraining the seemingly overwhelming possibilities of molecular combinations and arrangements of potential DIB candidates.

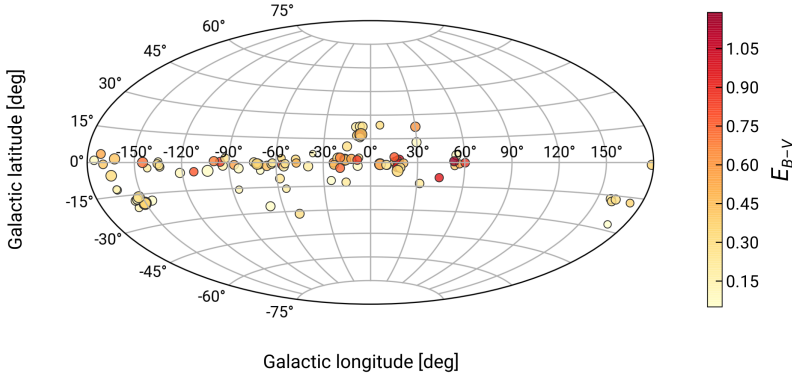


Figure 1.3: Distribution of EDIBLES sightlines in the Milky Way. The color spectrum corresponds to the reddening index (color excess) of the target star and the symbol size is determined by the total-to-selective extinction ratio $R_V (= A_V/E_{B-V})$; this parameter describes the dust grain size distribution along the sightline). *Figure adapted from Cox et al. (2017).*

The ESO Diffuse Interstellar Bands Large Exploration Survey (EDIBLES). It comes as no surprise that the total number of DIBs discovered rose markedly with the advancement of instrumentation (telescope optics, dispersion media, detection and recording means), offering a much higher signal-to-noise ratio and spectral resolution, as well as the implementation of accurate models for better telluric correction, especially that most of the research on DIBs is done using ground-based, optical telescopes. In the past half century or so, many sky surveys have been made not only to search for DIBs but also to determine how their behavior can be dictated by the physical and chemical properties of the environments where they are seen (or vice versa) to constrain, if not eventually identify, the carriers. Most of these were dedicated to either focus on a few of the strongest DIBs towards a large sample of sightlines (e.g., [Friedman et al. 2010](#), [Yuan & Liu 2012](#), [Puspitarini et al. 2015](#)), or to survey many DIBs in just a few targets (e.g., [Jenniskens & Désert 1994](#), [Hobbs et al. 2009](#)). A relatively recent observational program called the European Southern Observatory (ESO)–Diffuse Interstellar Bands Large Exploration Survey (EDIBLES) was undertaken to complement these previous surveys, with the best of both worlds – studying many DIB features towards many sightlines – in order to better infer the [molecular] characteristics of the carriers by utilizing a statistically significant data set ([Cox et al. 2017](#)).

EDIBLES is a large (250+ hr) ‘filler’ program (ESO ID 194.C-0833, PI. N.L.J. Cox) using the Ultraviolet and Visible Echelle Spectrometer of the Very Large Telescope (VLT-UVES) in Paranal, Chile, implemented to observe the spectra of early-

type (hot and bright) stars along the Galactic plane (Fig. 1.3) that probes the diffuse- and translucent ISM. (For more details and project goals, see Cox et al. 2017 and Cami et al. 2018.) A total of 123 unique sightlines are targeted and, as of April 2019, over 90% have been observed. To briefly summarize the survey design: four standard configurations of UVES (Dekker et al. 2000) are employed, with wavelength settings centered at 3460, 4370, 5640, and 8600 Å, covering from about 3042 to 10 420 Å. It offers a high spectral resolution of $\sim 70\,000$ ($\sim 100\,000$) in the blue (red) arm and a high signal-to-noise ratio (S/N) with a median value of around 500–1000. These specifications make EDIBLES a versatile data set to not only detect and study the DIBs but also to include other interstellar features such as C_2 and CN (and in particular, OH^+ ; Chap. 5 in this thesis) which can be used as additional diagnostics for the physical and chemical conditions (e.g., the Galactic cosmic-ray ionization rate) in the DIB environment.

★

It may well be haphazard to argue that telescopes ought to have more powerful optics for better light collection to detect more of the weak DIBs, and the spectrometers used in conjunction with them be of a much higher resolution than what is currently achievable; the technological demands involved for these improvements are quite *astronomical*. While this is undoubtedly important in knowing more about the DIBs and their carriers, high-sensitivity and high-resolution electronic spectroscopy in the laboratory provides us with accurate molecular parameters that we can use for modeling temperature-dependent band profiles, and inferring the presence of much weaker signatures to compare with (and even guide) astronomical observations.

This thesis

In the next chapters, I will present the results of my PhD work that revolves around the goal of understanding the DIB problem, involving laboratory spectroscopy and observational analysis.

Chapter 2 describes the experimental techniques that I have employed in recording spectra specific to the study of carbon-chain radicals. These are namely Incoherent Broadband Cavity-Enhanced Absorption Spectroscopy (IBBCEAS) and Cavity Ring-Down Spectroscopy (CRDS). The two methods are used in a complementary fashion; combining the advantage of the fast data acquisition and wide wavelength coverage of IBBCEAS together with the high resolution of CRDS ensures an efficient search and identification of [new] spectral features that may be directly compared with astronomical DIB spectra. Details on the synthesis of molecules through hydrocarbon plasma expansions are also provided.

Chapters 3 and 4 focus on the hexatriynyl radical, C_6H and its heavier isotopologue, $^{13}C_6H$. The C_6H carbon chain was first found in space (Suzuki et al. 1986) before its spectra was even recorded in the laboratory (Pearson et al. 1988) using

millimeter-wave spectroscopy. Despite failing the criteria for a DIB carrier, the electronic spectrum of this molecule is rich with information unraveled using high-resolution CRDS which can nevertheless provide insight on how, for instance, band profiles can change with subtle intramolecular interactions. In these contributions, the electronic origin band of $^{13}\text{C}_6\text{H}$ is reported for the first time, and an extensive energy level scheme for C_6H is formulated on the basis of rovibronic assignments and literature data (mm-wave, matrix isolation, and hollow-cathode spectra, ab-initio calculations, and isotopic substitution). Additionally, a Renner-Teller analysis is invoked to explain and assign the different electronic transitions.

Finally, in Chapter 5, electronic transitions of the hydroxyl cation OH^+ are searched for in astronomical spectra from the ESO Diffuse Interstellar Bands Large Exploration Survey (EDIBLES). The interstellar abundance of OH^+ is quantified and from this the rate of cosmic-ray ionization (CRI) in diffuse-translucent clouds is inferred. This quantity is especially important for modeling the chemical evolution of various interstellar species in these environments which may well include the molecular DIB carriers (see e.g., [Lepp et al. 1988](#)). It is found in this contribution that the rates are higher than what was previously derived through submillimeter, infrared, and UV observations. This is due to a revised formulation of the OH^+ abundance – CRI rate relation using updated oscillator strength values for the OH^+ transitions. It is possible, however, that these sightlines have inherently high concentrations of OH^+ , and thus, lead to a high rate of CRI derived. Nevertheless, the results serve as a complementary check to other methods of deriving the CRI rate, using ground-based observations of multiple OH^+ transitions in the UV.

CHAPTER 2

Cavity-enhanced absorption spectroscopy of plasma jets

The different laboratory spectroscopic techniques used in this thesis are presented in this chapter. The concept of absorption spectroscopy is introduced, where the basic requirements needed to record a spectrum are laid out. The two methods employed here, known succinctly as IBBCEAS and CRDS, both utilize an optical cavity which greatly enhances the sensitivity in detecting short-lived and reactive molecules. In the context of this thesis, the former is best used in making a survey for [new] spectral features, as it is fairly sensitive and can cover a wide wavelength range in a short amount of time for each measurement run, while the latter, offering a much higher spectral resolution, is utilized in zeroing-in on these absorption features to further unravel structural details. From a precursor gas mixture, the chemical species of interest are synthesized using plasma nozzles which produce supersonic jets of radicals and ions in the gas phase. Here, several conceptually different plasma nozzle systems will be described. Species formed in the resulting plasma expansions can be identified using, for example, rotational constants and vibronic energy differences which can be obtained by analyzing the recorded spectra. Searching in the laboratory for potential carriers of unidentifiable features from astronomical surveys, such as the diffuse interstellar bands, can thus be efficiently implemented using IBBCEAS and CRDS—two complementary measurement schemes that will be described shortly.



This chapter describes a work in preparation for publication.

2.1 Introduction

The basic ingredients for a direct spectroscopic absorption experiment include a source of radiation, a light-dispersing medium for generating a spectrum, an absorbing material (i.e., the sample to be analyzed), and a detector. The Beer-Lambert (or Beer-Lambert-Bouguer) law for the absorption of light states that the higher the concentration of the sample and the longer the path that light travels through it, the more the light gets absorbed.¹ For a particular measurement a high signal-to-noise ratio (S/N) can be obtained by increasing the sample density and/or the effective absorption pathlength; this, however, is not always possible. One practical solution would be to contain the sample inside an optical cavity (the absorption cell) and have the light pass through the sample more than once. Mirror configurations that allow for multipass absorption already exist – the Pfund cell (invented by August Pfund in the late 1930s), the White cell (White 1942), the Herriott cell (Herriott & Schulte 1965), the circular multipass cell (Thoma et al. 1994), and other variations that rely on precise laser beam patterns on the mirrors (Kaur et al. 1990, McManus et al. 1995) – and these have their own utility depending on the application and/or the design constraints of the experiment. These are typically challenging to set up, since they require that the light beams be spatially separated which consequently demand larger mirrors, and some have mirror holes precisely aligned to let the light in or out. With the advent of mirror coating techniques (e.g., evaporative deposition, ion-beam sputtering)² that can achieve reflectivities of more than 99.9%, an optical cavity can now be constructed with only two mirrors sharing a single optical axis which simplifies the configuration and alignment procedure. Light enters the cavity through one of the cavity mirrors and exits through the other. The high reflectivity essentially enables the light to be trapped in between the two mirrors for a much longer time, and thus for a much longer total travel path. If an absorbing sample is contained in this cavity, the total absorption from the injected light is compounded significantly as the trapped light bounces back and forth through the sample. Using this technique, a typical sample length of a few centimeters can have an effective absorption path length of up to a few kilometers. This is the basic concept behind cavity-enhanced absorption spectroscopy (CEAS). (For a comprehensive review of the principle and development of CEAS and its various techniques, see, e.g., Berden et al. 2000, Berden & Engeln 2009, Romanini et al. 2014.)

¹ $A = \sigma(\lambda)nl$, where A is the absorbance, $\sigma(\lambda)$ is the absorption cross section [cm^2] of the sample for a particular wavelength λ , n is the number density [cm^{-3}], and l is the pathlength of light through the sample [cm]. This linear relationship only holds true for as long as the absorption is small enough so as not to cause optical saturation which can lead to stimulated emission.

² Traditionally, through the process of ‘silvering’, a thin coat of metal such as aluminum, copper, silver, or gold is applied onto a glass substrate, producing mirrors with average reflectivities of 80–99% in the visible region.

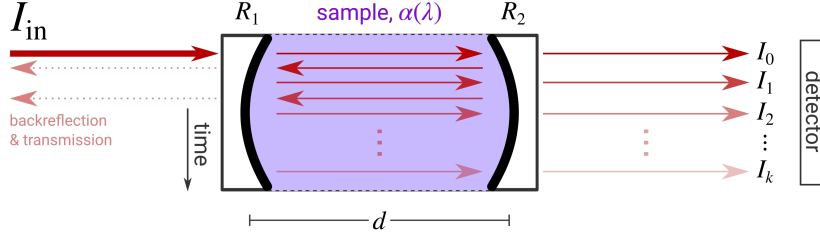


Figure 2.1: Schematic of the CEAS configuration. In reality, the light rays lie along the optical axis of the cavity; they are separately drawn to denote their temporal evolution.

2.2 Cavity-enhanced absorption spectroscopy

When monochromatic light of intensity I_{in} passes through a sample of length l with a wavelength-dependent absorption ‘strength’ denoted by the coefficient $\alpha(\lambda)$, the output intensity I_{out} follows

$$I_{\text{out}} = I_{\text{in}} e^{-\alpha(\lambda)l}, \quad (2.1)$$

which is assumed to be within the linear regime of the Beer-Lambert law. As was described above, the absorption can be enhanced by containing the sample in a stable optical cavity comprised of two mirrors, each with reflectivities R_1 and R_2 separated by a distance d . Although the sample may span the whole length of the cavity ($l = d$), in some cases as with the supersonic plasma jets studied in this thesis, $l < d$; the former is adopted for simplicity in the formulation.

Figure 2.1 depicts a schematic of the CEAS multipass configuration. After the first pass through the sample, the light intensity detected at the exit end of the cavity is

$$I_0 = I_{\text{in}}(1 - R_1) e^{-\alpha d}(1 - R_2). \quad (2.2)$$

The terms $(1 - R_1)$ and $(1 - R_2)$ set the fraction of light transmitted through each of the mirrors. It is assumed here that other loss mechanisms, such as absorption and scattering in the mirror substrate and the sample container walls, are much smaller than what is limited by the mirror reflectivities. The first internally-reflected light inside the cavity will have an intensity equal to $I_{\text{in}}(1 - R_1) e^{-\alpha d} R_2$, and will further take a factor of $e^{-\alpha d} R_1 e^{-\alpha d}(1 - R_2)$ after completing one round-trip (two passes). It is straightforward to show that for each round-trip until the k th time following the first pass, the detected intensity becomes

$$\begin{aligned}
I_1 &= I_{\text{in}}(1 - R_1) e^{-\alpha d} R_2 e^{-\alpha d} R_1 e^{-\alpha d} (1 - R_2) \\
I_2 &= I_{\text{in}}(1 - R_1) e^{-\alpha d} R_2 e^{-\alpha d} R_1 e^{-\alpha d} R_2 e^{-\alpha d} R_1 e^{-\alpha d} (1 - R_2) \\
&\vdots \\
I_k &= I_{\text{in}}(1 - R)^2 e^{-\alpha d} (R e^{-\alpha d})^{2k} = I_0 (R e^{-\alpha d})^{2k},
\end{aligned} \tag{2.3}$$

with R as the ‘effective’ reflectivity equivalent to the geometric³ mean $\sqrt{R_1 R_2}$. From this it is clear that for a particular sample the enhancement of the absorption solely depends on the mirror reflectivities, as this determines the number of passes achievable. For an empty cavity (i.e., $\alpha = 0$), Eq. 2.3 becomes $I_k = I_{\text{in}}(1 - R)^2 R^{2k}$. To obtain a spectrum, the detected⁴ intensity of light transmitted through the cavity with and without an absorbing medium is compared, and is then plotted with the wavelength of light. The two CEAS methods used in this thesis, namely Incoherent BroadBand Cavity-Enhanced Absorption Spectroscopy (IBBCEAS) and Cavity Ring-Down Spectroscopy (CRDS), can be distinguished by how these detected intensities of light are handled and analyzed. Each technique will be described in the succeeding sections.

2.2.1 Incoherent broadband CEAS

The principle of Incoherent BroadBand Cavity-Enhanced Absorption Spectroscopy (IBBCEAS) was first developed and demonstrated by Fiedler et al. (2003) (see also Fiedler 2005 and references therein for a detailed theory on the discussion below). In this method, incoherent broadband light is coupled into the optical cavity, and the transmitted light is integrated through the detector. Although the formulation above was made for monochromatic light, this can readily be extended to all frequencies in accordance to the superposition principle. For each wavelength λ , the total detected intensity is the sum of all transmissions through the exit mirror, that is,

$$I_{\text{out}} = \sum_{k=0}^{\infty} I_k = I_{\text{in}}(1 - R)^2 e^{-\alpha d} \sum_{k=1}^{\infty} (R e^{-\alpha d})^{2k}. \tag{2.4}$$

With $R \rightarrow 1$ the summation converges and Eq. 2.4 can be expressed as

$$I_{\text{out}} = I_{\text{in}} \frac{(1 - R)^2 e^{-\alpha d}}{1 - (R e^{-\alpha d})^2}, \tag{2.5}$$

³ Compared to the arithmetic mean, taking the geometric mean will prevent the larger of the two reflectivities to dominate the ‘effective’ value. Source: <https://www.landonlehman.com/post/the-geometric-mean/> (accessed on 8 April 2019).

⁴ The attenuated signal after the k th round-trip should be above the noise level of the detector.

and for an empty cavity,

$$I_{\text{out}}^0 = I_{\text{in}} \frac{1 - R}{1 + R}. \quad (2.6)$$

These intensities are measured simultaneously for each wavelength dispersed at a given moment, and a spectrum is generated by taking the ratio of the detected intensities with and without the absorbing medium. The spectral resolution, largely determined by the monochromator used in dispersing the light, is moderate compared to laser-based techniques such as CRDS (Sec. 2.2.2). However, in the case of diffuse interstellar bands research, the somewhat lower spectral resolution is no issue, as DIBs tend to be broad and unresolved. In addition, a substantially wider spectral coverage can be achieved with IBBCEAS for a much shorter measurement time since less reflective mirrors are used (compared to those in CRDS) which can be manufactured with a wider bandwidth.

The IBBCEAS setup (Figs. 2.2 and 2.3; also known as the BroadBand – Diffuse Interstellar Bands setup or BB-DIB; [Walsh et al. 2013](#)) in the Sackler Laboratory for Astrophysics at Leiden Observatory is comprised of, first and foremost, a 300-W xenon arc lamp (LOT, LSB530; Ushio, UXL-302-0) which simultaneously provides light across the entire visible spectrum, with an extended coverage towards the UV and the near-IR region (200 nm – 2.5 μm). This light is collimated through a telescope assembly and coupled into an optical cavity (with two mirrors of $R \gtrsim 99.95\%$) that contains the absorbing material; typically a hydrocarbon plasma jet is positioned. (Details on the production of the pulsed plasma jet will be described in the subsequent sections.) Light leaking out of the cavity is collected by means of a circular-to-rectangular fiber optic bundle (LOT, LBB552) that directs it through the entrance slit (13 μm) of a Czerny-Turner-type spectrograph (Andor, Shamrock 750). Inside the spectrograph, a grating (1800 lines/mm; spectral resolution of 0.03 nm) held on a turret disperses the light and projects a wavelength range of 20 nm at a time onto a charge-coupled device (CCD) array (Andor, Newton) of 2048×512 pixels. The pixels provide an absolute wavelength accuracy of 0.1 Å which is sufficient for comparing with the best-resolved DIB features. To record a spectrum, the light reaching the CCD is integrated over time using various settings for exposure, readout rate, number of accumulated exposures, etc., depending on the application while also avoiding saturation of the pixels and the A/D converter. Typically, every column of CCD pixels is binned together to generate a one-dimensional spectrum of photoelectron counts versus the wavelength of light. After each measurement of an absorption signal, a reference spectrum is taken without the plasma jet which is used for subtracting/dividing the lamp and cavity transmission continuum from the signal. Wavelength calibration is made possible by separately recording an emission spectrum from a mercury or sodium discharge lamp. In addition, atomic emission lines (e.g., Ar^+) from the plasma glow, if present, can also be used for this purpose. An interference filter is placed before the fiber optic bundle to further block off most of the emitted light from the plasma (and the Xe arc lamp) that is outside the wavelength range for which the cavity mirrors

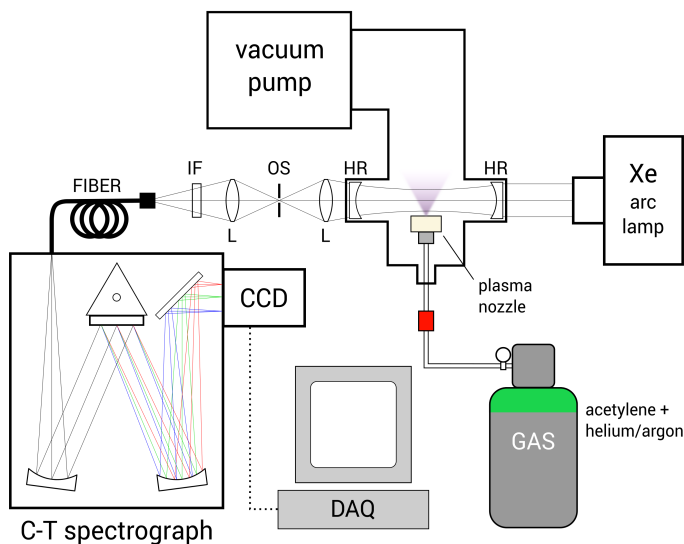


Figure 2.2: Block diagram of the IBBCEAS setup at the Sackler Laboratory for Astrophysics in Leiden. High-reflectivity mirror (HR); lens (L); optomechanical shutter (OS); interference filter (IF); Czerny-Turner (C-T) spectrograph; charge-coupled device (CCD); data acquisition interface (DAQ).

have R -values above 99.95%. The mirrors used (e.g., Research Electro-Optics Inc., Layertec) typically only offer less than 100 nm of wavelength bandwidth, and thus, was replaced accordingly to cover as much of the visible spectrum.

It should be noted that the lamp produces continuous-wave (cw) radiation whereas the plasma jet comes in 1–2-ms pulses at 25 Hz. This means that an absorption signal can only be present whenever light coincides in time with the plasma jet, and so, the CCD also gets exposed to light that does not contain any signal at all (the data acquisition duty cycle is much less than one). As a consequence, the S/N lowers and the sensitivity of the measurement decreases. To mitigate this, the light transmitted through the exit mirror of the cavity is focused through the slot of an optomechanical shutter (Stanford Research Systems, SR540) that is synchronously referenced to the repetition rate of the plasma pulse to cut off the light which does not carry any spectral information. Furthermore, the CCD is cooled using a thermoelectric cooler (bringing its temperature down to -70°) to minimize the electronic noise due to its inherent dark current.

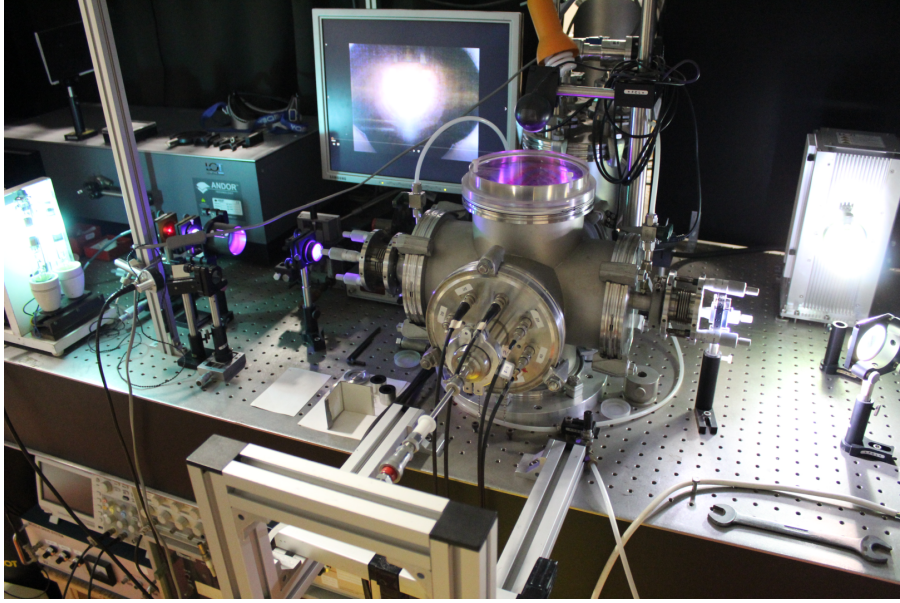


Figure 2.3: The BB-DIB setup in the Sackler Laboratory for Astrophysics at Leiden Observatory.

2.2.2 Cavity ring-down spectroscopy

The other technique known as [pulsed] Cavity Ring-Down Spectroscopy (CRDS), first demonstrated by O’Keefe & Deacon (1988), employs a laser which can be tuned across a certain wavelength range. Instead of integrating the intensity of the exiting light as in IBBCEAS, its attenuation is measured in time as it bounces from one to the other mirror (Fig. 2.4). Building from the previous formulation in Sec. 2.2, it can be shown that the time t elapsed for k round-trips is $t = 2dk/c$, where c is the speed of light. Equation 2.3 can now be expressed⁵ as

$$I(t) = I_0 \exp\left[\frac{ct}{d} (R - 1 - \alpha d)\right]. \quad (2.7)$$

The intensity of light decays exponentially, hence the term ‘ring-down’. The time when I_0 has decreased by a factor of $1/e$ is the characteristic ring-down time τ which is defined as

$$\tau = \frac{d}{c(1 - R + \alpha d)}, \quad (2.8)$$

⁵ Note that $\ln(x) \approx (x - 1)$ as $x \rightarrow 1$ and $e^{\ln(x)} = x$.

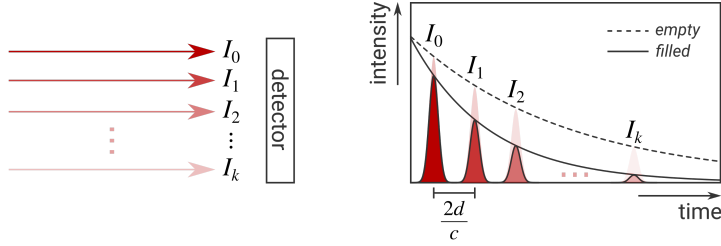


Figure 2.4: Continued from Fig. 2.1. The exponential decrease in light intensity is measured in CRDS. (The roundtrip time for one laser pulse is equal to twice the cavity length d divided by the speed of light c .) The ring-down time for light in a cavity with an absorbing sample decays faster than for an empty one; this characteristic time is determined and plotted for each wavelength to obtain an absorption spectrum.

and for an empty cavity,

$$\tau^0 = \frac{d}{c(1 - R)}. \quad (2.9)$$

Equation 2.9 can be used for accurately calculating mirror reflectivities, as was done in the first conceptualization of the CRD technique (Crawford 1985). To extract the ring-down time, a mono-exponential decay curve is fitted to the recorded ring-down transient. In this way CRDS can also be used for recording absorption signals. An absorption spectrum is obtained by taking the ratio of ring-down times with and without the sample and plotting it for each wavelength. The spectra are recorded at a high resolution which allows for the determination of accurate molecular parameters. Since the decay rate, rather than the absolute intensity, is measured, CRDS is insensitive to power fluctuations for each input light pulse. This is crucial since it is preferred to have experimental conditions as constant as possible for the whole measurement run where it typically takes a much longer time to obtain a wavelength scan compared to, e.g., IBBCEAS. However, since CRDS requires higher mirror reflectivities (typically, in the experiments performed in this thesis, $R \gtrsim 99.995\%$), this consequently limits the range of wavelengths that can be covered for a given measurement. Similarly, the lasing frequency of the dye is another limiting factor to consider when using a dye laser as a light source. Due to this inherent slowness especially when larger wavelength domains have to be covered, combining CRDS with IBBCEAS makes for a viable experimental approach in tackling spectral identification of astronomical observations such as the carriers of the DIBs.

In the LaserLaB at the Vrije Universiteit Amsterdam, a standard pulsed-CRDS setup (Ityaksov 2009, Zhao et al. 2011a, Haddad 2014, Bacalla et al. 2015) is used for recording spectra of transient species in the gas phase produced in a plasma discharge

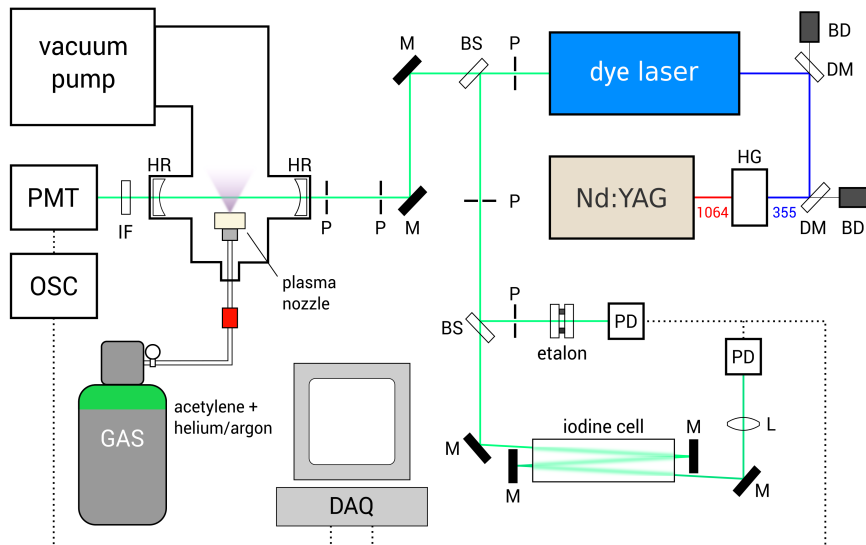


Figure 2.5: Block diagram of the CRDS setup in the LaserLaB in Amsterdam. Harmonic generation crystal (HG); dichroic mirror (DM); beam dump (BD); pinhole (P); beamsplitter (BS); lens (L); photodiode (PD); mirror (M); high-reflectivity mirror (HR); interference filter (IF); photomultiplier tube (PMT); oscilloscope (OSC); data acquisition interface (DAQ). *Figure adapted from Bacalla (2014).*

(Figs. 2.5 and 2.6). The light source is a tunable dye laser (Sirah, Cobra-Stretch) pumped by a Nd:YAG laser (Laser Physics, Quanta-Ray). Different dyes can be used, offering specific bandwidths across the IR-Vis-UV range, which can be pumped with either 532- or 355-nm light that is harmonically generated from the 1064-nm light of the Nd:YAG. The laser is typically operated at a 10-Hz repetition rate with a pulse width of around 6 ns at 66 mJ per pulse. Lasing from the dye can be narrowed down to a bandwidth of 0.035 cm^{-1} by using its 2nd order diffraction from two gratings (in a Littrow configuration) which serve as the wavelength selector. The laser beam is split into two: one is directed to the ring-down cavity while the other goes to the calibration section of the setup. A photomultiplier tube (PMT) records the ring-down signal and an interference filter is placed in front of the PMT to filter out the light from the glow produced by the plasma discharge. While taking the ring-down signal, étalon fringes are also recorded together with an absorption spectrum of iodine gas in a cell. The fringes are used for correcting any non-linearity in the wavelength scan brought about by the mechanical tuning of the wavelength selector; the I_2 spectrum

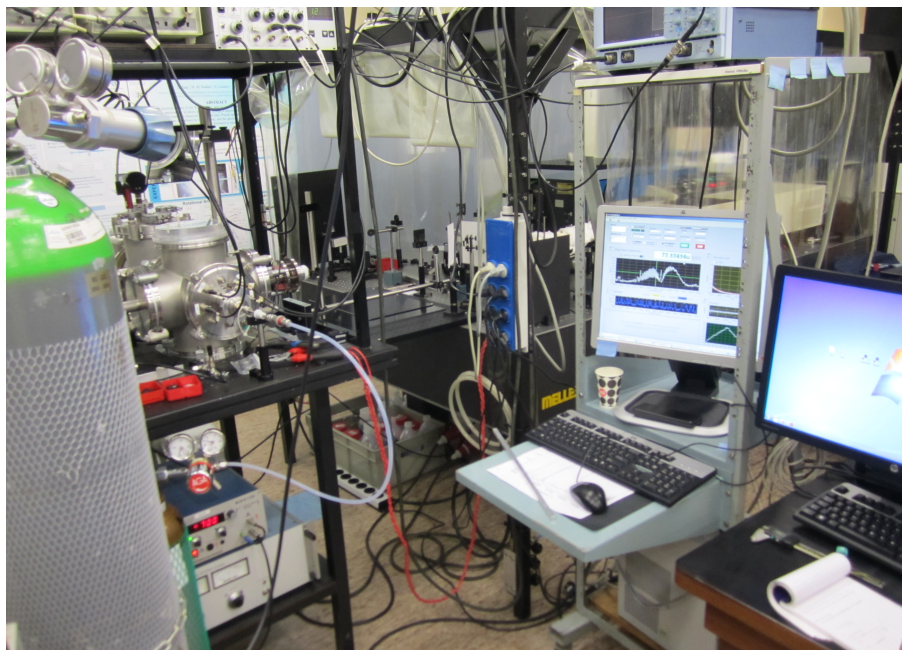


Figure 2.6: The pulsed-CRDS setup in the LaserLaB at the VU University Amsterdam.

($\sim 11\,600\text{--}20\,000\text{ cm}^{-1}$ or $\sim 500\text{--}860\text{ nm}$) is for absolute wavelength calibration, with an accuracy of $\pm 0.02\text{ cm}^{-1}$ (Martin et al. 1986, Knöckel et al. 2004). The ring-down signal from the oscilloscope, as well as the étalon transmission and I_2 absorption signals from the photodetectors, are interfaced into a computer where data are recorded and analyzed. Using a routine developed in LabVIEW, an exponential decay curve is fitted to the ring-down signal and a data point is recorded for every average of 10 ring-down events. In this setting, a measurement covering $\sim 10\text{ cm}^{-1}$ (0.3 nm) will run for about an hour. Wavelength calibration is performed in the PGOPHER software (Western 2014), as well as the absorption line / band fitting to extract molecular constants from the recorded spectrum.

2.3 Plasma production

In this work, the spectra of carbon-based molecules in the gas phase are studied. The molecular transients are formed in supersonically expanding plasma jets. The basic idea is to start with a dilute mixture of a precursor gas and an inert buffer gas: $< 1\%$ acetylene (C_2H_2) in helium or argon. The gas mixture is injected into the vacuum chamber (baseline pressure in the order of 10^{-3} mbar) through a solenoid valve (General Valve, Series 9) with a 2-mm orifice and is typically operated at a pulse du-

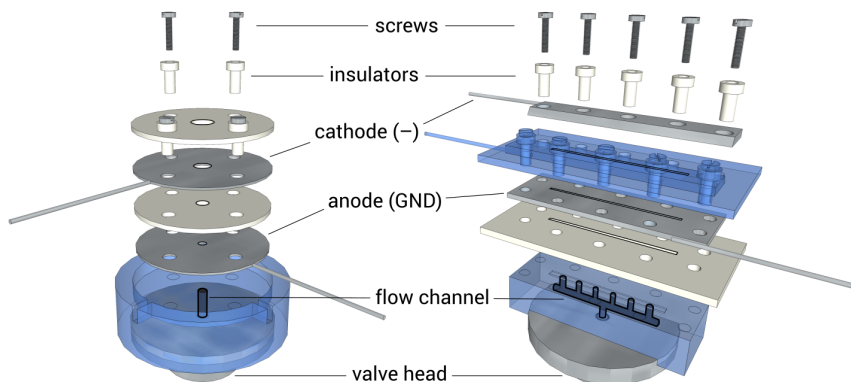


Figure 2.7: Exploded view drawing of the pinhole- and slit plasma nozzle. In essence, both designs incorporate metal- and ceramic plates arranged alternately—the main difference being the profile of the generated plasma jet (conical and planar, respectively). Some components in the figure are set as transparent (blue) for visual aid.

ration of around 1 ms. Behind the solenoid a gas flow fixture with a pinhole or slit is mounted. A rotary vane – roots blower pump system ($\sim 1000 \text{ m}^3/\text{h}$ pumping capacity) is used for maintaining the vacuum pressure at around 0.1 mbar as the gas expands supersonically into the chamber. Aside from reduced gas use, in contrast to a continuous gas flow, operating in pulsed-mode helps in attaining higher input/backing pressures (up to 10 bar) which enhances the rotational/vibrational cooling of the molecules due to the adiabatic expansion of the gas into the vacuum chamber. This is important since the rovibrational temperature will affect the profile of the spectrum and thus, the low-temperature spectra makes it easier to directly compare the recorded features in the laboratory with astronomical spectra. Moreover, as a limited number of molecules is forced into a smaller number of states, the overall detection sensitivity increases.

To generate the plasma, a stream of electrons is needed to break apart the precursor molecules into smaller units which can then recombine to form larger species such as carbon chains. The manner as to how this final step is done sets the different nozzle configurations apart from each other, and this will be described in detail below.

2.3.1 Pinhole- and slit nozzle

The pinhole- and slit nozzle both consist of metal plates that are separated by a ceramic insulator, with the whole assembly fastened onto a certain type of gas flow channel piece that sits atop the solenoid valve head (Fig. 2.7). The plate situated most downstream is raised to a high negative voltage (cathode) with respect to a grounded

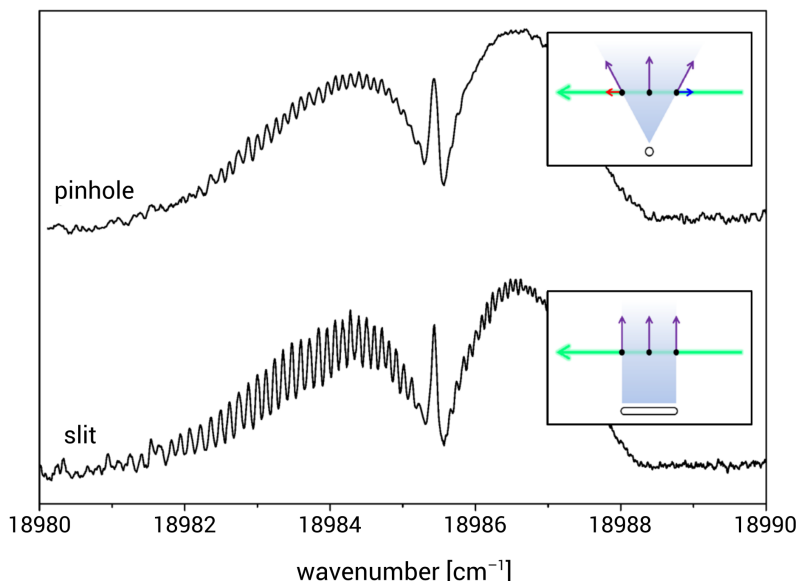


Figure 2.8: Comparison of the plasma jet profiles produced (inset) and the resulting spectra using a pinhole and a slit nozzle. Since velocity components (red and blue arrows) along the optical axis of the cavity (green arrow) are minimized in a planar plasma expansion, the resulting absorption line widths in the spectrum recorded are narrower / more resolved, that is, Doppler broadening is reduced. The spectrum shown here is a spin-orbit component ($\Omega = 3/2$) of the $B^2\Pi_{\Omega} - X^2\Pi_{\Omega}$ electronic origin band of C_6H , measured with CRDS. *Figure taken from Bacalla (2014).*

plate, creating a potential difference that allows for electrons to jump from one plate to the other as the gas pulse comes in between. Voltages from -600 to -1000 V are typically used, and currents of up to 120 mA are needed to keep the plasma stable. The plates are arranged such that the electrons will flow counter to the gas flow (i.e., upstream) so as to increase the efficiency in dissociating the molecules. In fact, this is the only configuration that allows a stable flow as otherwise the much slower cations are forced upstream. Similarly, this electron discharge is pulsed and is synchronized together with the injection of the gas into the vacuum chamber—the discharge ideally going off at the most concentrated and stable part of the gas pulse. The plasma interaction region in the space between the plates is where most of the recombination of dissociated fragments occurs; high backing pressures also increase the instances of collisions in this confined space.

The main difference between the pinhole- and the slit nozzle design, as their names suggest, is the form of the nozzle orifice which consequently affects the result-

ing geometry of the plasma jet. The pinhole design, comprised of alternating metal- and ceramic plates with holes of increasing diameter (1.0–3.5 mm), produces a conical plasma expansion profile with a particle density that decreases quadratically with distance from the nozzle along the gas flow direction (downstream). On the other hand, the slit design is formed by an array of pinholes that distribute the gas output along a line, providing for a longer sample length. Particularly in combination with CRDS or IBBCEAS, this increases the effective absorption pathlength. Combined with plates of narrow slit orifices (3 cm \times 200–800 μ m), this nozzle also effectively generates a planar plasma expansion which significantly reduces the first-order Doppler broadening of the absorption lines (Fig. 2.8). Downstream, the particle density of the planar plasma decreases inversely with distance from the nozzle. In addition, instead of having a single cathode, the slit nozzle has two metal jaws with which the separation distance can be adjusted. This can narrow down the jet expansion angle perpendicular to the slit orientation and will further increase the collision-induced cooling of rovibrational states of the molecules. Finally, the pinhole nozzle consumes much less gas than the slit which makes it a better choice when recording the spectra of plasma synthesized using [expensive] isotope precursors.

2.3.2 Electron impact ionization source

Besides plasma driven by a high-voltage (HV) discharge, electron impact ionization (eI^2) can also be used. Such sources are known to produce ions and other species more effectively compared to HV discharges, as the plasma is generated in a less-destructive manner. The eI^2 source employs electron bombardment of a gas pulse to induce the fragmentation and ionization of molecules (Fig. 2.9). From the pulsed valve, the gas flows through an expansion slit (3.2 cm \times 50 μ m) and into the vacuum chamber. A 0.2-mm diameter tungsten filament is extended along the central axis of a molybdenum tube that is slotted (through hole/slit) to expose the wire along its length. A current of 4 A through the tungsten wire heats it up and starts off the thermionic emission of electrons. Acting as a Wehnelt shield, the negatively-biased molybdenum tube confines the electron cloud along the through slit and a voltage of 80–120 V is applied to accelerate the electrons towards a grounded anode which also has an aperture to let the electron beam through. This continuous stream of electrons is placed as close as possible to the gas expansion slit and is oriented to bombard the gas pulse from below which then creates the plasma. The electron gun assembly sits on a water-cooled block to keep its temperature at an operating level. It should be noted that slit eI^2 sources have been used in the past, albeit in continuous mode (Verbraak et al. 2007). The current system described here is the first system that operates in pulsed mode, resulting in a lower gas flow that can be extended to utilize carbon-bearing precursors.

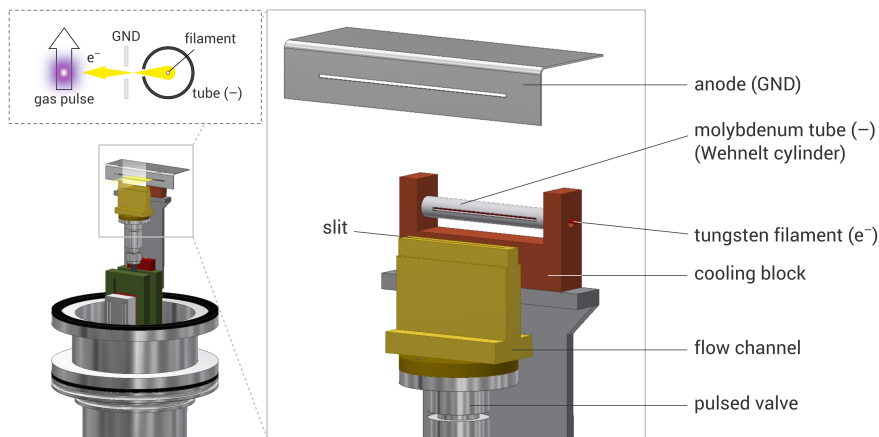


Figure 2.9: The electron impact ionization (eI^2) source as mounted on the vacuum flange. Inset cartoon: the focused electron beam hits the planar gas pulse from one side and induces plasma production. *Technical drawing by Martijn Witlox.*

2.4 Results

Presented in this section are absorption spectra as well as wide surveys of emission spectra of the hydrocarbon plasma produced using the slit discharge nozzle and the electron impact ionization source. The spectra are recorded in the visible region using IBBCEAS.

2.4.1 Optical absorption spectra of a hydrocarbon plasma

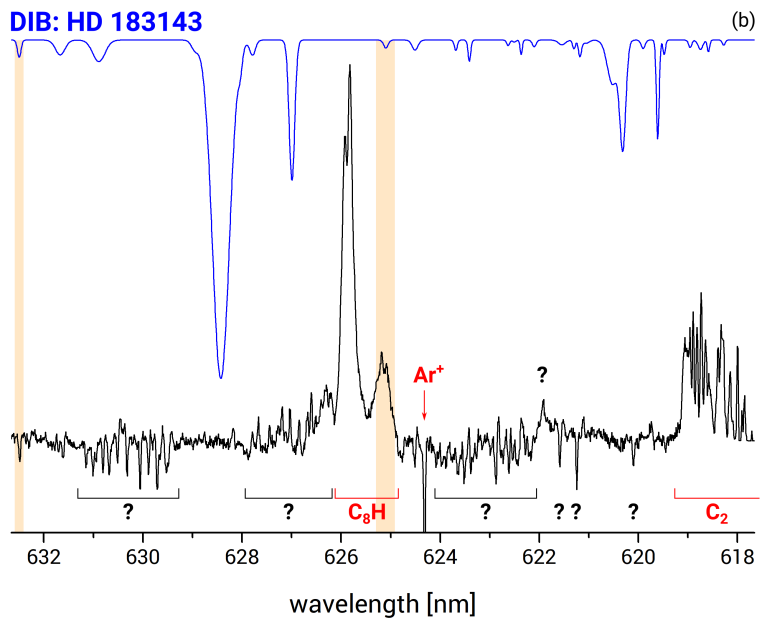
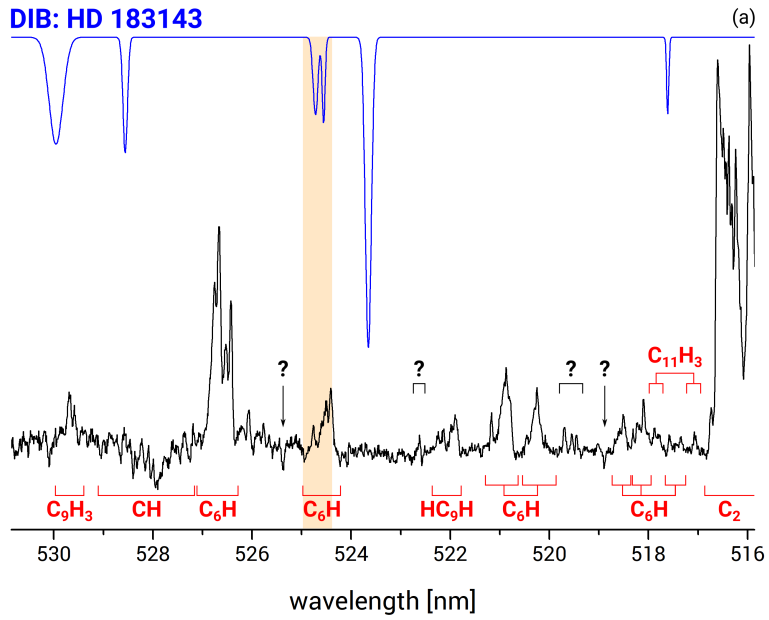
Starting from a dilute mixture of acetylene (0.3%) and argon, a hydrocarbon plasma is generated using the slit discharge nozzle and spectra are recorded through IBBCEAS. These are presented in the figures to follow and will be compared to the diffuse interstellar bands. (The simulated DIBs spectrum is based on observations done by [Hobbs et al. \(2009\)](#) along the sightline towards HD 183143, and each DIB is represented by a Gaussian.) In this comparison exercise, there are criteria to be fulfilled in order for a possible match to be confirmed.

First and most obvious is that the central wavelength of the absorption feature must coincide with the DIB center. Since this is an absorption measurement in the gas phase, it has the advantage of having the recorded spectra directly comparable to astronomical observations (after shifting them to the laboratory frame) in contrast to, for example, matrix isolation spectroscopy which suffers from wavelength shifts

caused by solid state interactions. It is important to ensure that laboratory data (especially in laser experiments which are measured in cm^{-1} in vacuum) are correctly compared to astronomical spectra (\AA in air, which additionally requires an index of refraction scaling in view of observations done at high altitudes). Looking at Fig. 2.10a, a slight coincidence is seen between two DIBs and one of the absorption features of C_6H at around 524.7 nm. Since this band is one of the many vibronic bands of C_6H (see Chap. 4 of this thesis), it is additionally required to have a DIB aligning with the strongest band of C_6H at around 526.6 nm which is the origin band. Clearly, C_6H fails this criterion and thus, is not a DIB carrier. For this same reasoning C_8H (see Fig. 2.10b) is excluded as a DIB carrier. In the figure, there is one line coincident with a DIB absorption at a little beyond 632 nm; this is, however, excluded since it is in emission. In Fig. 2.10c a coincidence can also be observed between C_{10}H and a broader DIB overlapped with narrower features. The other requirement is also fulfilled since the coincident absorption feature is the origin band of C_{10}H . However, this does not immediately indicate a match. Naturally, all of the subsequent vibronic bands of C_{10}H that will be associated with a DIB must follow the band intensity ratios according to the assumed vibronic temperature.

If the DIB has fine structure, then the next thing to check is the band profile of the absorption feature. The shape of the band is mainly dictated by the rotational temperature of the molecules; being able to manipulate this in the laboratory is a plus. In our experimental setup, it has been shown before (see, e.g., Zhao et al. 2011a) that this is possible by adjusting the distance of the pinhole discharge nozzle from the cavity axis. Moreover, the supersonic expansion of the plasma helps produce vibrationally- and/or rotationally cool molecules which are more representative of the conditions in the astronomical environments where DIBs are observed. One can also perform CRDS measurements to fully resolve (if applicable) the rotational lines of the absorption band that will enable for the spectroscopic constants to be measured. Alternatively, band contour fitting algorithms can also be employed. These constants can then be used for simulating rotational temperatures to change the band shape accordingly.

It is natural that more questions will arise as a molecule progresses from being a potential candidate to a DIB carrier. One might then ask about the chemistry involved in the formation of the molecule. For instance, having seen (even hypothetically) an absorption feature of C_{10}H in the DIBs spectrum, is it then more likely to form this larger molecule in space compared to C_8H or C_6H ? If this is true, then we are taking the *top-down* route of molecule formation which is contrary to the way how we synthesize these molecules in the laboratory (i.e., starting from C_2H_2). This then poses the question whether these larger molecules can be photostable in the environments where we observe them which can also constrain certain geometries that they can have. Will cosmic rays also play a role in any of the reactions in the network leading to the formation of the molecule? If we follow the other route, *bottom-up*, then it is not possible to form C_{10}H without having the smaller molecules in the mix, as what we see in our laboratory spectrum. This implies that the coincident DIB is yet caused



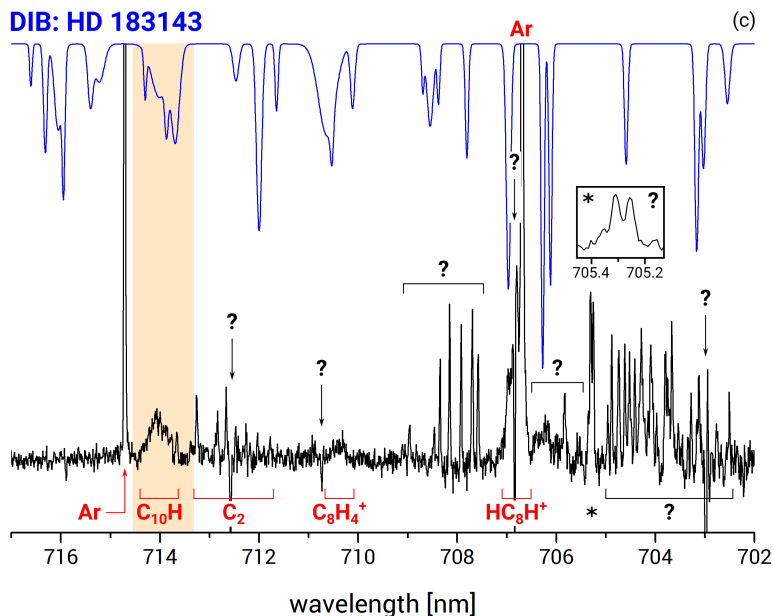


Figure 2.10: Overview spectrum of a hydrocarbon plasma measured using IBBCEAS (black trace; flipped vertically) compared to a simulated DIBs spectrum towards HD 183143 (blue trace; Hobbs et al. 2009). (a) One of the vibronic bands of C_6H (highlighted) seems to coincide – which is not necessarily a match – with a DIB feature around 524.7 nm. (b) The Ar^+ emission line at around 624.3 nm can be used for shifting the whole spectrum to rest wavelength. (c) One of the Ar absorption lines at around 706.7 or 714.7 nm can be used for shifting the whole spectrum to rest wavelength.

by another molecule with an origin- or vibronic band which happens to overlap with the origin band of $C_{10}H$. In fact, the chances are quite high, as some 500 DIBs cover the wavelength range from roughly 400–1000 nm. The process of testing continues.

There still are a few things that can be said about the laboratory spectrum. All of the spectral features, both identified⁶ and unidentified, are produced simultaneously in the plasma discharge. Experimental settings, such as the discharge voltage and the backing pressure, also determine the chemical species produced in the plasma. In principle, the concentration as well as the kind of precursor gas can also be changed. These can all affect the relative amount of the species produced, so one can tune the measurement to a particular molecule. Using the different plasma sources can also

⁶ All molecules indicated in the plots were identified using available wavelength positions provided for in the literature (see e.g., Motylewski et al. 2000 and references therein).

result to having diverse products, as we shall see in the emission spectra presented in the next section.

2.4.2 Optical emission spectra of a hydrocarbon plasma

By replacing the cavity mirrors of BB-DIB with MgF_2 windows, an emission spectroscopy experiment can easily be set up. Shown in Fig. 2.11 is a wide spectral survey (320–860 nm) of emission features of a hydrocarbon plasma produced with a slit discharge nozzle. Typically, a quick scan over this wavelength range takes less than 10 mins. At first glance, a number of bands can already be observed, usually in the form of vibronic progressions. These have been identified as the Swan bands of C_2 (red) and the $A^2\Delta - X^2\Pi$ transition of CH (purple). Unidentifiable features are indicated in gray.⁷ Since the spacing between the rotational lines decreases as the length and/or the mass of a molecule increases, then we should expect that most of the bands that are more pronounced are due to the smaller species. Another emission feature, the electronic origin band of C_3 at ~ 405 nm is also observed (in green). The difference in the width of the band is markedly different, which means that the bands produced by larger/longer molecules would only get narrower, and thus, would require a much zoomed-in recording of spectra (such as in Fig. 2.10). We can also see individual lines that are sparsely distributed over the entire range which are likely due to atomic transitions such as that of argon and, by the fact that C_2 is produced from the dissociation of C_2H_2 , hydrogen. But a significantly denser distribution of these lines can be found in the emission spectra produced by the electron impact ionization source (Fig. 2.12). Here we see the same C_2 and CH transitions as that in the slit discharge, albeit weaker (both the slit discharge and the eI^2 emission spectra are plotted with the same intensity scale).

The emission features recorded here are of less importance to DIBs research, but these may turn out useful when comparing with, for example, the extended red emission (van Winckel et al. 2002, Zagury 2009). In the figures, a relatively low-resolution spectra from the Red Rectangle nebula is superposed (blue trace; data extracted from Zagury 2009) with the hydrocarbon emission features. In a first-order inspection, none of the most prominent bands produced by the smaller species (from both plasma sources) coincide with the astronomical spectra, although at higher resolution, the $d^3\Pi_g \rightarrow a^3\Pi_u$ Swan band of C_2 has been detected (Wehres et al. 2010).

⁷ It is quite possible that the unknown bands found at longer wavelengths are merely higher order diffractions of the emission features seen at much shorter wavelengths because the current configuration of the spectrograph allows for this to happen. On the CCD detector, the blue part of the higher order dispersion overlaps with the red part of the current grating order set by the spectrometer. For instance, the CH band around 430 nm shows up again at 860 nm, which is twice its wavelength. This technical issue, however, can be mitigated by using appropriate color/interference filters.

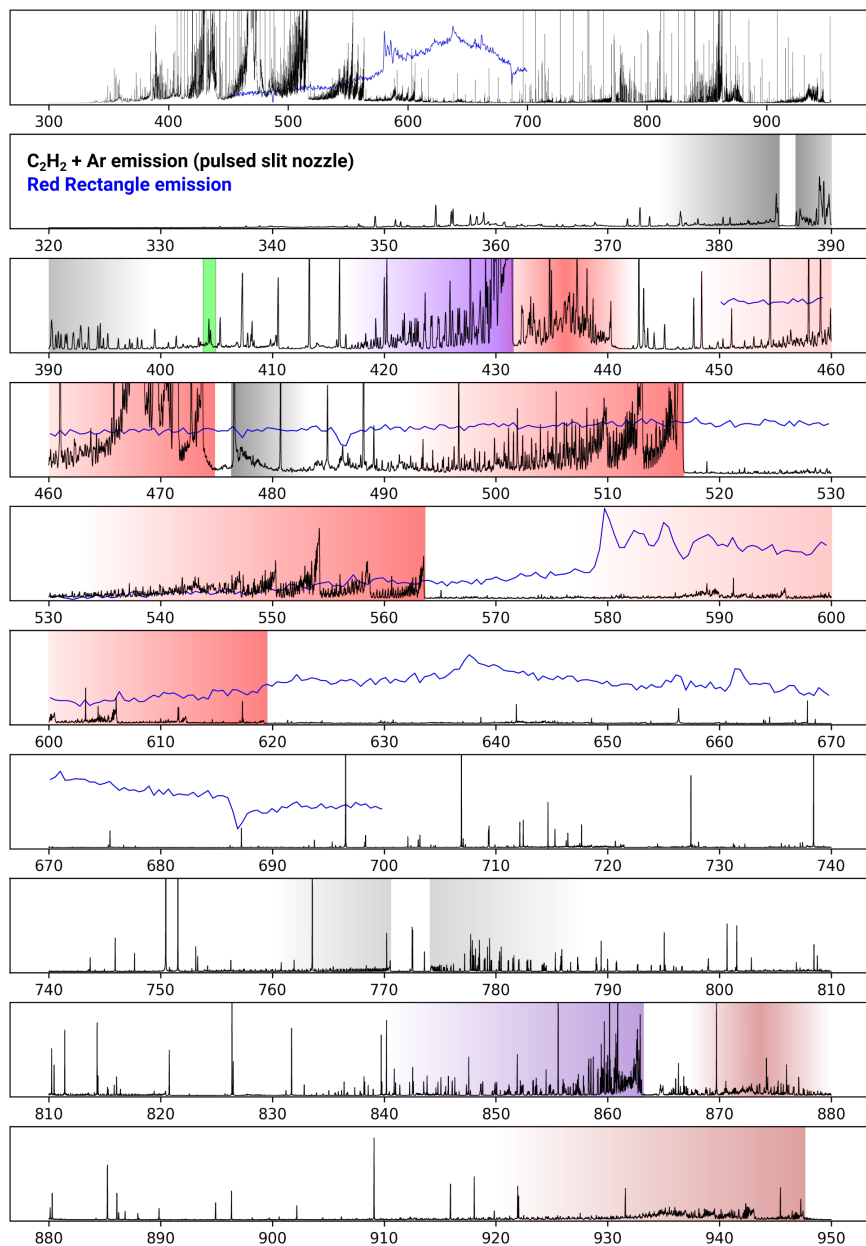


Figure 2.11: IBBCEAS wide spectral survey (320–860 nm) of emission features from the slit discharge nozzle compared with the Red Rectangle emission (Zagury 2009). See main text for a complete description.

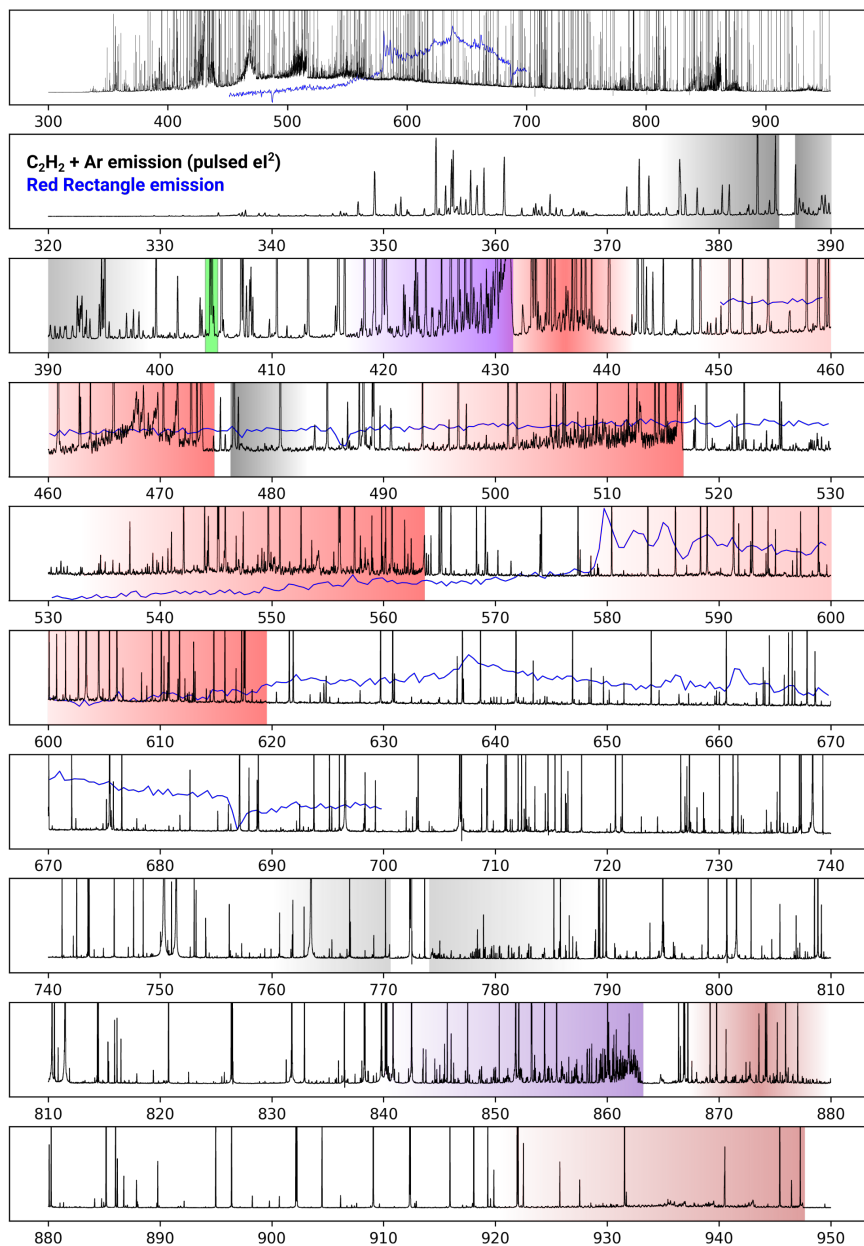


Figure 2.12: IBBCEAS wide spectral survey (320–850 nm) of emission features from the electron impact ionization source compared with the Red Rectangle emission (Zagury 2009). See main text for a complete description.

So far, we have not recorded any absorption feature of a hydrocarbon chain (e.g., C_6H , C_8H , $C_{10}H$), or of any larger molecule for that matter, using the eI^2 source in BB-DIB; these molecules can be observed with the slit discharge nozzle, as was presented in the previous section. The eI^2 source was previously operated as a continuous flow gas nozzle (Verbraak et al. 2007), and thus it was made pulsed in order to increase the density of the plasma created. This is with the assumption that the majority of the precursor molecules gets dissociated and/or ionized and can recombine through collisions. The recombination is effectively enhanced in the slit nozzle by having a small plasma interaction region in between the plates. On the other hand, since the eI^2 source produces the plasma when the gas has already started expanding into the vacuum chamber, there might well be fewer collisions taking place. Because the exact mechanism of plasma production using these sources can be challenging to pin down, one can also try out different plasma settings or even different precursor gases and check each time whether new absorption (or emission) features show up in the spectrum.

2.5 Summary

In this chapter we have presented ways as to which we can record optical absorption and emission spectra in the laboratory and have compared these measurements directly with [simulated] astronomical observations of the diffuse interstellar bands and the Red Rectangle emission. So far, no match has been confirmed. A combination of the IBCEAS technique with high resolution spectroscopy such as CRDS holds the potential for efficiently pinning down the carriers of the DIBs. The speed of data acquisition in IBCEAS proves to be quite useful in making spectral surveys for new bands most especially because of the almost trial-and-error nature of this experimental approach. Employing a mass-spectroscopic technique will also help in confirming the species synthesized. In addition, using hydrocarbon precursors other than acetylene in combination with the newly-developed pulsed electron impact ionization source as well as the slit plasma nozzle will be a way forward in searching for new spectral features in the laboratory.

CHAPTER 3

The $B^2\Pi-X^2\Pi$ electronic origin band of $^{13}\text{C}_6\text{H}$

The rotationally resolved spectrum of the $B^2\Pi-X^2\Pi$ electronic origin band transition of $^{13}\text{C}_6\text{H}$ is presented. The spectrum is recorded using cavity ring-down spectroscopy in combination with supersonic plasma jets by discharging a $^{13}\text{C}_2\text{H}_2/\text{He}/\text{Ar}$ gas mixture. A detailed analysis of more than a hundred fully-resolved transitions allows for an accurate determination of the spectroscopic parameters for both the ground and electronically excited state of $^{13}\text{C}_6\text{H}$.



This chapter is based on the work of Bacalla, X., Zhao, D., Salumbides, E. J., Haddad, M. A., Linnartz, H., and Ubachs, W. “The $B^2\Pi-X^2\Pi$ electronic origin band of $^{13}\text{C}_6\text{H}$ ” in *J. Mol. Spectrosc.* **308–309** (2015) 41–44.

3.1 Introduction

The hexatriynyl radical C_6H , a member of the linear C_{2n}H series, belongs to the spectroscopically best studied carbon chain radicals. The $X^2\Pi$ ground state was studied extensively in Fourier-transform microwave (MW) studies, yielding accurate constants (Pearson et al. 1988, Linnartz et al. 1999, Gottlieb et al. 2010). The laboratory data followed astronomical detections of this molecule in the cold dense cloud TMC-1 (Suzuki et al. 1986, Cernicharo et al. 1987). Later this molecule was detected along other lines-of-sight as well, e.g. towards the carbon rich star IRC+10216 (Cernicharo et al. 2000). The $B^2\Pi-X^2\Pi$ electronic spectrum of C_6H was reported in several studies. The first data were recorded in Ne matrix isolation studies after mass selective deposition (see e.g. Freivogel et al. 1995). This provided approximate values for the gas phase absorptions. The first gas phase spectrum was obtained under somewhat poor experimental conditions, using a hollow cathode discharge cell (Kotterer & Maier 1997). The resulting spectrum only showed unresolved features, including many bands starting from vibrationally excited states. Subsequently, high precision and rotationally resolved spectra were recorded using a new planar plasma source design (Motylewski & Linnartz 1999) that allowed the detection of rotationally cold C_6H and C_6D transients under nearly Doppler-free conditions (Linnartz et al. 1999). Combined with sensitive detection techniques, such as cavity ring-down spectroscopy, it was possible to realize excellent S/N ratios, not only for the origin band but also for transitions involving vibrationally excited levels in the upper electronic state. In combination with the available MW constants it was possible to derive precise upper state constants, for both spin-orbit components. Recently, a substantially extended study of these electronic bands, as well as new transitions involving vibronic hot bands, was presented, with a focus on Renner-Teller effects in C_6H (Zhao et al. 2011a). In the present work we extend previous spectroscopic studies to the fully ^{13}C -substituted isotopologue $^{13}\text{C}_6\text{H}$. The rotationally resolved electronic spectrum yields accurate spectroscopic constants, also including the ground state constants that have not been determined before.

3.2 Experiment / method

We follow an established method that has been used successfully to record electronic spectra of many different carbon chain radicals before. Details of the experimental setup and experimental procedures are available from Motylewski & Linnartz (1999) and Zhao et al. (2011a,c). Supersonically jet-cooled $^{13}\text{C}_6\text{H}$ radicals are produced – among other species – in a pulsed (~ 10 Hz) planar or pinhole plasma expansion generated by discharging a high pressure (10 bar) gas pulse comprising of 0.18% ^{13}C -enriched (99% purity) C_2H_2 in a helium:argon $\sim 85:15$ mixture. Both slit and pinhole discharge nozzles, which have been used to study $^{12}\text{C}_6\text{H}$ (Zhao et al. 2011a), are employed in the present experiment. The 3 cm \times 300 μm slit discharge nozzle, with typical discharge I/V values of ~ 100 mA/–750 V per jaw, is used to generate

a planar plasma expansion with a nearly Doppler-free environment and a relatively long effective absorption path length. The pinhole nozzle system, with typical $I/V \sim 80 \text{ mA}/-1000 \text{ V}$ values, generates a plasma expansion suffering from a somewhat larger Doppler width, but allows measuring spectra with different rotational temperatures in a more convenient way. Final rotational temperatures typically amount to 15–30 K.

The $^{13}\text{C}_6\text{H}$ spectra are recorded in direct absorption using cavity ring-down laser spectroscopy. Tunable light around 525 nm – the region where regular C_6H has been found – is generated using a Nd:YAG pumped pulsed dye laser ($\sim 6 \text{ ns}$ pulse duration). The bandwidth of the dye laser is $\sim 0.035 \text{ cm}^{-1}$, well below the expected line splitting between two adjacent rotational transitions. The light pulse is spatially filtered and enters a 58 cm long optical cavity comprising of two high reflection mirrors. The optical axis is aligned a few mm downstream, parallel to the slit or below the pinhole of the nozzle. Light leaking out of the cavity is recorded by a photo-multiplier tube and a spectrum is obtained by recording the ring-down time as function of the laser wavelength. Typical ring-down times amount to 40–100 μs . A precise pulse generator coordinates that the gas and the discharge pulse, and as well as the ring-down event, coincide. Simultaneously with the spectral recordings of $^{13}\text{C}_6\text{H}$, transmission fringes of an etalon (with a free spectral range of $\sim 20.1 \text{ GHz}$) are recorded, providing relative frequency markers to correct for a possible non-linear wavelength scanning of the dye laser. An iodine spectrum allows for an absolute wavelength calibration with an accuracy better than 0.02 cm^{-1} .

3.3 Results and analysis

In Fig. 3.1 the $\text{B}^2\Pi-\text{X}^2\Pi$ electronic origin band (0_0^0) transition of regular C_6H (upper panel) and of $^{13}\text{C}_6\text{H}$ (lower panel) is shown. The newly recorded $^{12}\text{C}_6\text{H}$ spectrum compares well with data presented by Linnartz et al. (1999) and Zhao et al. (2011a). From a comparison of both panels it can be concluded that the ^{13}C -sample is highly pure, as nearly no features due to ^{12}C contamination can be clearly seen. Some extra lines in the lower panel – recorded through the slit expansion – are due to overlapping hot band transitions of other small hydrocarbons in the plasma. Previous work has shown that these lines become much weaker using the pinhole discharge nozzle, as visible from the corresponding spectrum. It should be noted that in contrast to the pinhole nozzle experiments by Zhao et al. (2011a), the final Doppler width of individual transitions is smaller, mainly because of the reduced expansion velocity of the jet that is run with more argon in the gas mixture.

The overall spectral pattern of $^{13}\text{C}_6\text{H}$ is very similar to that of $^{12}\text{C}_6\text{H}$, with a blue shift of $\sim 2 \text{ cm}^{-1}$. Both spectra consist of two components, each with (fully resolved) P , Q and (partially resolved) R branches, reflecting transitions between the two spin-orbit components: $\text{B}^2\Pi_{3/2}-\text{X}^2\Pi_{3/2}$ and $\text{B}^2\Pi_{1/2}-\text{X}^2\Pi_{1/2}$. The two band systems are split by $\Delta A = |A' - A''|$: the difference between the spin-orbit splitting in the ground

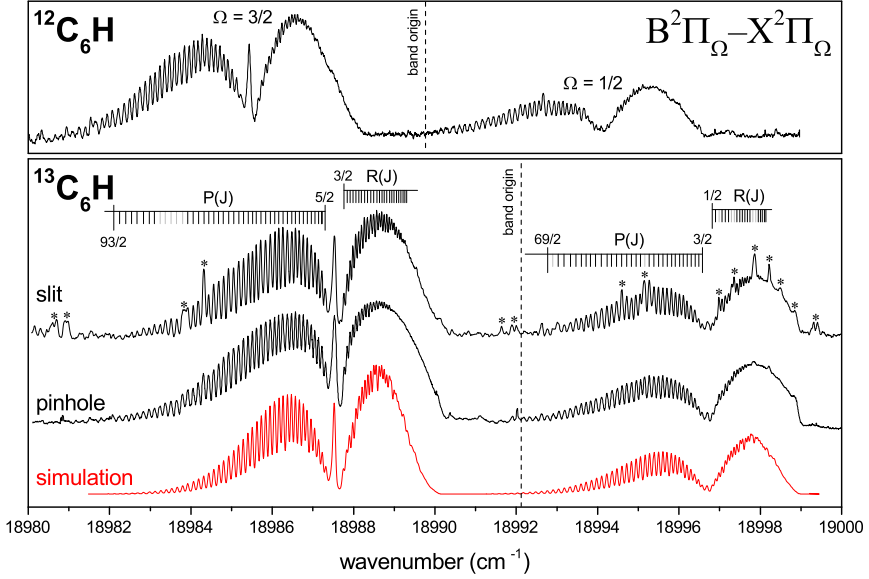


Figure 3.1: The $B^2\Pi-X^2\Pi$ electronic transition of $^{12}\text{C}_6\text{H}$ (upper panel) and $^{13}\text{C}_6\text{H}$ (lower panel) for a planar (slit) and a pinhole plasma expansion. Features indicated by an asterisk are due to other species and are mainly visible in the slit nozzle plasma. A simulated spectrum for $^{13}\text{C}_6\text{H}$ is shown in the lowest trace, based on the constants listed in Table 2 and a rotational temperature of $T_{\text{rot}} = 20.3(1)$ K.

and excited state. An assignment of the individual spin-orbit components is straightforward; with a low final temperature in the jet expansion, the more intense component corresponds to a transition from the lower spin-orbit state, i.e. $X^2\Pi_{3/2}$ for C_6H . The observation of the barely visible Q -branch in the $B^2\Pi_{1/2}-X^2\Pi_{1/2}$ system provides further evidence for this assignment, as the intensity of the Q -branch scales quadratically with the value of the spin-orbit angular momenta (Ω^2).

The detailed rotational assignments for $^{13}\text{C}_6\text{H}$ are shown in Fig. 3.1. The determined transition energies of the 116 assigned lines listed in Table 3.1 are used to fit five parameters. For regular C_6H a full analysis has been presented before (Linnartz et al. 1999, Zhao et al. 2011a), guided by accurate ground state constants available from MW work (Pearson et al. 1988, Linnartz et al. 1999). The focus here is on $^{13}\text{C}_6\text{H}$ for which ground state constants are not available; it is important, therefore, to realize that ground and excited state parameters may correlate in a fit.

The rotational analysis is performed using the PGOPHER software (Western 2014). The transition frequencies are fitted using a standard Hamiltonian for a $^2\Pi-^2\Pi$ electronic transition, with the band origin T_0 , rotational parameters B'' and B' , and spin-

Table 3.1: The observed line positions (in cm^{-1}) for the two spin orbit components of the $\text{B}^2\Pi\text{--X}^2\Pi$ electronic transition of $^{13}\text{C}_6\text{H}$.

<i>P</i> -branch		$\text{B}^2\Pi_{3/2}\text{--X}^2\Pi_{3/2}$		$\text{B}^2\Pi_{1/2}\text{--X}^2\Pi_{1/2}$		<i>R</i> -branch		$\text{B}^2\Pi_{3/2}\text{--X}^2\Pi_{3/2}$		$\text{B}^2\Pi_{1/2}\text{--X}^2\Pi_{1/2}$	
<i>J'</i>	<i>J''</i>	Observed	o-c	Observed	o-c	<i>J'</i>	<i>J''</i>	Observed	o-c	Observed	o-c
0.5	1.5			18996.57	0.003	1.5	0.5			18996.82	-0.001
1.5	2.5	18987.30	-0.017	18996.48	0.003	2.5	1.5	18987.73	-0.007	18996.90	0.000
2.5	3.5	18987.22	-0.010	18996.39	0.003	3.5	2.5	18987.82	-0.007	18996.99	0.002
3.5	4.5	18987.14	-0.002	18996.29	0.001	4.5	3.5	18987.90	-0.001	18997.06	-0.001
4.5	5.5	18987.05	0.008	18996.20	-0.002	5.5	4.5	18987.98	0.003	18997.14	0.000
5.5	6.5	18986.96	0.006	18996.11	0.002	6.5	5.5	18988.06	0.004	18997.22	0.007
6.5	7.5	18986.86	-0.002	18996.02	0.008	7.5	6.5	18988.13	-0.001	18997.29	0.001
7.5	8.5	18986.76	-0.006	18995.92	0.007	8.5	7.5	18988.20	-0.005	18997.36	-0.003
8.5	9.5	18986.66	-0.004	18995.81	0.006	9.5	8.5	18988.27	-0.014	18997.43	-0.004
9.5	10.5	18986.57	0.002	18995.70	-0.010	10.5	9.5	18988.34	-0.013	18997.50	0.000
10.5	11.5	18986.48	0.012	18995.60	-0.003	11.5	10.5	18988.42	-0.003	18997.56	-0.006
11.5	12.5	18986.38	0.009	18995.51	0.009	12.5	11.5	18988.49	0.002	18997.63	-0.009
12.5	13.5	18986.26	-0.004	18995.40	0.004	13.5	12.5	18988.57	0.010	18997.68	-0.014
13.5	14.5	18986.16	0.000	18995.27	-0.012	14.5	13.5	18988.63	0.005	18997.74	-0.019
14.5	15.5	18986.06	0.008			15.5	14.5	18988.69	0.001		
15.5	16.5	18985.95	0.006	18995.05	-0.007	16.5	15.5	18988.75	-0.001		
16.5	17.5	18985.85	0.010	18994.95	0.006	17.5	16.5	18988.82	0.002	18997.95	0.015
17.5	18.5	18985.74	0.008	18994.83	-0.001	18.5	17.5	18988.88	0.002	18998.00	0.010
18.5	19.5	18985.63	0.004	18994.71	-0.005	19.5	18.5	18988.94	0.004	18998.04	-0.004
19.5	20.5	18985.51	0.004	18994.60	0.000	20.5	19.5	18989.00	0.004	18998.10	-0.002
20.5	21.5	18985.40	0.002	18994.49	0.010	21.5	20.5	18989.05	0.005	18998.15	-0.004
21.5	22.5	18985.28	-0.005	18994.37	0.013	22.5	21.5	18989.11	0.009		
22.5	23.5	18985.16	-0.005	18994.24	0.007	23.5	22.5	18989.16	0.005		
23.5	24.5	18985.05	-0.002	18994.10	-0.007	24.5	23.5	18989.21	0.003		
24.5	25.5	18984.93	-0.002	18993.98	-0.002	25.5	24.5	18989.26	0.001		
25.5	26.5	18984.81	0.000	18993.85	-0.004	26.5	25.5	18989.31	-0.004		
26.5	27.5	18984.69	-0.001	18993.73	0.003						
27.5	28.5	18984.56	-0.008	18993.59	-0.003						
28.5	29.5	18984.44	-0.004	18993.46	0.008						
29.5	30.5	18984.31	-0.001	18993.33	0.009						
30.5	31.5	18984.18	-0.006	18993.18	-0.006						
31.5	32.5	18984.05	-0.004	18993.03	-0.016						
32.5	33.5	18983.92	-0.005								
33.5	34.5			18992.77	0.006						
34.5	35.5										
35.5	36.5										
36.5	37.5										
37.5	38.5										
38.5	39.5	18983.10	-0.013								
39.5	40.5	18982.97	0.002								
40.5	41.5	18982.83	0.006								
41.5	42.5	18982.68	-0.005								
42.5	43.5	18982.54	0.002								
43.5	44.5	18982.40	0.008								
44.5	45.5	18982.25	0.001								
45.5	46.5	18982.09	0.000								

Table 3.2: Molecular parameters of $^{13}\text{C}_6\text{H}$ for ground and excited $^2\Pi$ state derived from a line fit (FIT-I) and a combination difference fit (FIT-II), compared with values available from for $^{12}\text{C}_6\text{H}$ (Linnartz et al. 1999, Zhao et al. 2011a). All parameters are in cm^{-1} .

	$^{13}\text{C}_6\text{H}$		$^{12}\text{C}_6\text{H}$
	FIT-I	FIT-II	
B''	0.042973(16)	0.042942(17)	0.04640497
D''^a	1.20×10^{-9}	1.20×10^{-9}	1.35×10^{-9}
A''	-11.62(13)	-12.9(12)	-15.0424
B'	0.042218(17)	0.042199(17)	0.0455952(5)
D'^a	1.20×10^{-9}	1.20×10^{-9}	$1.58(28) \times 10^{-9}$
A'	-20.78(13)	-26(4)	-23.6924(7)
B'/B''^b	0.9824	n/a	0.9825
$ A' - A'' $	9.16	n/a	8.65
T_0^c	18992.116(1)	n/a	18989.7672(4)

^a Parameters fixed in the least-squares fit for $^{13}\text{C}_6\text{H}$.

^b Ratio of rotational constants is dimensionless.

^c Values in parentheses indicate the statistical error from the least-squares fit. The absolute uncertainty in T_0 is limited by the uncertainty in the frequency calibration of the laser, corresponding to 0.02 cm^{-1} .

orbit constants A'' and A' as floating parameters. We note that the centrifugal distortion constants (D'' and D') cannot be well determined with our data set, and therefore, their values are fixed to $1.2 \times 10^{-9} \text{ cm}^{-1}$. This is obtained by scaling the D'' value for $^{12}\text{C}_6\text{H}$ with the reduced mass ratio ($^{12}\text{C}_6\text{H}/^{13}\text{C}_6\text{H}$) which is derived from the rotational constant ratio. It turns out to be possible to fit both spin-orbit components simultaneously with one set of molecular parameters, yielding an overall standard deviation of 0.007 cm^{-1} , i.e., well below the experimental accuracy. The resulting constants are listed under FIT-I in Table 3.2. The corresponding observed-calculated (o-c) values for individual rotational transitions are also listed in Table 3.1. These values exhibit a statistical behavior, indicating that the spectrum is largely free of perturbations.

As no MW data for the ground state exists, it is wise to check for possible correlations between the resulting ground and upper state parameters using a global fit. Indeed, the fitted values for A and B give high correlation coefficients (1.000 and 0.997, respectively). For this, combination differences for both ground and excited state have been fitted separately. The resulting molecular parameters are summarized as FIT-II in Table 3.2. As can be seen, the derived values for (B'' , A'') and (B' , A') are in good agreement with those derived from FIT-I.

A simulated spectrum using these constants is incorporated in the lower panel of Fig. 3.1. The overall pattern reproduces well for a rotational temperature of $T_{\text{rot}} =$

20.3(1) K. This not only applies to the Boltzmann contour, but also to the relative intensity ratio of the two spin-orbit components, indicating that the spin-orbit relaxation is as effective as the rotational cooling.

The fitted band origin of the $B^2\Pi-X^2\Pi$ band of $^{13}\text{C}_6\text{H}$ is roughly 2.35 cm^{-1} blue shifted with respect to the main isotopologue. The rotational constant $B''(^{13}\text{C}_6\text{H})$ is found to be 7.4% smaller than that of $B''(^{12}\text{C}_6\text{H})$, fully consistent with predictions from the previously determined C_6H structure (McCarthy & Thaddeus 2005). Upon electronic excitation, the value of B' decreases, indicating that the molecule stretches, but as the inter-atomic forces are expected to barely change, the B'/B'' ratios for $^{12/13}\text{C}_6\text{H}$ are nearly the same. It should be noted that the effective spin-orbit splitting constants ($|A''|$ and $|A'|$) for $^{13}\text{C}_6\text{H}$ are smaller than those for $^{12}\text{C}_6\text{H}$. This may be due to a different Renner-Teller effect (i.e., the electronic orbital-vibration interaction) in $^{13}\text{C}_6\text{H}$. Indeed, spin-orbit coupling can be significantly affected by Renner-Teller effects; and as discussed by Zhao et al. (2011a), for $^{12}\text{C}_6\text{H}$ a very strong Renner-Teller effect exists.

Acknowledgments

This work has been supported by the Netherlands Organization for Fundamental Research on Matter (FOM) and the Netherlands Organisation for Scientific Research (NWO) through a VICI grant and within the context of the Dutch Astrochemistry Network (DAN). X.B. and W.U. acknowledge support from the Templeton Foundation.

CHAPTER 4

Spectroscopic survey of electronic transitions of the hexatriynyl radical

Electronic spectra of C_6H are measured in the $18\,950 - 21\,100\text{ cm}^{-1}$ domain using cavity ring-down spectroscopy of a supersonically expanding hydrocarbon plasma. In total, 19 (sub)bands of C_6H are presented, all probing the vibrational manifold of the $\text{B}^2\Pi$ electronically excited state. The assignments are guided by electronic spectra available from matrix isolation work, isotopic substitution experiments (yielding also spectra for $^{13}\text{C}_6\text{H}$ and C_6D), predictions from *ab initio* calculations and rotational fitting and vibrational contour simulations using the available ground state parameters as obtained from microwave experiments. Besides the 0_0^0 origin band, three nondegenerate stretching vibrations along the linear backbone of the C_6H molecule are assigned: the ν_6 mode associated with the C–C bond vibration and the ν_4 and ν_3 modes associated with $\text{C}\equiv\text{C}$ triple bonds. For the two lowest ν_{11} and ν_{10} bending modes, a Renner-Teller analysis is performed identifying the $\mu^2\Sigma(\nu_{11})$ and both $\mu^2\Sigma(\nu_{10})$ and $\kappa^2\Sigma(\nu_{10})$ components. In addition, two higher lying bending modes are observed, which are tentatively assigned as $\mu^2\Sigma(\nu_9)$ and $\mu^2\Sigma(\nu_8)$ levels. In the excitation region below the first non-degenerate vibration (ν_6), some $^2\Pi - ^2\Pi$ transitions are observed that are assigned as even combination modes of low-lying bending vibrations. The same holds for a $^2\Pi - ^2\Pi$ transition found above the ν_6 level. From these spectroscopic data and the vibronic analysis a comprehensive energy level diagram for the $\text{B}^2\Pi$ state of C_6H is derived and presented.



This chapter is based on the work of Bacalla, X., Salumbides, E. J., Linnartz, H., Ubachs, W., and Zhao, D. “Spectroscopic Survey of Electronic Transitions of C_6H , $^{13}\text{C}_6\text{H}$, and C_6D ” in *J. Phys. Chem. A* **120** (2016) 6402.

4.1 Introduction

The hexatriynyl radical, C_6H , belongs to the best studied linear carbon chain radicals. As several other members in the acetylenic $C_{2n}H$ series, it has been identified in different environments in the interstellar medium (Suzuki et al. 1986, Cernicharo et al. 1987, Guélin et al. 1987, Kawaguchi et al. 1995). Microwave spectroscopic work (Pearson et al. 1988) has provided accurate spectroscopic constants for the $X^2\Pi$ electronic ground state that later were extended to deuterated hexatriynyl C_6D (Linnartz et al. 1999) as well as to vibrationally excited C_6H (Gottlieb et al. 2010). *Ab initio* calculations (Liu et al. 1992, Brown et al. 1999, Cao & Peyerimhoff 2001), together with infrared (IR) work (Doyle et al. 1991), have also been conducted to predict and identify the fundamental vibrational frequencies of C_6H . Recently, the astronomical detection of the vibrationally excited C_6H (Cernicharo et al. 2008, Gottlieb et al. 2010) and the chemically related C_6H^- anion (McCarthy et al. 2006) triggered a renewed spectroscopic interest in this molecule.

The first electronic spectra of C_6H were recorded using matrix isolation spectroscopy (Forney et al. 1995, Freivogel et al. 1995), results of which guided two gas phase studies (Kotterer & Maier 1997, Linnartz et al. 1999). An unresolved electronic origin band as well as several hot bands were recorded for a rather high temperature ($T_{\text{rot}} \sim 150$ K) using a liquid-nitrogen cooled hollow cathode discharge (Kotterer & Maier 1997). After this, a study of a supersonically expanding and adiabatically cooled plasma resulted in a full rotational analysis of the two spin-orbit components of the $^2\Pi-X^2\Pi$ origin band spectrum for both C_6H and C_6D radicals (Linnartz et al. 1999). An extended study, presenting more accurate data for the electronic origin band as well as a Renner-Teller analysis for the $\{11\}_1^1 \mu^2\Sigma - \mu^2\Sigma$ vibronic hot band, was presented several years later (Zhao et al. 2011a). In the optical spectra only the $^2\Sigma$ vibronic component of the ν_{11} mode was observed, in contrast to the $^2\Delta$ component, which was detected in the microwave spectrum (Gottlieb et al. 2010), but which is most likely too energetic (~ 100 cm^{-1}) to be observed in cold jet expansions. The same holds for the low-lying electronic state with $^2\Sigma$ symmetry, at an excitation energy of $\sim 1\,774$ cm^{-1} , which was observed in a photo-detachment study (Taylor et al. 1998). These states were predicted in *ab initio* electronic structure calculations (Sobolewski & Adamowicz 1995, Cao & Peyerimhoff 2001). Harmonic vibrational frequencies of the various modes in C_6H were *ab initio* calculated, yielding the lowest mode, ν_{11} , at some 100 cm^{-1} and the highest mode at about $3\,300$ cm^{-1} (Brown et al. 1999). Also of interest is the spectroscopic investigation of the C_6H^+ cation, both in a neon matrix (Shnitko et al. 2006) and in the gas phase (Raghunandan et al. 2010).

In the present work, cavity ring-down spectroscopy of a supersonically expanding hydrocarbon plasma has been employed in a wider-ranging spectroscopic survey. All spectroscopic features observed are associated with the $B^2\Pi$ electronically excited state and its vibrational modes. From the C_6H origin band at around $18\,980$ cm^{-1} toward higher wavenumbers, several new spectral features have been observed and found to originate from C_6H as well. Also a substantial number of $^{13}C_6H$ (full ^{13}C

substitution) and C_6D bands has been observed for the first time.

4.2 Experiment

The experimental setup and the measurement procedure are similar to those described before (Motylewski & Linnartz 1999, Zhao et al. 2011a). The carbon chain radicals are formed by discharging different gas mixtures in the throat of a pulsed plasma nozzle, either a slit nozzle (Motylewski & Linnartz 1999) or pinhole design (Zhao et al. 2011c). For C_6H and C_6D , 0.5% $^{12}\text{C}_2\text{H}_2$ in He and 0.3% $^{12}\text{C}_2\text{D}_2$ in He mixtures are used, respectively. An isotopically enriched $^{13}\text{C}_2\text{H}_2$ (99% purity) gas sample, mixed at 0.13–0.18% in He/Ar (85/15) is used to record $^{13}\text{C}_6\text{H}$ fully ^{13}C substituted spectra. A solenoid valve (General Valve, Series 9) on top of the nozzle body controls a high pressure (5–10 bar) gas pulse (roughly of 1 ms duration) that is discharged between ceramically isolated electrodes before expanding into a vacuum, generated by a powerful roots blower system. Typically 300–500 μs long negative high-voltage pulses ($V/I \sim -750 \text{ V} / 100 \text{ mA}$) are offered to dissociate the precursor species and to allow molecule formation through collisions in the expanding plasma. In parallel, the adiabatic expansion allows for final rotational temperatures of the order of 15 to 25 K.

The output of a pulsed Nd:YAG-pumped dye laser is aligned just below (2–5 mm) and parallel to a $3 \text{ cm} \times 300 \mu\text{m}$ slit nozzle, or across the conical jet of a 1.0 mm diameter pinhole. The effective absorption path length along the slit or through the pinhole expansion can be further improved by orders of magnitude by positioning the slit nozzle (or pinhole) along the optical axis set by two highly reflective mirrors ($R > 0.99998$) in a cavity ring-down configuration (Wheeler et al. 1998). Typical values for the ring-down time amount to $\tau = 40$ to $100 \mu\text{s}$, corresponding to effective path lengths of several kilometers through the plasma. The experiment runs at 10 Hz and precise pulse generators are used to guarantee that gas and discharge pulse as well as ring-down event coincide in time. Typically, the average of 10 ring-down events is used for each laser wavelength before being stored as a data point.

The laser bandwidth is about 0.035 cm^{-1} , thus sufficiently narrow to resolve subsequent rovibronic transitions in C_6H that has a rotational constant of the order of 0.045 cm^{-1} ; i.e., two lines are separated by about 0.090 cm^{-1} . The wavelength calibration is achieved, recording simultaneously an etalon transmission spectrum (FSR $\sim 20.1 \text{ GHz}$), which provides relative frequency markers for correction of any nonlinearity during scanning. An iodine (I_2) spectrum is recorded for absolute wavelength calibration, yielding an overall accuracy of better than 0.02 cm^{-1} .

The use of the slit nozzle leads to nearly Doppler-free spectra due to a collimation effect on the gas pulses emanating from the slit jet expansion perpendicular to the laser beam inside the ring-down cavity. In the case of the pinhole nozzle the contribution of molecules with velocity components along the laser beam path is larger, therewith producing spectral lines with extended Doppler broadening. However, the latter effect

can be partially counteracted by mixing Ar in the gas sample, which produces a favorable effect on the spectral linewidth. This advantage is exploited for the recording of $^{13}C_6H$ spectra. The isotopically enriched $^{13}C_2H_2$ was used in combination with the pinhole nozzle which uses up less gas than the slit nozzle. A few of the ^{13}C -containing bands were nevertheless recorded in the slit nozzle configuration.

Obviously, the optical methods used are not mass selective, and spectra contain information from a number of species formed in the plasma, including separate transitions originating from, for example, C_2 , C_3 , or CH. Also, under similar experimental conditions, long linear (Haddad et al. 2015) and bent chain (Zhao et al. 2011b, 2012) carbon-based molecules are formed in the plasma expansion. Although, under the presently used plasma expansion conditions, the larger molecules are rotationally and vibrationally cooled, typically exhibiting rotational temperatures of $T_{\text{rot}} \sim 20$ K and vibrational temperatures of the same values (Zhao et al. 2011a), the diatomic radicals C_2 and CH are detected at elevated temperatures, even allowing the detection of C_2 in the metastable $a^3\Pi$ state in the $v = 9$ level (Haddad et al. 2015). It is noted that the resulting rotational temperature can be regulated by changing the nozzle-to-laser-beam distance (Zhao et al. 2011a,c). Further, the plasma chemistry is different under conditions of a conical expansion when a pinhole nozzle is employed, or for a planar expansion in the case of a slit jet configuration. The spectral features associated with C_2 and CH, which in some cases can be assigned to previously identified transitions, overlap and in some cases congest the C_6H features under investigation in the present study. The isolated line features pertaining to C_2 and CH (and possibly other radicals) will be indicated by an asterisk (*). In particular, in the energy region higher than $19\,350\text{ cm}^{-1}$, with the (0,0) band origin of the $d^3\Pi_g - a^3\Pi_u$ C_2 Swan band at $T_0 = 19\,378.4646(7)\text{ cm}^{-1}$ (Lloyd & Ewart 1999), the spectra become swamped by a line forest, for which reason no spectra for C_6D and $^{13}C_6H$ will be reported in this range. For C_6H the sequence of vibronic states is presented despite the fact that the spectra are severely contaminated by C_2 lines. With the PGOPHER program (Western 2014) and using spectroscopic constants from the literature (Lloyd & Ewart 1999), we can simulate and identify most of the strong C_2 lines originating from the (0,0) and (1,1) Swan bands.

In addition to the spectral features associated with the absorption lines of these diatomic radicals, some of the recorded spectra are overlaid by absorption features of unknown origin, which, due to their isolated nature, may be connected to atomic lines. These features, that will be indicated by hashes (#), are, in some cases, detected as reduced absorptions, hinting at amplified spontaneous emission or laser-induced fluorescence features. Because we failed to assign those features, they will be treated as artifacts in the following. We note here that the presently reported spectra were recorded over a 5-year interval (2010–2015) and a number of bands were fully reproduced using independently produced gas mixtures from which we conclude that these ‘artifacts’ are not due to measurement issues but are reproducible spectral features associated with atomic or molecular absorption or emission, although unassigned.

4.3 Results

The survey covers the 18 950–21 100 cm^{-1} ($\sim 527\text{--}473$ nm) range and comprises a large number of bands. For each isotopologue, eight individual bands (seven for C_6D) have been unambiguously assigned. In the case of C_6H , eleven additional bands have been recorded that exhibit very different spectral features. The assignments to C_6H , $^{13}\text{C}_6\text{H}$, and C_6D are based on a rotational analysis of the bands where it is assumed that in the cold jet expansion, the population is only retained in the lowest spin-doublet of the $\text{X}^2\Pi$ state, for both $^2\Pi_{3/2}$ and $^2\Pi_{1/2}$ components, and in the very low lying $\mu^2\Sigma$ Renner-Teller component of the ν_{11} bending vibration. For these ground states, accurate molecular constants are available from microwave data (Pearson et al. 1988, Linnartz et al. 1999, Gottlieb et al. 2010) except for the $^{13}\text{C}_6\text{H}$ isotopologue for which the ground state constants were determined optically (Zhao et al. 2011a) and via isotopic scaling. The use of the available information allows us to identify the character of the lower state of the bands. As for the assignment of the excited state vibrational levels, this is based on neon matrix spectra (Forney et al. 1995, Freivogel et al. 1995, Nagarajan & Maier 2010) in combination with *ab initio* calculations (Doyle et al. 1991, Liu et al. 1992, Sobolewski & Adamowicz 1995, Brown et al. 1999, Cao & Peyerimhoff 2001).

In Fig. 4.1 an overview of the band origins of all the observed optical absorption bands is shown for the three species studied here: regular C_6H , $^{13}\text{C}_6\text{H}$, and C_6D . Connected by dotted lines, the corresponding bands in the zoom-in (upper panel) of Fig. 4.1 show a similar pattern for each of the three isotopologues. These isotopic shifts further guide in identifying the absorbing species. The labels with Roman numerals I–XIX in the figure correspond with those used in the sections below and in Table 4.2 and are based on the order at which the bands appear in the overall spectrum. A substantial number of the observed bands has been recorded at rotational resolution and for many of these bands accurate molecular parameters have been derived using PGOPHER. The bands were described by either a $^2\Pi - ^2\Pi$ or a $^2\Sigma - ^2\Sigma$ transition (see below). For the rotational and fine structure analysis, we adopt the effective Hamiltonian of a diatomic molecule, which may be used for transitions in a linear polyatomic molecule such as C_6H . The fitting routine takes ground state values for the rotational constant B'' , the centrifugal distortion constant D'' , the spin-orbit constant A'' , and the spin-rotation constant γ'' ; these parameters are kept fixed in optimizing the excited state values. With the exception for the origin band (Bands I and II) and for the next vibronic band (Band III), we assume $D' \approx D''$: $1.35 \times 10^{-9} \text{ cm}^{-1}$ (C_6H) and $1.2 \times 10^{-9} \text{ cm}^{-1}$ ($^{13}\text{C}_6\text{H}$ and C_6D). As in the plasma jet, particularly, lower lying rotational levels are probed, an independent fit of D' is not possible for the majority of the bands presented here.

The resulting values are summarized in Table 4.2. For some bands a rotational analysis could not be performed, either due to a poor signal-to-noise ratio, overlapping features from other species, or due to lifetime broadening. For these cases only approximate molecular constants are reported.

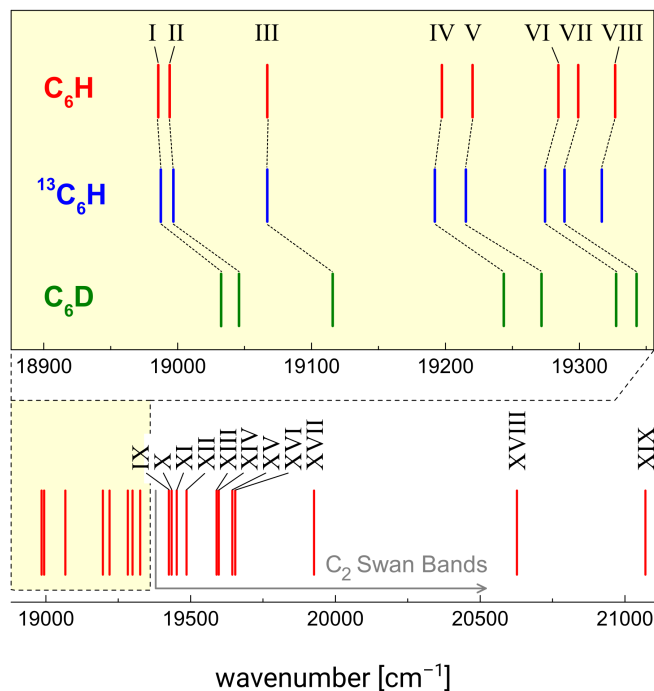


Figure 4.1: Stick diagram denoting the positions of all the observed bands in the 18 950 – 21 100 cm^{-1} range for C_6H (in red, lower panel). The corresponding bands for $^{13}C_6H$ (blue) and C_6D (green) are shown in the zoomed portion (upper panel) and are connected with dotted lines. The area with overlapping C_2 Swan transitions is indicated.

Bands I and II: $0_0^0 B^2\Pi_{\Omega}-X^2\Pi_{\Omega}$ origin band

Fully resolved rovibronic spectra of the $B^2\Pi-X^2\Pi$ origin band transition have been reported before (Linnartz et al. 1999, Zhao et al. 2011a, Bacalla et al. 2015). Figure 4.2 shows the cavity ring-down spectra of C_6H , $^{13}C_6H$, and C_6D . The spectra are repeated for completeness and as an introduction to the interpretation of the other $^2\Pi-^2\Pi$ bands presented later.

In each spectrum two spin-orbit components of a band system are shown, corresponding to the $(0,0)$ band origin of the $B^2\Pi_{3/2}-X^2\Pi_{3/2}$ (left of T_0) and $B^2\Pi_{1/2}-X^2\Pi_{1/2}$ (right) transition. Each component displays largely rotationally resolved P and R branches. In the $B^2\Pi_{3/2}-X^2\Pi_{3/2}$ case, the Q branch is clearly visible; in the $B^2\Pi_{1/2}-X^2\Pi_{1/2}$ case it is much harder to discriminate. The two subbands are split by the difference in spin-orbit splitting in ground and electronically excited state, $A' - A''$.

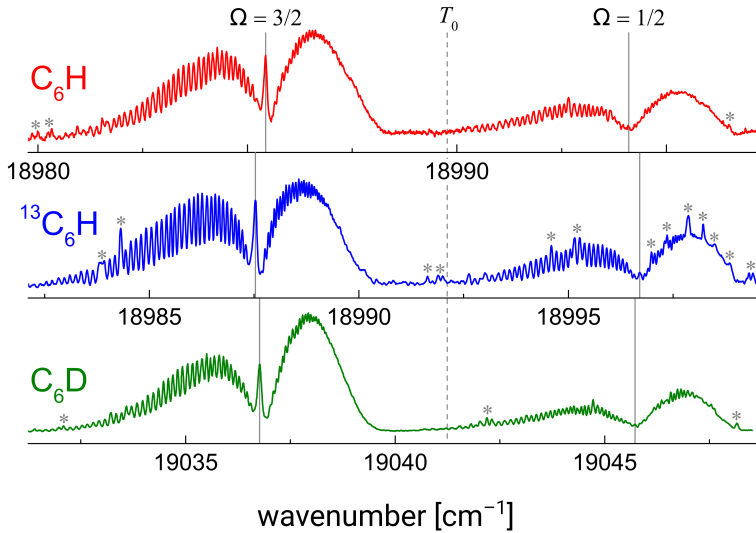


Figure 4.2: $B^2\Pi-X^2\Pi$ electronic origin band (referred to as Bands I and II) of C_6H , measured with a slit plasma nozzle, with the fully ^{13}C -substituted and the deuterated isotopologue. All three spectra, measured in the slit jet configuration, are plotted here on the same scale with their band origins aligned (denoted by T_0). Peaks marked with an asterisk (*) are blended transitions from smaller species.

Depending on whether this number is positive or negative, the $B^2\Pi_{3/2}-X^2\Pi_{3/2}$ component is situated to lower or higher energy of the $B^2\Pi_{1/2}-X^2\Pi_{1/2}$ component, assuming that both ground state and excited state have a regular or inverted spin-orbit splitting. As the intensity of the Q branch scales with Ω^2 , it is clear that the lower energy component corresponds with the $B^2\Pi_{3/2}-X^2\Pi_{3/2}$ system (Linnartz et al. 1999). Also, a full rotational analysis (results presented in Table 4.2) shows that the band gap amounts to roughly $10B$, with B as the rotational constant, instead of $6B$ as typical for the $B^2\Pi_{1/2}-X^2\Pi_{1/2}$ band. As a consequence the assignment of the two bands is straightforward and in combination with microwave data (Pearson et al. 1988) the spin-orbit splittings are set as an inverted system with $A'' = -15.04 \text{ cm}^{-1}$ and $A' = -23.69 \text{ cm}^{-1}$. Based on these numbers and the overall pattern, it is also possible to derive the spin-orbit and rotational temperatures for our plasma settings, yielding 13–22 K.

These findings apply with approximately the same values to all three species. The fitting of the observed spectra is rather straightforward as very precise microwave constants are available to characterize the electronic ground state, but only for the case of

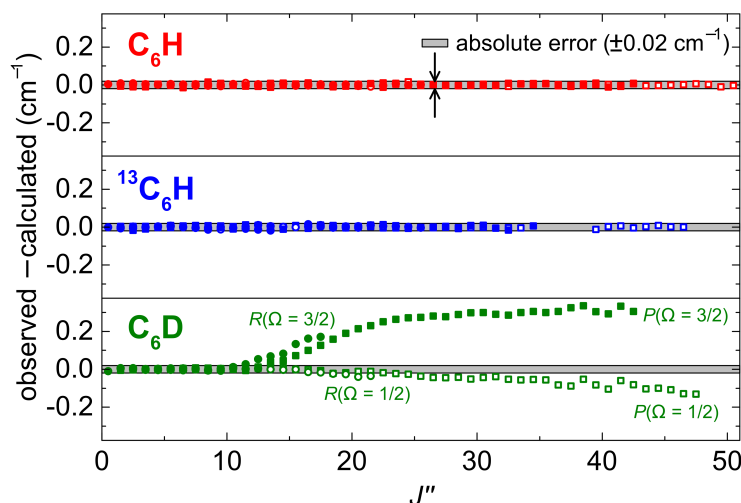


Figure 4.3: Residuals plotted for each of the observed rotational transitions in the electronic origin band. Squares (\square) denote P branch lines and circles (\circ) to R branch lines, with the filled symbols referring to $\Omega = 3/2$ and open symbols to $\Omega = 1/2$. Notice that for both C_6H and $^{13}C_6H$, residuals fall within the uncertainty margins while in C_6D they deviate for higher J'' .

C_6H and C_6D (Linnartz et al. 1999). Because there are no ground state constants for the $^{13}C_6H$ species from microwave or infrared spectroscopy, both the upper and the lower energy levels of the $B^2\Pi-X^2\Pi$ (0,0) transition are optimized in the fitting (Bacalla et al. 2015), and the resulting ground state molecular constants will be used for the simulation and fitting of the other $^{13}C_6H$ bands.

In previous work extensive lists with line positions have been given for these bands and using PGOPHER accurate molecular parameters have been derived for C_6H and C_6D (Zhao et al. 2011a), as well as for the ^{13}C -substituted species (Bacalla et al. 2015). The molecular constants are collected in Table 4.2. Shown in Fig. 4.3 are the differences between the observed and calculated (o-c) values which are derived from these line lists (Supporting Information, available online at <https://pubs.acs.org/doi/suppl/10.1021/acs.jpca.6b06647>). When the behaviors of the residuals for the three molecules are compared, the o-c values of C_6D deviate outside the experimental uncertainty. For $J'' > 15.5$ (10.5) in the $B^2\Pi_{3/2}-X^2\Pi_{3/2}$ ($B^2\Pi_{1/2}-X^2\Pi_{1/2}$) component, residuals can become an order of magnitude larger than the absolute uncertainty of $\pm 0.02 \text{ cm}^{-1}$. The deviation for the $B^2\Pi_{3/2}-X^2\Pi_{3/2}$ component starts early on and goes to a much larger value as compared to that of the $B^2\Pi_{1/2}-X^2\Pi_{1/2}$ component. This behavior is indicative of a perturbation of the excited state level structure in C_6D .

Band III: $\{11\}_1^1 \mu^2\Sigma - \mu^2\Sigma$ vibronic band

First among the newly recorded vibronic spectra is the $\{11\}_1^1 \mu^2\Sigma - \mu^2\Sigma$ transition of $^{13}\text{C}_6\text{H}$, highlighted in the middle panel of Fig. 4.4. Although this band exhibits clearly discernible *P* and *R* branches, no *Q* branch is observed, indicative of a $\Sigma - \Sigma$ type of transition, which does not allow for a change of electronic angular momentum and, thus, $\Delta J = 0$ is forbidden (Herzberg 1950). For C_6H and C_6D corresponding bands have been identified as originating from the $\{11\}_1^1 \mu^2\Sigma - \mu^2\Sigma$ vibronic hot band, and full rotational and Renner-Teller (RT) analyses have been presented previously (Zhao et al. 2011a). Here we use the information from the rotational analysis of C_6H and C_6D to fit the $^{13}\text{C}_6\text{H}$ line positions. First a spectral simulation using the C_6H constants, after isotopic scaling, is used to assign the individual $^{13}\text{C}_6\text{H}$ transitions. These are then included in a fit with PGOPHER using a regular $^2\Sigma - ^2\Sigma$ Hamiltonian, yielding the $^{13}\text{C}_6\text{H}$ constants. The resulting simulation is shown in Fig. 4.4.

Apart from the blended absorption lines from small species, the fit reproduces the experimental spectrum convincingly, including the irregular features in the *P* branch and the bump in the *R* branch. We can decompose this fitted curve into two subbands labelled $F_1 - F_1$ and $F_2 - F_2$ to show clearly the doublet *P* and doublet *R* band structure. The $F_1 - F_1$ subband gives rise to $P_1(J)$ and $R_1(J)$ branches and the $F_2 - F_2$ subband to $P_2(J)$ and $R_2(J)$ branches. The overlap of the $P_1(J)$ and $P_2(J)$ branches reproduces the experimentally observed spectral interference and a more intense $R_2(J)$ compared to the $R_1(J)$ branch produces the step-like phenomenon at $19\,068.3\text{ cm}^{-1}$. The relative intensity of the two subbands also confirms the vibronic assignment because different values for the rotational constants result in different band contours. It is interesting to note that in this way the somewhat irregular appearance of Band III can be fully reproduced. The derived molecular constants are listed in Table 4.2.

Band IV: $\{10\}^1\{11\}_1 \mu^2\Sigma - \mu^2\Sigma$ vibronic band

A well resolved spectrum of this band system (Band IV) is reported for the first time and has been measured for all three isotopologues (Fig. 4.5). The appearances of the band structure for the three isotopologues are very similar, providing confidence in assigning the three spectra to the same band system. Largely resolved *P* and *R* branches are observed at the low and high energy side of an unresolved and structureless feature, more or less at the position where a *Q* branch might be expected. However, in a simulation it can be shown that these unresolved features are due to the $R_2(J)$ branch of the $F_2 - F_2$ component in a $^2\Sigma - ^2\Sigma$ band. The intensities of these unresolved features scale with that of the *P* and *R* branches and must, therefore, be part of this band system.

The different appearance, compared to Band III, is caused by a larger ratio between the effective spin-rotation constant γ and the effective *B* rotational constant (Table 4.2), causing the lines in the $R_2(J)$ branch to move closer together, forming a band head that is uncommon for low rotational temperatures. This is illustrated in

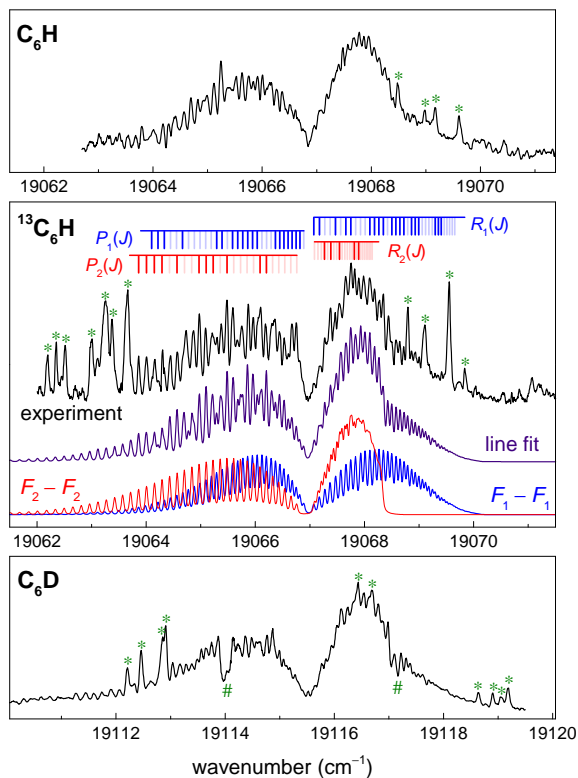


Figure 4.4: The $\{11\}_1^1 \mu^2 \Sigma - \mu^2 \Sigma$ vibronic band (Band III), for all three isotopologues measured in the slit jet configuration. For each branch, the lines are assigned with heavy tick marks. Blended lines from small species are marked with asterisks (*). Dips, that are reproduced in independent scans, are present in the C_6D spectrum and are marked with hashes (#). Rotational analyses of C_6H and C_6D spectra have been presented by [Zhao et al. \(2011a\)](#).

Fig. 4.5 where the fits of the individual subbands as well as the composite spectrum are shown. Despite these overlapping transitions, it is possible to assign some of the rotational levels and perform a fit. This is possible because at the low energy side the $P_2(J)$ transitions contribute largely to the intensity, whereas at the high energy side the $R_1(J)$ branch is the sole contributor to the spectrum. In the experimental spectrum the individual rotational lines are largely resolved and these are well reproduced by the fitted spectrum. This even applies to the overlapping rotational structure in the energy region just at the low-energy side of the $R_2(J)$ band head.

The observed spectra are well reproduced using the corresponding ground state constants derived for Band III, confirming that Band IV originates from the same

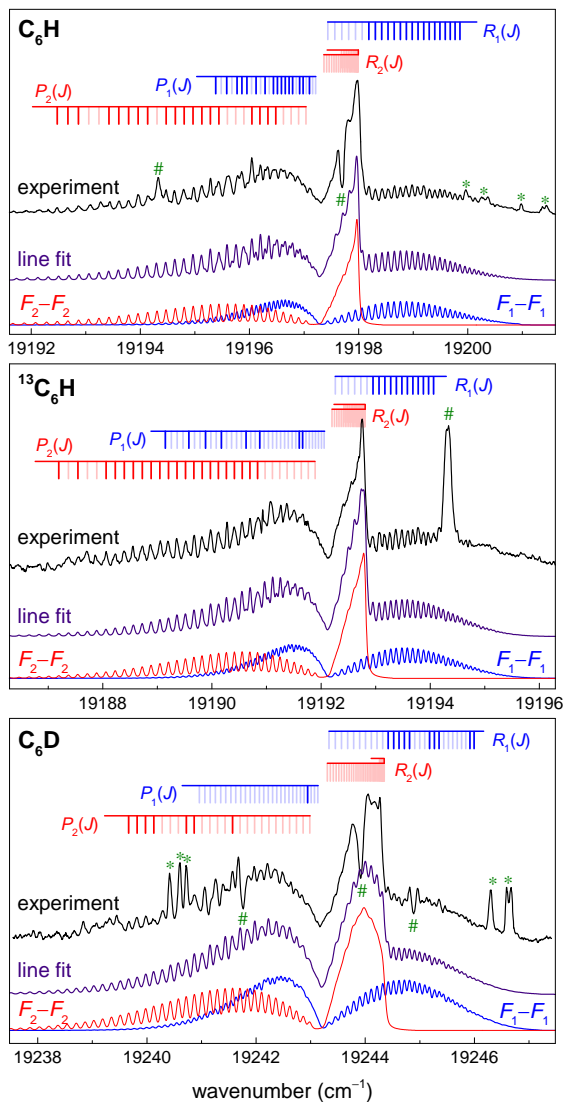


Figure 4.5: Recording of the $\{10\}^1\{11\}_1 \mu^2\Sigma - \mu^2\Sigma$ vibronic band (Band IV) for C_6H (upper), $^{13}\text{C}_6\text{H}$ (middle), and C_6D (lower). Both spectra for C_6H and C_6D were measured using the slit nozzle configuration. For $^{13}\text{C}_6\text{H}$ the pinhole nozzle configuration was used with an admixture of argon gas to reduce Doppler broadening. Blending absorptions from smaller species are marked with asterisks (*). For features marked with a hash (#), see text.

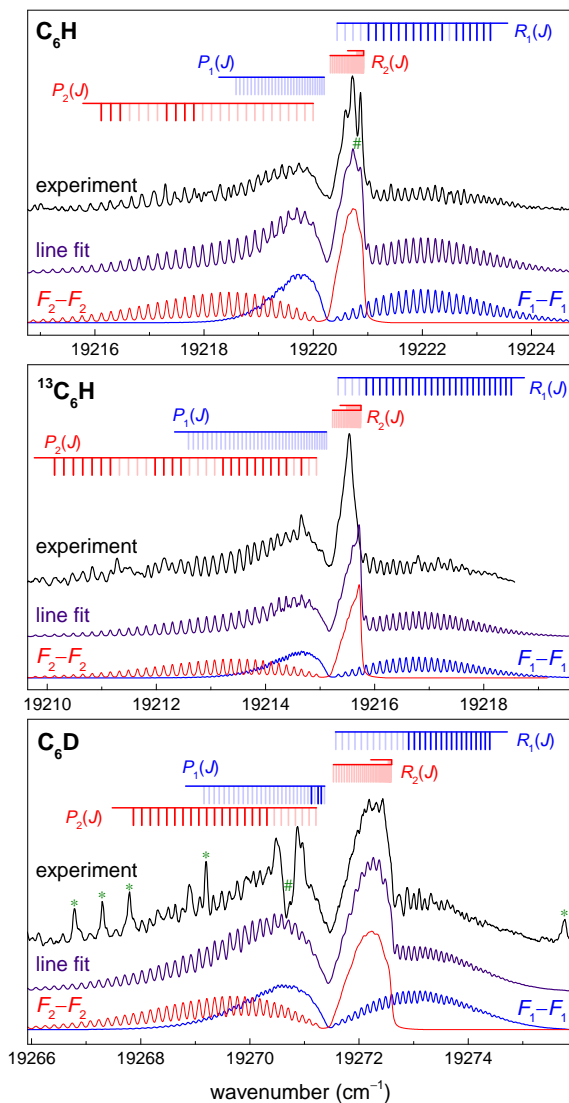


Figure 4.6: Band V assigned as the $\{10\}^1\{11\}_1 \kappa^2\Sigma - \mu^2\Sigma$ transition. Again, distinct dips (marked with #) show up in the spectra which cannot be accounted for in the rotational line fit.

$\{11\}_1 \mu^2\Sigma$ state. Also the relative intensities of the subbands $F_1 - F_1$ and $F_2 - F_2$ further support this assignment. It should be noted, though, that for C_6H and C_6D , a narrow depletion in the absorption signal has been found in the $R_2(J)$ band head region that is not reproduced in the fit. Should this be a perturbation in the upper rotational states, a corresponding dip should show up in the P branch, but this is not observed. A simulation of the spectra for C_6H and C_6D including these anomalies, marked by a hash (#), turned out to be impossible. In the same way for $^{13}C_6H$ a strong and broad line shows up around 19194.3 cm^{-1} with unclear origin. Incidentally the strong line in $^{13}C_6H$ coincides with a small peak in the C_6H spectrum, at exactly the same frequency, both marked by a hash (#), again indicative of the same feature of unknown origin; an assignment is not possible at this moment. The molecular constants for this band are collected in Table 4.2.

Band V: $\{10\}^1\{11\}_1 \kappa^2\Sigma - \mu^2\Sigma$ vibronic band

Band V (Fig. 4.6) is another well resolved spectrum with a band contour that is very much like Band IV, which strongly suggests that a similar type of electronic transition ($^2\Sigma - ^2\Sigma$) is taking place. With a number of resolved transitions a rotational line fit can be performed, yielding the molecular constants as listed in Table 4.2. The simulations reproduce the lines and the overall contour, although for $^{13}C_6H$ the peak of the central spectral feature is slightly off by $\sim 0.2 \text{ cm}^{-1}$ to higher energy. The vibrational assignment of Band V in connection with Band IV is described in the Discussion section.

Band VI: $\mu^2\Sigma - \mu^2\Sigma$ vibronic band

The spectra, assigned to Band VI and recorded in the slit jet configuration, are presented in Fig. 4.7. At first glance the contour of Band VI is reminiscent of Band III, rather clearly for C_6H and C_6D , pointing to a $^2\Sigma - ^2\Sigma$ transition. For C_6H , having the best S/N for this band, a fit to the rotational structure is very possible using the ground state constants obtained for the Renner-Teller $\mu^2\Sigma$ ground state. Again the intensity in the R branch is most pronounced and also the intensity drop at 19285.4 cm^{-1} can be understood as a result of the contribution by the $F_1 - F_1$ and $F_2 - F_2$ subbands. The spectrum for C_6H has a single artifact feature denoted by a hash (#), while the spectra of C_6D and $^{13}C_6H$ are overlaid by multiple artifact features and extra lines associated with small radicals, denoted by asterisks (*).

Given the low S/N, for the $^{13}C_6H$ and the C_6D spectrum a good line fit is not possible for molecular constants isotopically scaled from the main C_6H isotopologue. Moreover, anomalous band features make it harder to identify and assign rotational lines. The lack of individually resolved rotational transitions necessitates a contour simulation using the known ground state values and tuning the excited state parameters together with the rotational temperature until the overall shape of the band is matched. Clearly, results obtained using this procedure will not be as precise as the results from

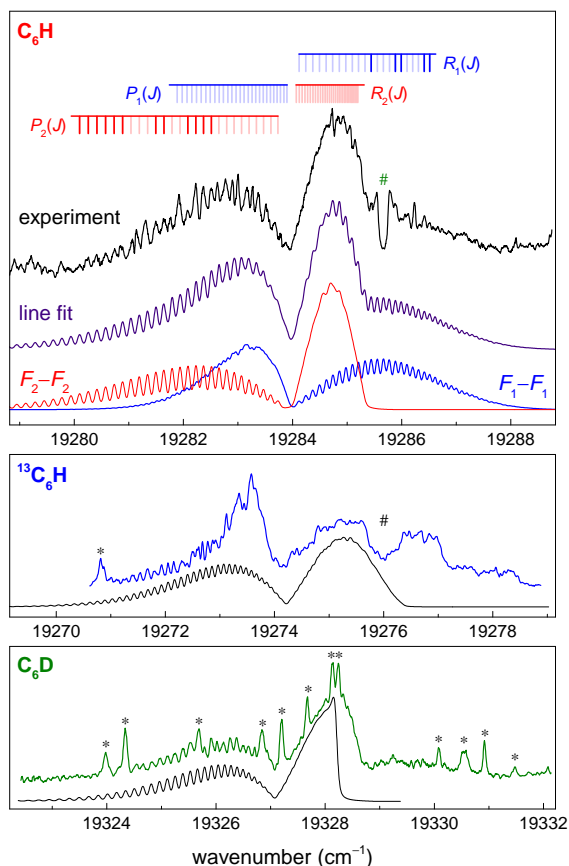


Figure 4.7: Band VI assigned as a $^2\Sigma - ^2\Sigma$ transition. All three spectra were recorded using the slit nozzle configuration. Shown in the upper panel is a rotational line fit done for C_6H with the two band components. For $^{13}C_6H$ and C_6D a band contour simulation (in black) was performed. Features denoted by asterisks (*) and hashes (#) are discussed in the main text.

a line fit. So as an additional criterion to verify the correct simulation of the spectrum, the spacing between individual (but unassignable) rotational lines has been matched, typically in the P branch.

The spectrum for C_6D is overlaid by a number of sharp lines (marked by *). If this is taken into account, the contour fit yields a reasonable simulation of the observed spectrum, although the sharp drop in the simulated intensity of the R branch is not clearly reproduced.

Of the three spectra, the $^{13}C_6H$ spectrum exhibits the most severe anomalies,

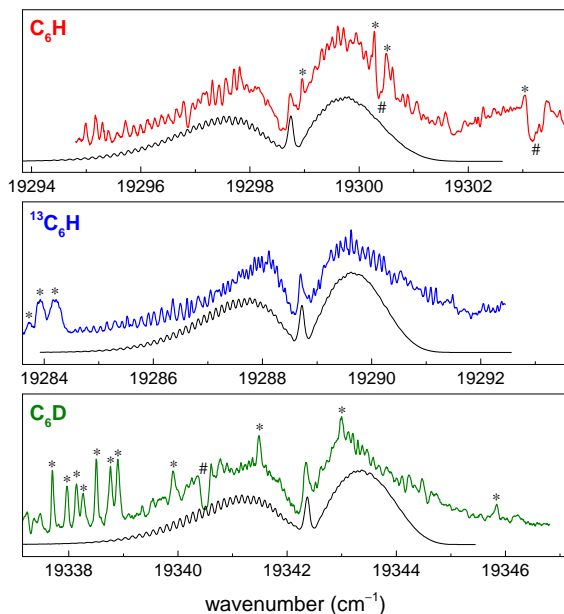


Figure 4.8: Spectral recordings of Band VII, here identified as a ${}^2\Pi - {}^2\Pi$ transition. All spectra were recorded using the slit nozzle configuration. Again blended lines (*) and dips (#) are visible in the spectrum. Simulated band contours are shown in black.

which makes it less straightforward to obtain a proper band contour simulation. The increased intensity in the P branch near $19\,273.5\text{ cm}^{-1}$ might be associated by the spectral lines of small radicals contributing to the intensity, although no sharp and distinct lines are visible. In the R branch of ${}^{13}\text{C}_6\text{H}$, a double broad feature appears; this could be due to an artifact dip (marked by #) or it may well be that the second feature is caused by a different species because it is rather outside the simulated intensity pattern. In any case the observed spectrum deviates quite distinctively from a constructed band contour as shown in the figure, and so the resulting constants should be treated with care.

The molecular constants obtained from a fit of the C_6H spectrum and a band contour simulation for C_6D and ${}^{13}\text{C}_6\text{H}$ are listed in Table 4.2.

Band VII: $B^2\Pi_Q - X^2\Pi_Q$ vibronic band

Spectra of Band VII, recorded in the slit jet configuration for all three isotopologues, are displayed in Fig. 4.8. The overall shapes of the band structures for the three isotopologues are similar, which forms the basis for assigning these spectral

features to the same band. In the band gap region between the P and R branches a clear peak reminiscent of a typical Q branch is found. In the spectra for C_6H and C_6D some additional lines associated with small radicals (marked with *) are visible as well, and their shapes are somewhat similar to the Q branch feature. However, because these extra lines do not occur in the spectrum for $^{13}C_6H$ and the location of the Q branch is in all cases at the appropriate frequency, the identification of a Q branch feature is unambiguous. Hence, Band VII is assigned as $^2\Pi - ^2\Pi$.

As was discussed in previous studies of the $^2\Pi - ^2\Pi$ band origin transition in C_6H (Linnartz et al. 1999), the Q branch is most visible for the $\Omega = 3/2$ spin-orbit component, while it is hardly visible for $\Omega = 1/2$; this intensity relationship is exemplified in the origin band (Fig. 4.2). Detailed inspection of the recorded Q branches of Band VII for all isotopologues shows that all three are somewhat blue-degraded, unlike in the case of the origin band, where the Q branches are red-degraded. Such a line shape is difficult to explain. A possible rationale is that the two spin-orbit components of the transition, hence $^2\Pi_{3/2} - ^2\Pi_{3/2}$ and $^2\Pi_{1/2} - ^2\Pi_{1/2}$, are overlapped with each other to some extent, which further implies that for this transition, $A' \approx A''$. A similar situation applies to other species, like HC_6H^+ and HC_8H^+ , where transitions starting from both spin-orbit components coincide and differences are only visible for higher rotational temperatures (Pfluger et al. 2000). In principle, it is also possible that A'' increases, and for a similar spin-orbit temperature, this means that the population in the $\Omega = 1/2$ state decreases. This is not expected, as the ground state splitting should be the same for all $^2\Pi - ^2\Pi$ transitions studied here. The constructed contours, shown in black in Fig. 4.8, are based on this assumption. In all three cases the observed spectra are reasonably well reproduced in the contour fits and the underlying molecular constants are listed in Table 4.2.

Band VIII : $B^2\Pi_{3/2} - X^2\Pi_{3/2}$ vibronic band

Figure 4.9 displays the spectra of Band VIII recorded for C_6H and $^{13}C_6H$. Band VIII was not recorded for C_6D since in the energy region beyond $\sim 19\,350\text{ cm}^{-1}$, where this band is expected (see also Fig. 4.1), the spectra are covered by very strong absorptions from the C_2 Swan bands.

Again, as in the case of Band VII, the spectra are characterized by the presence of a pronounced Q branch, the reason for assigning this band to a $^2\Pi - ^2\Pi$ type transition. This time, the Q branch lies more to the P branch side, and the line shape of the Q branch is red-degraded, which is an indicator for a $^2\Pi_{3/2} - ^2\Pi_{3/2}$ transition. Indeed both spectra for C_6H and $^{13}C_6H$ can be well reproduced by a contour simulation. Values obtained from the contour simulation are listed in Table 4.2.

Bands IX and X : $B^2\Pi_{\Omega} - X^2\Pi_{\Omega}$ vibronic band

In the narrow frequency window at $19\,420 - 19\,440\text{ cm}^{-1}$ two more absorption bands are found that are heavily overlaid by strong resonances from C_2 . With molec-

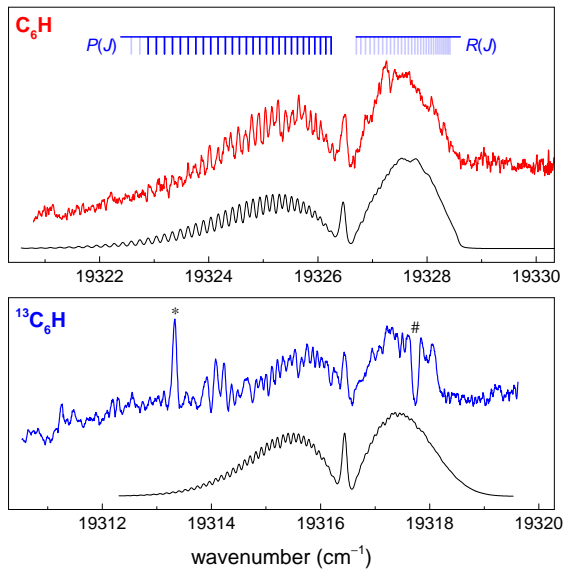


Figure 4.9: Spectra for Band VIII, assigned as the $\{9\}_0^1 B^2\Pi_{3/2}-X^2\Pi_{3/2}$ transition, recorded for C_6H in the slit nozzle configuration and for $^{13}C_6H$ in the pinhole nozzle configuration. Simulated band contours are shown in black.

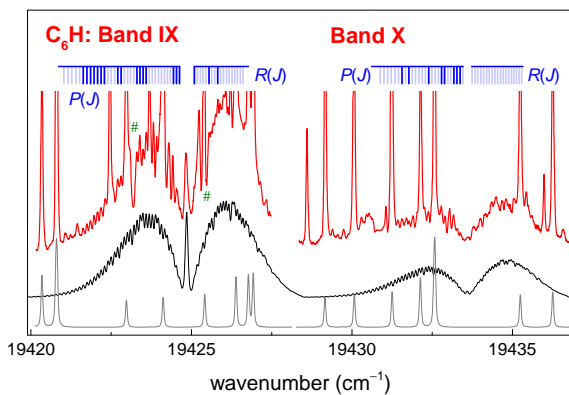


Figure 4.10: Bands IX and X of C_6H measured in a slit jet plasma configuration and a rotational line fit for a $^2\Pi_{\Omega}-^2\Pi_{\Omega}$ band for both $\Omega = 3/2$ and $1/2$ components. At the bottom of the figure a simulated spectrum of overlapping C_2 Swan transitions is plotted.

ular constants from the literature (Lloyd & Ewart 1999), these blending peaks can be attributed to the (0,0) origin band of the Swan system of C_2 . This simulation and together with the spectra recorded in the slit jet configuration are displayed in Fig. 4.10. The observed bands (Bands IX and X) have the shape of a $^2\Pi_{\Omega}-^2\Pi_{\Omega}$ pair: very similar to bands I and II. Band IX has a narrow resonance at 19424.9 cm^{-1} , which is not reproduced by a Swan band line like most of the other sharp resonances observed. This resonance, identified as a Q branch, is centered in between apparent P and R branch features. Following the argument, as for Bands I and II, that the $\Omega = 3/2$ component exhibits a much stronger Q branch than the $\Omega = 1/2$ component, a contour fit can be produced for the combined $^2\Pi_{\Omega}-^2\Pi_{\Omega}$ bands using the ground state rotational constant and spin-orbit constants $A'' = -15.04$ and $A' = -23.77\text{ cm}^{-1}$. The agreement of the excited state spin-orbit constant A' with that of the band origin ($A' = -23.69\text{ cm}^{-1}$) provides confidence for a positive assignment of these bands. It is noted that these bands were presented previously in a PhD-thesis by Denisov (2006), employing cavity ring-down spectroscopy, where the bands were also assigned as a $^2\Pi_{\Omega}-^2\Pi_{\Omega}$ pair. Similarly as in the previously presented vibronic bands, dips show up in the spectra which cannot be reproduced in a fit.

Band XI: $B^2\Pi_{3/2}-X^2\Pi_{3/2}$ vibronic band

A recording of Band XI, presented in Fig. 4.11, is assigned as $^2\Pi_{3/2}-^2\Pi_{3/2}$ due to the presence of a Q branch. Again the spectrum in this energy range is overlaid by strong resonances due to C_2 Swan (0,0) band absorption, but the prominent absorption feature at 19451.8 cm^{-1} does not coincide with a predicted C_2 line and is therefore identified as the Q branch. A number of well-resolved rotational lines in the P and R branches allows for a fit yielding a rotational constant that is indicative of C_6H (Table 4.2). The associated $^2\Pi_{1/2}-^2\Pi_{1/2}$ spin-orbit component could not be observed.

Band XII: $^2\Sigma-^2\Sigma$ vibronic band

Figure 4.12 shows a recording of a band centered at 19486 cm^{-1} . In a previous study this band feature was associated to the $^2A''-X^2A''$ electronic transition of the $C_4H_4^+$ cation (Araki et al. 2004), whereas in another study, it was identified as a $^3\Sigma^--X^3\Sigma^-$ transition of the C_6H^+ cation (Raghunandan et al. 2010). Because the spectrum is overlaid by a number of strong and sharp C_2 Swan transitions, particularly in the region where a Q branch of a possible $^2\Pi_{3/2}-^2\Pi_{3/2}$ transition of C_6H may be expected, an unambiguous assignment of this band is difficult. Several band contours were simulated, and by imposing a transition of $^2\Sigma-^2\Sigma$ symmetry and keeping the ground state fixed at values for the $\mu^2\Sigma$, Band XII can be well reproduced with excited state constants ($B' = 0.04552\text{ cm}^{-1}$ and $\gamma' = 12.9 \times 10^{-3}\text{ cm}^{-1}$) matching those of C_6H . The fact that the observed interference between simulated P branches for both $F_1 - F_1$ and $F_2 - F_2$ subbands at $\sim 19484.6\text{ cm}^{-1}$ is reproduced in the simulated

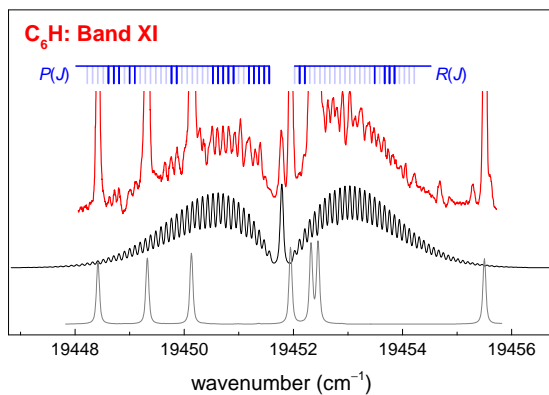


Figure 4.11: Recording of Band XI of C₆H in a slit jet plasma configuration and a rotational line fit assuming a $^2\Pi_{3/2} - ^2\Pi_{3/2}$ transition.

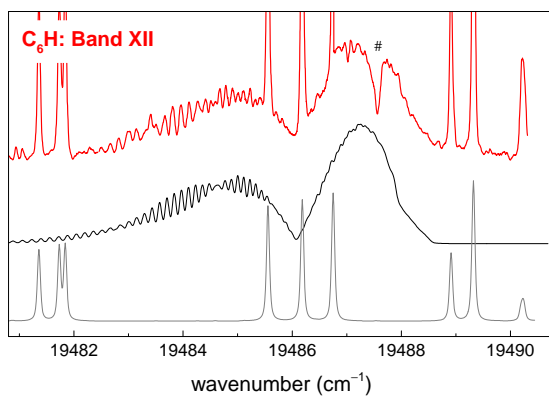


Figure 4.12: Bands XII of C₆H measured in the slit plasma nozzle configuration. A simulated contour spectrum of a $^2\Sigma - ^2\Sigma$ transition is plotted in black. The sharp absorption features can be identified as C₂ Swan band lines for bands (0,0) and (1,1) bands (in gray).

spectrum lends credit to the assignment of this band to a $^2\Sigma - ^2\Sigma$ feature and to assign the C_6H molecule as its carrier. It is interesting to note that the distinctive dip in the R branch at 19487.6 cm^{-1} in Fig. 4.12, indicated by #, was also observed in the aforementioned studies (Araki et al. 2004, Raghunandan et al. 2010). This again demonstrates that these features of decreased absorption are not just artifact features.

Bands XIII and XIV: $B^2\Pi_\Omega - X^2\Pi_\Omega$ vibronic band

In the frequency range $19\,587 - 19\,600\text{ cm}^{-1}$ another composite band feature has been observed which again is heavily overlaid by sharp C_2 (0,0) and (1,1) Swan band transitions. The spectrum (Bands XIII and XIV), presented in Fig. 4.13, displays the appearance of a $^2\Pi_\Omega - ^2\Pi_\Omega$ pair. Like for the other $^2\Pi_\Omega - ^2\Pi_\Omega$ pairs the $\Omega = 3/2$ component (Band XIV) exhibits an identifiable Q branch visible at $\sim 19\,596.5\text{ cm}^{-1}$, while the other subband feature (Band XIII) does not display such a pronounced Q branch. However, at this location a weak C_2 line is predicted in the simulation, so the assignment of the C_6H bands remains tentative. In addition the order of the spin-orbit components in the putative $^2\Pi$ -doublet is reversed, i.e., $\Omega = 1/2$ falls at lower energies than the $\Omega = 3/2$ component. The molecular constants used for producing the simulated spectrum for the corresponding C_6H features are listed in Table 4.2.

Bands XV and XVI: $\{6\}_0^1\ ^2\Pi_\Omega - ^2\Pi_\Omega$ vibronic band

In the frequency range $19\,638 - 19\,656\text{ cm}^{-1}$ two sequential bands have been observed for C_6H in the slit jet discharge expansion. The spectrum, displayed in Fig. 4.14, is of low signal-to-noise and overlaid with pronounced sharp resonances due to C_2 Swan band lines. By itself the identification of the features remains somewhat unclear, in particular because the intensity of the $^2\Pi_{1/2} - ^2\Pi_{1/2}$ component exhibits about the same intensity as the $^2\Pi_{3/2} - ^2\Pi_{3/2}$ component. Additional measurements using the pinhole configuration and detecting these bands downstream from the plasma expansion show that the intensity of the $^2\Pi_{1/2} - ^2\Pi_{1/2}$ component did not drop in a fashion similar to that of the $^2\Pi_{1/2} - ^2\Pi_{1/2}$ component of the origin band, as was shown by Zhao et al. (2011a). The same features were also observed in the hollow cathode discharge experiment (Kotterer & Maier 1997) and there they were assigned to a $\{6\}_0^1\ ^2\Pi_\Omega - ^2\Pi_\Omega$ transition, based on a comparison with matrix data. From a contour simulation of the spectrum it follows that both subbands, pertaining to $\Omega = 3/2$ and $\Omega = 1/2$ components, can be reproduced with spin-orbit constants $A'' = -15.04\text{ cm}^{-1}$ and $A' = -24.4\text{ cm}^{-1}$ and rotational constants $B'' = 0.04640497\text{ cm}^{-1}$ and $B' = 0.0460\text{ cm}^{-1}$. This provides support for a definitive assignment of Bands XV and XVI to $6_0^1\ ^2\Pi_\Omega - ^2\Pi_\Omega$ in C_6H .

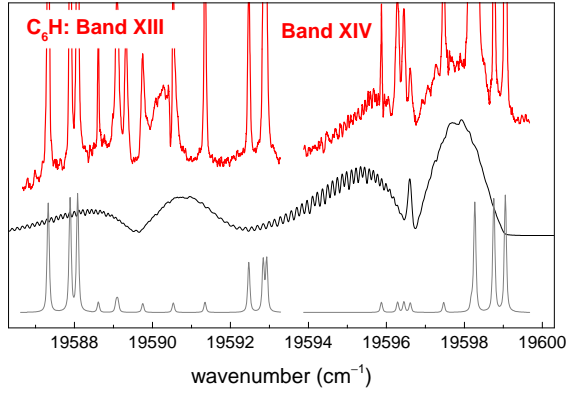


Figure 4.13: Bands XIII and XIV of C_6H measured in the slit plasma jet configuration with a simulated spectrum based on a $^2\Pi_\Omega - ^2\Pi_\Omega$ pair with the $\Omega = 1/2$ component at lower energies. The sharp and intense absorption peaks arise from C_2 (0, 0) and (1, 1) Swan bands (in gray).

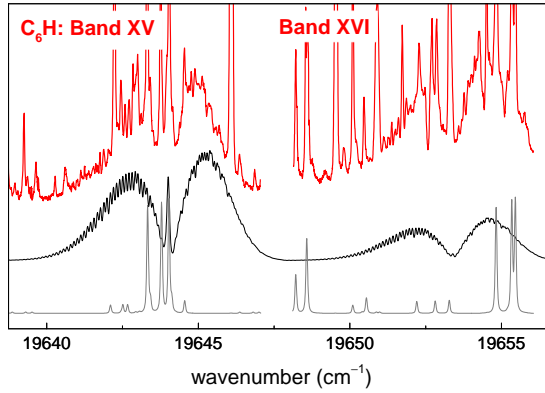


Figure 4.14: Bands XV and XVI of C_6H measured with a slit plasma nozzle. The blended absorption peaks arise from C_2 (0, 0) and (1, 1) Swan bands (in gray).

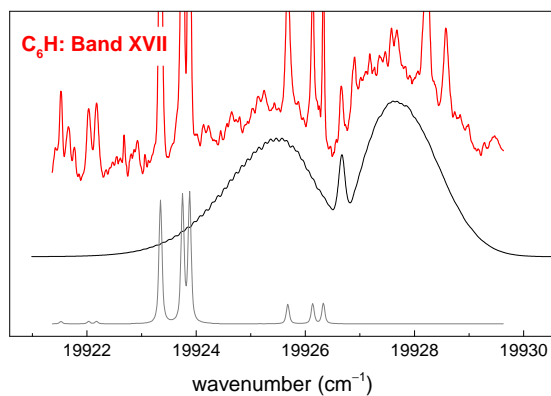


Figure 4.15: Band XVII of C_6H measured with the slit jet plasma configuration and a simulation based on a $^2\Pi_\Omega - ^2\Pi_\Omega$ band type. The narrow absorption peaks arise from C_2 (0, 0) and (1, 1) Swan bands.

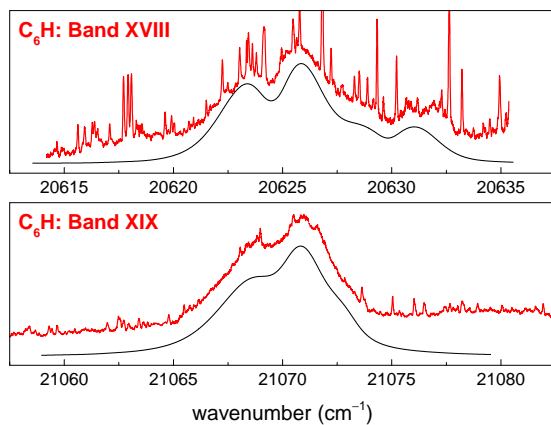


Figure 4.16: Bands XVIII and XIX of C_6H measured with a slit plasma nozzle and a contour simulation of the spectrum (in black). Note that the wavenumber axis is wider than in the previous figures.

Band XVII: $^2\Pi_Q - ^2\Pi_Q$ vibronic band

The band system in the frequency range $19\,922 - 19\,930\text{ cm}^{-1}$, displayed in Fig. 4.15, is of low quality in terms of signal-to-noise and coverage with sharp resonances associated with C_2 . The assignment of this feature is very tentative: the central rather narrow peak at $19\,926.7\text{ cm}^{-1}$ might be considered as a Q branch and indicative of a $^2\Pi_{3/2} - ^2\Pi_{3/2}$ component. But using a similar argument as with Band VII, based on the position of the Q branch, the spectrum can be simulated by superimposing the two spin-orbit components. Only rough estimates of the T_0 , B' , and A' constants can be given on the basis of a contour analysis, and the corresponding values are listed in Table 4.2.

Bands XVIII and XIX

Finally, in the highest energy region investigated in the present study, in the frequency range above $20\,000\text{ cm}^{-1}$, two bands have been observed, which are shown in Fig. 4.16. Despite the two bands having been measured with a slit plasma nozzle, individual rotational lines of C_6H could not be resolved. The broadening is effective to the extent that the $^2\Pi_{3/2}$ and $^2\Pi_{1/2}$ components are somewhat overlapped, without a distinct Q branch visible. Moreover, the spectra, in particular for Band XVIII, are overlaid by a congested forest of narrow resonances. Assuming a rotational temperature of $\sim 22\text{ K}$, and fixing the ground state constants to those of the $^2\Pi$ ground state of C_6H , a band contour simulation can be produced yielding the molecular constants listed in Table 4.2.

4.4 Discussion

In the present study 19 vibronic (sub)bands pertaining to the $B^2\Pi - X^2\Pi$ electronic system of the C_6H molecule have been observed. For the C_6D isotopologue the seven lowest energy bands have been observed and for $^{13}C_6H$ the eight lowest bands. From the fitting of the recorded spectra, values are derived for the band origins T_0 , effective rotational constants B_{eff} , effective spin-rotation constants γ_{eff} , and, for the case of $^2\Pi$ vibronic states, a spin-orbit coupling constant A_{SO} . For some of the bands, clearly rotationally resolved spectra have been measured and in these cases a fit has been made comparing individual line positions (see Supporting Information for the line lists, available online at <https://pubs.acs.org/doi/suppl/10.1021/acs.jpca.6b06647>). In some additional cases spectra are unresolved or strongly overlaid with narrow spectral features belonging to CH and C_2 radical species. In such cases only a band contour simulation has been produced, for which the uncertainty on the derived spectroscopic parameters is larger.

All the bands investigated are connected to an electronic transition of $^2\Pi - ^2\Pi$ character. If the C_6H molecule were to remain linear in ground and excited state levels then the vibronic absorption bands could all be described as $^2\Pi - ^2\Pi$ transitions

Table 4.1: Calculated eigenfrequencies of the six non-degenerate stretching modes of C_6H as in the four reported *ab initio* studies (Doyle et al. 1991, Liu et al. 1992, Brown et al. 1999, Cao & Peyerimhoff 2001) together with the vibrational frequencies derived from the observed gas-phase vibronic spectrum.

Mode	Doyle et al.	Liu et al.	Brown et al.	Cao & Peyerimhoff	Observed
ν_1	3 659.1	3 609.0	3 448	3 457	...
ν_2	2 436.7	2 197.8	2 109	2 137	1 953.4 ^a
ν_3	2 336.0	2 139.6	2 080	2 105	2 080.8
ν_4	2 092.0	1 974.5	1 872	1 895	1 637.4
ν_5	1 213.0	1 201.8	1 210	1 224	...
ν_6	653.9	638.5	642	650	658.9

^a The observed frequency at $1\,953.4\text{ cm}^{-1}$ is taken from Doyle et al. (1991). All values in cm^{-1} .

in a diatomic molecule. Even if both $^2\Pi$ states would fit a Hund's case(b) description, this would remain the case (Herzberg 1966). If, however, the spin-orbit splitting in a $^2\Pi$ state becomes appreciable, then the bending vibrations couple to the electronic motion, giving rise to doubly degenerate structures and bands that appear as $^2\Sigma - ^2\Sigma$ transitions — a phenomenon known as the Renner-Teller (RT) effect. This holds for the case of a single bending vibration. For the non-degenerate stretching vibrations, this is not the case and the electronic absorption bands retain the character of a $^2\Pi - ^2\Pi$ transition. The same holds for a combination of two degenerate bending vibrations that will also display the character of a $^2\Pi - ^2\Pi$ transition.

The C_6H molecule is the first member of the C_nH series to be linear in the $X^2\Pi$ ground state, in contrast to the smaller chains like C_4H exhibiting a $^2\Sigma^+$ ground state. This was shown in electronic structure calculations by Pauzat & Ellinger (1989) and Sobolewski & Adamowicz (1995) and was found to be consistent with radio astronomical observations (Cernicharo et al. 1987). C_6H is also linear in the vibrationless $B^2\Pi$ excited state as is derived from the gas-phase observation of the $B^2\Pi - X^2\Pi$ origin band spectrum (Linnartz et al. 1999). It has 16 vibrational modes, of which there are 5 doubly degenerate bending modes (in the two perpendicular planes containing the molecular axis) and 6 non-degenerate stretching modes. Four different *ab initio* studies have been reported that calculated the non-degenerate stretching modes along the linear axis of the C_6H backbone (Doyle et al. 1991, Liu et al. 1992, Brown et al. 1999, Cao & Peyerimhoff 2001). The calculated eigenfrequencies of the fundamental modes, as listed in Table 4.1, are in reasonable agreement with each other. Two of the cited works on *ab initio* calculations (Brown et al. 1999, Cao & Peyerimhoff 2001) also include results on the five doubly degenerate bending modes. Energies of the degenerate modes were calculated to exhibit mode frequencies of $100 - 600\text{ cm}^{-1}$, whereas the energies of the nondegenerate modes fall in the range $600 - 3\,500\text{ cm}^{-1}$.

In Fig. 4.17 the fundamental nondegenerate eigenmodes are drawn in the geometry of the C_6H molecule, including calculated bond lengths (Liu et al. 1992, Brown et al. 1999). The highest frequency mode, ν_1 , has the typical frequency of a C–H stretching mode and is assigned as such. The three subsequent modes, ν_2 , ν_3 , and ν_4 , in order of decreasing frequency, are associated with the $C\equiv C$ triple bonds (Fig. 4.17) where the highest frequency is assigned to the mode with the shortest bond length among the three. The two lowest frequencies, ν_5 and ν_6 , are associated with the vibrational motion centered on the C–C single bonds.

These calculations are taken as the basis for assigning the recorded vibronic bands. It should be noted that all four *ab initio* calculations were performed for the ground state electronic configuration, and that we assume the vibrational level structure of the $B^2\Pi$ excited state to reproduce that of the ground state. This is, of course, a rather strong but common assumption. It is noted further that in the study of Brown et al. (1999), ambiguity arises on the identification of the infrared mode observed in the ground state of C_6H at 1953.4 cm^{-1} (Doyle et al. 1991), which is assigned as ν_3 in one of their tables. In another table in the same paper, they still assign this mode to ν_3 but they list a calculated frequency of 2109 cm^{-1} , which corresponds to ν_2 in their previous table. In any case, this IR absorption is identified as the $C\equiv C$ stretching vibration next to the C–H bond (r_2 in Fig. 4.17). In addition, in the photodetachment study by Taylor et al. (1998) a vibrational mode at 2202 cm^{-1} was deduced, which however is associated with a low-lying electronic state of $^2\Sigma^+$ symmetry (Sobolewski & Adamowicz 1995). Although the two bands mentioned pertain to the $X^2\Pi$ and $A^2\Sigma^+$ states, in the matrix studies two bands were observed at 21645 cm^{-1} and 22517 cm^{-1} , corresponding to vibrational excitations of 2791 cm^{-1} and 3664 cm^{-1} in the $B^2\Pi$ state. These bands were tentatively assigned as $\nu_3 + \nu_6$ and $\nu_3 + \nu_5$ combination bands (Freivogel et al. 1995), whereas on the basis of the consistent *ab initio* calculations (Liu et al. 1992, Brown et al. 1999, Cao & Peyerimhoff 2001, Doyle et al. 1991) the higher frequency band might also be associated with ν_1 .

All observed bands originate from the ground vibrational level, starting from the lowest lying $X^2\Pi_{3/2}$ level, or the $X^2\Pi_{1/2}$ spin-orbit component which is excited by $\sim 15.0\text{ cm}^{-1}$, or from the $\mu^2\Sigma$ component of the RT manifold, which is at an excitation energy of $10.7 \pm 0.5\text{ cm}^{-1}$ above the ground level ($X^2\Pi_{3/2}$) (Zhao et al. 2011a). The $\mu^2\Sigma$ component is associated with the lowest $\nu_{11} = 1$ bending vibration in the electronic ground state, which vibronically couples to produce a pair of $^2\Sigma$ states, referred to as a lower $\mu^2\Sigma$ component and a higher lying $\kappa^2\Sigma$ component. This $\kappa^2\Sigma$ component has not yet been observed spectroscopically. Also a pair composed of the $^2\Delta_{5/2}$ and $^2\Delta_{3/2}$ levels follows from the RT coupling, excited at $\sim 50\text{ cm}^{-1}$, which has been observed for C_6H in a microwave study (Gottlieb et al. 2010). In the present study no signature of this $^2\Delta$ pair can be identified.

From a spectroscopic analysis of the rovibronic bands and their treatment in the previous section, it appears that all bands can be described either by a $^2\Pi - ^2\Pi$ or a $^2\Sigma - ^2\Sigma$ type transition. In the following, all available data are merged with the aim

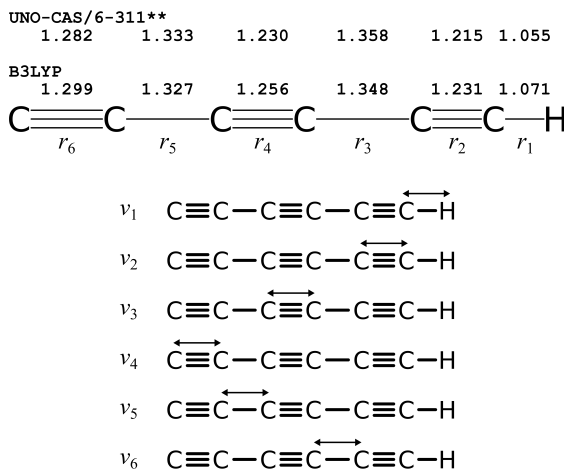


Figure 4.17: The geometry of the C_6H molecule, adopted from the UNO-CAS/6-311** calculations of Liu et al. (1992) and from the more recent B3LYP calculations by Brown et al. (1999). Bond lengths (in Å) are exaggerated to emphasize their differences. Also shown are the six fundamental nondegenerate eigenmodes where double arrows indicate on which bond the stretching vibration primarily occurs.

to assign the observed bands to the vibronic level structure of the $B^2\Pi$ state.

4.4.1 $^2\Pi$ levels

In all cases the bands connected to $^2\Pi - ^2\Pi$ character display the characteristic spin-orbit splitting with $A'' \approx -15 \text{ cm}^{-1}$ for the C_6H and C_6D isotopologues, hence yielding an inverted spin-orbit level ordering between $^2\Pi_{3/2}$ and $^2\Pi_{1/2}$. As discussed previously, (Bacalla et al. 2015) the ground state spin-orbit splitting for $^{13}C_6H$ is $A'' \approx -12 \text{ cm}^{-1}$. In all the fits and band contour simulations the ground state spin-orbit constants have been kept fixed at these values. The spin-orbit structure of the $B^2\Pi - X^2\Pi$ (0,0) origin bands of C_6H and C_6D was discussed in an earlier study (Linartzt et al. 1999) and yielded an excited state spin-orbit constant of $A' \approx -24 \text{ cm}^{-1}$. The value for $^{13}C_6H$ of $A' \approx -21 \text{ cm}^{-1}$ can be considered consistent (Bacalla et al. 2015).

The spectra of the $^2\Pi - ^2\Pi$ bands are compared with observations from matrix-isolation data, which bear the advantage that a mass-analyzer stage selects the ionized radical species before depositing in a matrix. In this way the matrix data provide an additional constraint that can be used to identify the carriers of the bands discussed

here. For C_6H such studies were typically performed in neon matrices cooled to 5 K, where only the $^2\Pi$ ground state was populated (Forney et al. 1995, Freivogel et al. 1995). In these matrix studies, no excitations associated with the Renner-Teller ν_{11} bending mode were observed, thus creating another helpful selection criterion. Furthermore, several band features, observed in the matrix spectra, were assigned to vibrational modes in the electronically excited C_6H molecule, from a comparison with calculated fundamental frequencies for the electronic ground state of the molecule as available at the time (Liu et al. 1992, Brown et al. 1999). Besides the 0_0^0 origin band of the $\text{B}^2\Pi\text{--X}^2\Pi$ system, three additional nondegenerate modes were observed at vibrational excitation energies of 2080.8 cm^{-1} , 1637.4 cm^{-1} , and 658.9 cm^{-1} . These stretching vibrations generate a $^2\Pi\text{--}^2\Pi$ type transition as is clearly observed in the spectra. Of importance for the present analysis is that the matrix shift for the 0_0^0 origin band amounts to -136 cm^{-1} . A typical finding from matrix-isolation spectroscopy is that matrix shifts tend to be constants for vibronic structures within a few cm^{-1} . This forms another ingredient for identifying bands.

The spectra of Bands XV and XVI, for which both $^2\Pi_{3/2}\text{--}^2\Pi_{3/2}$ and $^2\Pi_{1/2}\text{--}^2\Pi_{1/2}$ components were observed for C_6H , can be unambiguously assigned to a $^2\Pi\text{--}^2\Pi$ doublet for a number of reasons, even though the spectrum is heavily contaminated. This band was observed in a matrix study (Freivogel et al. 1995) exhibiting a matrix shift of -137 cm^{-1} with respect to the present measurement as well as to the shift observed in a lower resolution gas-phase discharge spectrum (Kotterer & Maier 1997). The present study yields an excited state spin-orbit constant of $A' = -24.4\text{ cm}^{-1}$, which is consistent with that of the origin band. We follow the assignment as in previous studies to match the two components of this band to the lowest non-degenerate vibration, the ν_6 mode, which derives its energy from the vibrational motion of a C–C single bond in the molecule (cf. Fig. 4.17). It is noted, however, that the intensity ratio between the $^2\Pi_{3/2}\text{--}^2\Pi_{3/2}$ and the $^2\Pi_{1/2}\text{--}^2\Pi_{1/2}$ spin-orbit components behaves somewhat irregularly (see the Results section for Bands XV and XVI).

In a similar way, the bands observed for C_6H in the higher energy region (Bands XVIII and XIX) can be well reproduced by a $^2\Pi\text{--}^2\Pi$ doublet with excited state spin-orbit values of $A' = -20.3\text{ cm}^{-1}$ and $A' = -16.8\text{ cm}^{-1}$, which are in good agreement with the A' spin-orbit constant for the vibrationless origin band. Comparison of the present gas-phase band origins with matrix data yields matrix shifts ~ 133 and $\sim 142\text{ cm}^{-1}$, in good agreement with the typical matrix shift as measured for the 0_0^0 origin band. In previous matrix isolation studies (Forney et al. 1995, Freivogel et al. 1995) these bands were assigned to ν_5 and ν_3 modes from a comparison with the then available *ab initio* data (Liu et al. 1992). In the later calculations (Brown et al. 1999, Cao & Peyerimhoff 2001) the ν_3 mode is shifted to lower frequencies, which is indeed in agreement with the present observation of $\Delta\nu = 2080.8\text{ cm}^{-1}$. For the assignment of the band observed at $\Delta\nu = 1637.4\text{ cm}^{-1}$, the situation is less clear. In view of the most recent calculations this band matches better with the ν_4 mode than with the earlier identification as ν_5 (Freivogel et al. 1995). Hence we keep this assignment as

tentative at ν_4 .

The observed spectra (see Fig. 4.16), recorded for the first time in the gas phase, are markedly different from all other bands measured, in the sense that in all other cases resolved rotational lines appear. The ν_3 and ν_4 excited state vibrational modes exhibit a triple-bond stretching vibration (cf. Fig. 4.17), which means that the molecule does not deviate from linearity. Hence, a rotational line separation is expected to be very similar to that of other ${}^2\Pi - {}^2\Pi$ bands and rotational lines should be resolved in the same manner as for the other bands detected. Because this is not observed, it is assumed that the ν_3 and the ν_4 modes undergo lifetime broadening, most likely due to internal conversion. It is noted that the next carbon chain molecule in the $C_{2n}H$ series, C_8H , also exhibits lifetime broadening already in its origin band (Birza et al. 2003). For the moment, we leave the latter issues as outside the scope of the present work. Fluorescence studies, similarly as performed for the C_4H molecule (Hoshina et al. 1998), might clarify some of the dynamics.

Because the stretching vibrations (which give rise to a state of total ${}^2\Pi$ symmetry) are all predicted upward from $\sim 640\text{ cm}^{-1}$, this leaves little space for assigning the other low frequency modes of total ${}^2\Pi$ symmetry. What remains to be considered are the following bands: Bands VII through XI and Bands XIII and XIV, whereas Band XVII is a special case, because its frequency is larger than the 650 cm^{-1} demarcation point between stretching and bending modes in C_6H .

Bands IX and X, detected for C_6H only, reproduce the characteristic structure of a ${}^2\Pi_\Omega - X^2\Pi_\Omega$ doublet. The derived value of $A' = -23.77\text{ cm}^{-1}$ corresponds to the typical value for the spin-orbit constant also found for the 0_0^0 origin band and the ν_6 mode (Bands XV and XVI). In the neon-matrix spectra (Freivogel et al. 1995) this band was observed at $19\,286\text{ cm}^{-1}$. The presently observed gas-phase $B^2\Pi_\Omega - X^2\Pi_\Omega$ doublet is thus shifted by 143 cm^{-1} , consistent with the typical gas-matrix shift for C_6H . This mode has an excitation energy of 439.5 cm^{-1} .

Bands XIII and XIV again display the typical characteristics of a ${}^2\Pi - {}^2\Pi$ doublet, but this assignment yields an excited state spin-orbit constant of $A' = -8.0\text{ cm}^{-1}$, which is atypical for the $B^2\Pi$ state. The vibrational mode has an excitation energy of 603 cm^{-1} above the band origin.

Band VIII, observed for both C_6H and $^{13}C_6H$, and Band XI observed only for C_6H , both display a characteristic of a ${}^2\Pi_{3/2} - {}^2\Pi_{3/2}$ component. In view of the fact that rotational fits could be made for the C_6H spectra, resulting in a rotational constant matching that of C_6H , the assignment of Bands VIII and XI to the C_6H molecule can be considered as unambiguous. Band VIII has, in C_6H , an excitation energy of 337 cm^{-1} above the origin, whereas in $^{13}C_6H$ it is at 324 cm^{-1} , consistent with the pattern of isotope shifts for the vibrational bands.

Band VII, observed for all three isotopologues, involves a ${}^2\Pi_{3/2} - {}^2\Pi_{3/2}$ component. The hypothesis that this component is overlaid with a ${}^2\Pi_{1/2} - {}^2\Pi_{1/2}$ component yields an upper state spin-orbit constant of $A' = -14.6\text{ cm}^{-1}$. This interpretation should however be considered as tentative. In any case, the assignment of the

$^2\Pi_{3/2} - ^2\Pi_{3/2}$ component may be considered as firm, as is the assignment of these bands to the C_6H molecule. Band VII lies at an excitation energy of 309 cm^{-1} for C_6H , and at 296 cm^{-1} for $^{13}C_6H$, again consistent with the isotopic pattern.

As for the vibrational levels of these bands, the modes with frequencies 308.8 cm^{-1} , 336.7 cm^{-1} , 439.5 cm^{-1} , and 603.3 cm^{-1} , hence below $\sim 650\text{ cm}^{-1}$, cannot be assigned to nondegenerate eigenmodes. There simply are no stretching modes of such low energies predicted in the *ab initio* calculations (Doyle et al. 1991, Liu et al. 1992, Brown et al. 1999, Cao & Peyerimhoff 2001) (see Table 4.1). Hence, the entire set of low-lying $^2\Pi$ states must be due to combination modes of bending vibrations, such as $2\nu_{11}$, $\nu_{11} + \nu_{10}$, $2\nu_{10}$, etc.

The observed spectrum of Band XVII is weak and only a band contour simulation has been possible. Its excitation energy of 937 cm^{-1} does not match with a stretching eigenmode in the *ab initio* calculations. The ν_5 stretching mode yields a consistent value close to $\sim 1210\text{ cm}^{-1}$ in the *ab initio* calculations (cf. Table 4.1), which is off by $\sim 300\text{ cm}^{-1}$ with respect to the band origin of Band XVII. If ν_5 is not covered by the band observed at 1637.4 cm^{-1} (see above) then it might tentatively be assigned to the excitation at 937 cm^{-1} . Improved calculations of the $B^2\Pi$ excited electronic state vibrations of C_6H might decide on such a tentative assignment. Alternatively, and more probably, this feature could be due to a combination band, e.g., to a $2\nu_9$ mode. The observation that the B' rotational constants of several of these vibronic modes are larger than that of the 0_0^0 origin band implies that the vibration-rotation interaction is negative. This is typical for bending or bending-like modes, as was shown in the example of vibrations in the ground state of HC_6H (Chang et al. 2016). This lends further credit to assigning the low-lying $^2\Pi$ states to bending combination modes.

4.4.2 $^2\Sigma$ levels

To assign the remaining features in the recorded spectra interpreted as $^2\Sigma - ^2\Sigma$ type bands, the interaction between degenerate electronic states and its fundamental bending modes, i.e., the Renner-Teller effect, has to be analyzed for a number of vibronically excited states of $^2\Sigma$ symmetry. In two sets of *ab initio* calculations performed for the electronic ground state (Brown et al. 1999, Cao & Peyerimhoff 2001), some 5 doubly degenerate bending modes were calculated using B3LYP hybrid functionals (Brown et al. 1999): ν_{11} at $110\text{--}120\text{ cm}^{-1}$, ν_{10} at $214\text{--}255\text{ cm}^{-1}$, ν_9 at $396\text{--}445\text{ cm}^{-1}$, ν_8 at $519\text{--}553\text{ cm}^{-1}$, and ν_7 at $561\text{--}679\text{ cm}^{-1}$. Each of these give rise to a $\mu^2\Sigma - \kappa^2\Sigma$ doublet on the basis of which the five observed $^2\Sigma - ^2\Sigma$ transitions are to be assigned.

The Hamiltonian describing the energy of vibronic states is given as the sum of the energies involved in pure vibration, in the RT coupling, and in the spin-orbit (SO) interaction:

$$H = H_{\text{vib}} + H_{\text{RT}} + H_{\text{SO}}.$$

With the measured band origin T_0 for a particular transition, diagonalization of a matrix for calculated matrix elements for the various contributions will yield values of

the true spin-orbit coupling constant ($A''_{SO} = -47.5 \text{ cm}^{-1}$ and $A'_{SO} = -23.74 \text{ cm}^{-1}$) as well as for the Renner-Teller parameter ϵ , derived typically in the product $\epsilon\omega$ (Zhao et al. 2011a), with ω as the vibrational frequency. Then for $^2\Sigma$ vibronic states, the effective splitting A_Σ between the two $^2\Sigma$ components (labeled as $\mu^2\Sigma$ and $\kappa^2\Sigma$) is given by:

$$A_\Sigma = \sqrt{A_{SO}^2 + 4\epsilon^2\omega^2} \quad (4.1)$$

and the effective rotational constants can be approximated as: (Hougen 1962, Herzberg 1966)

$$B_{\text{eff}}^{\mu/\kappa} = B \left(1 \pm \frac{A_{SO}^2 B}{A_\Sigma^3} \right) \quad (4.2)$$

$$\gamma_{\text{eff}}^{\mu/\kappa} = 2B \left(1 - \frac{2\epsilon\omega}{A_\Sigma} \pm \frac{A_{SO}^2 B}{A_\Sigma^3} \right). \quad (4.3)$$

Such a RT analysis can be performed for the two low-lying bending modes ν_{10} and ν_{11} . For the lowest $\nu_{11} = 1$ vibrational mode, this was previously done for the C_6H and C_6D molecule, forming the basis for an assignment of a $\{11\}_1^1 \mu^2\Sigma - \mu^2\Sigma$ transition (Zhao et al. 2011a). A large RT parameter was obtained for the ground state ($\epsilon''_{11} \sim 0.99$), whereas a much smaller value was found for the excited state ($\epsilon'_{11} \sim 0.09$).

The presently observed Band III of $^{13}C_6H$ can be assigned in an analogous manner. On the basis of isotopic regularity, no other band feature is observed between this band and the (0,0) origin band of $^2\Pi - ^2\Pi$ signature (combined Bands I and II). As listed in Table 4.2, the isotopic shifts of the first three observed bands of $^{13}C_6H$ are decreasing; Band III is consistent with this trend, having a band shift of 0.1 cm^{-1} to higher energy compared to the regular isotopologue C_6H . In addition, its band contour appears very similar to those in the other isotopologues. Together with the results of the rotational line fit, all of these support for an unambiguous assignment of Band III in $^{13}C_6H$.

Furthermore, the RT analysis for the $\nu_{11} = 1$ mode in the upper electronic state predicts energy levels in the form of $^2\Sigma$ and $^2\Delta$ pairs, with a $\{11\}_1^1 \kappa^2\Sigma$ level lying $\sim 30 \text{ cm}^{-1}$ above the $\{11\}_1^1 \mu^2\Sigma$ level. No bands with nearly similar features have been observed in the predicted energy range for any of the three isotopologues. In general, a stronger RT effect in the upper state weakens the $\kappa^2\Sigma - \mu^2\Sigma$ transition which indicates a lesser coupling intensity between vibrational and electronic orbital angular momenta. In the case of a strong Renner-Teller effect, the Π electronic orbital is coupled to a vibrational angular momentum (of Π symmetry), resulting in two Σ and one Δ vibronic states, where the two Σ states have different parity signs ($^2\Sigma^+$

and $^2\Sigma^-$). The transition to a pure $^2\Sigma^-$ state, from the $\mu^2\Sigma^+$ ground state becomes forbidden (Hougen 1962, Herzberg 1966). Apparently, the value of ϵ'_{11} is large enough to prohibit an observable intensity in the $\kappa^2\Sigma$ component, and indeed no band with a substantial S/N is found at the expected position for any of the three isotopologues. Transitions to the $^2\Delta_{5/2}$ and $^2\Delta_{3/2}$ also cannot be observed since the only populated vibronic component of the ground $\nu_{11} = 1$ vibrational mode is the $\{11\}_1 \mu^2\Sigma$ state and the selection rule does not allow for a change in vibronic symmetry greater than by one quantum number.

For the low-lying $\nu_{10} = 1$ bending mode in the $B^2\Pi$ excited state, a similar RT analysis can be performed yielding a μ - κ doublet of $^2\Sigma$ symmetry. Experimentally, from the characteristic shapes of Bands IV and V, one can infer that they start from the same ground state, and that they are excited to coupled vibronic levels. Indeed, from the rotational fit, both of these bands can be simulated using the same ground state constants which are those of the $\{11\}_1 \mu^2\Sigma$ state. Moreover, the B' rotational constants for both bands are rather similar, as expected for a RT doublet.

The observed difference between the two band origins ($\sim 23 \text{ cm}^{-1}$) corresponds to the splitting A_{Σ}^{obs} between the $\mu^2\Sigma$ and the $\kappa^2\Sigma$ doublet. In contrast to the case of the ν_{11} bending mode, the combination of Bands IV and V may be interpreted as a doublet of transitions to the $\{10\}_1^1 \mu^2\Sigma$ lower and $\{10\}_1^1 \kappa^2\Sigma$ upper states of the RT doublet. If the value of the true spin-orbit constant $A'_{\text{SO}} = -23.74 \text{ cm}^{-1}$, as determined from the analysis of ν_{11} , is adopted, then an effective splitting between the band origins is calculated at $|A_{\Sigma}^{\text{calc}}| > |A_{\Sigma}^{\text{obs}}|$, via eq. (4.1). This hints to a very small Renner-Teller parameter ($\epsilon'_{10} < 0.01$) but still, the splitting between band origins for $\{10\}_1^1 \kappa^2\Sigma$ and $\{10\}_1^1 \mu^2\Sigma$ is too small for a consistent analysis. It is likely that the $\{10\}_1^1 \kappa^2\Sigma$ component (Band V) is shifted downward, for example, due to a perturbation or a Fermi resonance. The fact that the γ' parameter for Band V, specifically for the C_6H isotopologue ($\gamma' = 0.107 \text{ cm}^{-1}$), corresponds to $\gamma' > 2B'$ makes it unphysical and also points at a perturbation. In any case, the ϵ'_{10} value is expected to be small because both RT components are observed in the spectrum for all three isotopologues.

The next band observed, Band VI, also exhibits the character of a $^2\Sigma - ^2\Sigma$ transition. Here, as in the case of the lowest ν_{11} , no second component in a μ - κ RT pair is observed. In view of the numbering of bending vibrations, Band VI may be assigned as the lower μ component of ν_9 . In principle, the next band of $^2\Sigma - ^2\Sigma$ character (Band XII) might be considered as the upper κ component of ν_9 . However, the B' rotational constants for these bands differ substantially whereas they should be similar in a RT pair. For this reason, the last $^2\Sigma - ^2\Sigma$ transition (Band XII) is tentatively assigned as the μ component of ν_8 .

4.4.3 Isotope shifts

Table 4.2 displays values for the isotope shifts for the bands observed for $^{13}\text{C}_6\text{H}$ and C_6D with respect to those of C_6H . It should be noted that isotope shifts are deter-

mined only for degenerate bending modes, that is, for the $^2\Sigma - ^2\Sigma$ vibronic bands or for combinations thereof. The values can be understood by assuming that the effect of zero-point vibration makes up for a decisive contribution. If the ground state potential hypersurface is considered to be deeper than for the excited state, i.e., stronger chemical binding in the ground state, this explains the blue shift of the origin bands for the heavier molecules. The effect appears to be much stronger for C_6D than for $^{13}C_6H$ in view of the larger mass difference between D and H. For gradually higher vibrational excitation a regular effect of redshift for higher modes is observed to be $\sim 10\text{ cm}^{-1}$ overall for eigenmodes up to $\sim 300\text{ cm}^{-1}$. Although for $^{13}C_6H$ the shift pattern develops smoothly and linearly, for C_6D the pattern is less regular. There is an outlier for Band V, which may be associated with the perturbation found in the Renner-Teller splitting of Bands IV and V. A perturbation-induced down shifting of Band V in C_6H will result in an increased isotope shift for C_6D and a decreased isotope shift for $^{13}C_6H$ (cf. Fig. 4.1). Indeed, the isotope shift of Band V for $^{13}C_6H$ deviates somewhat ($\sim 2\text{ cm}^{-1}$) from a smooth regular progression of isotope shifts.

The measured isotope shifts in the present study all pertain, except for the origin band, to degenerate vibrational modes or combinations thereof. It is found that isotopic shifts for these bands in $^{13}C_6H$ and C_6D behave very differently, whereas in C_6D the isotope shift is $\sim 50\text{ cm}^{-1}$; for $^{13}C_6H$ this is typically $\sim -5\text{ cm}^{-1}$, hence of opposite sign. Brown et al. (1999) have performed specific isotope shift calculations for the nondegenerate ν_2 vibrational mode (reassigned from ν_3 in their paper) yielding a similar value of 78 cm^{-1} for both isotope shifts of $^{13}C_6H$ and C_6D (with respect to C_6H). This finding seems difficult to reconcile with the present measurements. Refined isotope shift calculations for a variety of bands may settle this issue.

4.5 Conclusion

The present study reports a comprehensive investigation of the vibronic structure of the $B^2\Pi - X^2\Pi$ transition in the C_6H molecule in the gas phase. Some 19 bands or band components have been detected, and in most cases rotationally resolved, for the main C_6H isotopologue, whereas eight have been duplicated for $^{13}C_6H$ and seven for C_6D . All assignments, taking into account all the arguments given here, result in a rather complete energy level diagram for C_6H (Fig. 4.18) in which the observed transitions (with corresponding band labeling) are shown. This figure includes energies pertaining to the C_6H main isotopologue; corresponding values for $^{13}C_6H$ and C_6D can be obtained from Table 4.2. For the non-degenerate (Σ) vibrations, besides the 0_0^0 origin band three vibrational eigenmodes have been identified: ν_6 , ν_3 , and, tentatively, ν_4 . In addition, a number of excited $^2\Pi$ vibronic states have been assigned to be probed in combination bands involving two low-lying degenerate vibrations. Low-lying bending modes have been observed for which a Renner-Teller treatment has been applied unambiguously, leading to the assignment of the $\mu^2\Sigma$ component of the ν_{11} mode and both $\mu^2\Sigma$ and $\kappa^2\Sigma$ components of the ν_{10} mode, whereas the $\mu^2\Sigma$

components of ν_9 and ν_8 have been tentatively assigned. These assignments are based on *ab initio* calculations of the C_6H molecule, which were, however, carried out for the ground state electronic configuration of the molecule (Liu et al. 1992, Brown et al. 1999, Cao & Peyerimhoff 2001). Previous matrix isolation data (Forney et al. 1995, Freivogel et al. 1995) and higher temperature discharge spectra (Kotterer & Maier 1997) were useful in the analysis, as were the present results on the $^{13}\text{C}_6\text{H}$ and C_6D isotopologues. The analysis and descriptive detail of the level structure of C_6H now equals that of the C_4H molecule (Hoshina et al. 1998) which is part of the same C_nH carbon chain series.

The present comprehensive experimental study might be a stimulus for future *ab initio* calculations specifically focusing on the $\text{B}^2\Pi$ electronically excited state of C_6H . Some open issues remain; those are the quest for a definite assignment of some vibrational (combination) modes, perturbation effects, and the dynamical effect of internal conversion in the highest vibrational levels. The investigation of the optical spectra of carbon chain molecules, and in particular also the C_6H molecule, was originally driven by the hypothesis that $^2\Pi - ^2\Pi$ electronic transitions of C_nH radicals might be responsible for some of the diffuse interstellar bands (Fulara et al. 1993b) observed in the optical spectra of reddened stars. For the presently observed manifold of vibronic bands, this is not the case.

Acknowledgment

This work has been supported by the Netherlands Organization for Scientific Research (NWO) through a VICI grant and was performed within the context of the Dutch Astrochemistry Network (DAN).

Table 4.2: Summary of spectroscopic constants in cm^{-1} .^a

	T_0^b	Band type	B'	B''	γ' (10^{-3})
C_6H					
I, II ^c	18989.7672(4)	$^2\Pi - ^2\Pi$	0.0455952(5)	<i>0.04640497</i>	-3.63(18)
III ^c	19066.8372(6)	$^2\Sigma - ^2\Sigma$	0.0456873(11)	<i>0.04652018</i>	38.29(6)
IV	19197.314(3)	$^2\Sigma - ^2\Sigma$	0.045580(7)	<i>0.04652018</i>	79.55(18)
V	19220.294(6)	$^2\Sigma - ^2\Sigma$	0.045971(18)	<i>0.04652018</i>	107.1(4)
VI	19283.992(3)	$^2\Sigma - ^2\Sigma$	0.045916(8)	<i>0.04652018</i>	70.27(16)
VII	19298.56 ^f	$^2\Pi - ^2\Pi$	0.0457 ^f	<i>0.04640497</i>	40 ^f
VIII	19326.479(4)	$^2\Pi - ^2\Pi$	0.045392(11)	<i>0.04640497</i>	...
IX, X	19429.236(5)	$^2\Pi - ^2\Pi$	0.046137(12)	<i>0.04640497</i>	-7(6)
XI	19451.792(2)	$^2\Pi - ^2\Pi$	0.045969(5)	<i>0.04640497</i>	...
XII	19486.08 ^f	$^2\Sigma - ^2\Sigma$	0.0455 ^f	<i>0.04652018</i>	13 ^f
XIII, XIV	19593.11 ^f	$^2\Pi - ^2\Pi$	0.0456 ^f	<i>0.04640497</i>	...
XV, XVI	19648.7 ^f	$^2\Pi - ^2\Pi$	0.0460 ^f	<i>0.04640497</i>	...
XVII	19926.41 ^f	$^2\Pi - ^2\Pi$	0.0460 ^f	<i>0.04640497</i>	...
XVIII	20627.2 ^f	$^2\Pi - ^2\Pi$	0.0461 ^f	<i>0.04640497</i>	-40 ^f
XIX	21070.6 ^f	$^2\Pi - ^2\Pi$	0.0454 ^f	<i>0.04640497</i>	30 ^f
$^{13}C_6H$					
I, II ^h	18992.116(1)	$^2\Pi - ^2\Pi$	0.042218(17)	0.042973(16)	...
III	19066.9716(16)	$^2\Sigma - ^2\Sigma$	0.04227(4)	0.04308(4)	34(3)
IV	19192.1414(17)	$^2\Sigma - ^2\Sigma$	0.042235(3)	<i>0.04308</i>	69.72(11)
V	19215.202(2)	$^2\Sigma - ^2\Sigma$	0.042443(5)	<i>0.04308</i>	90.22(15)
VI	19274.22 ^f	$^2\Sigma - ^2\Sigma$	0.0422 ^f	<i>0.04308</i>	-4 ^f
VII	19288.62 ^f	$^2\Pi - ^2\Pi$	0.0423 ^f	<i>0.04297</i>	...
VIII	19316.45 ^f	$^2\Pi - ^2\Pi$	0.0425 ^f	<i>0.04297</i>	...
C_6D					
I, II ^c	19041.2564(5)	$^2\Pi - ^2\Pi$	0.043592(4)	<i>0.04429243</i>	-6.3(7)
III ^c	19115.5251(10)	$^2\Sigma - ^2\Sigma$	0.0436478(19)	<i>0.0443852</i>	39.68(10)
IV	19243.221(2)	$^2\Sigma - ^2\Sigma$	0.043638(5)	<i>0.0443852</i>	57.89(11)
V	19271.454(5)	$^2\Sigma - ^2\Sigma$	0.043721(11)	<i>0.0443852</i>	64.6(3)
VI	19327.10 ^f	$^2\Sigma - ^2\Sigma$	0.0429 ^f	<i>0.0443852</i>	-1 ^f
VII	19342.16 ^f	$^2\Pi - ^2\Pi$	0.0435 ^f	<i>0.04429243</i>	...

Note: Except for Bands I and II and for Band III, we assume $D' \approx D''$: $1.35 \times 10^{-9} \text{ cm}^{-1}$ (C_6H) and $1.2 \times 10^{-9} \text{ cm}^{-1}$ ($^{13}C_6H$ and C_6D). ^a Terminating the values (enclosed in parentheses) are the statistical uncertainties (1σ) obtained from a least-squares rotational line fit. For values obtained through a band contour simulation, the uncertainties are omitted. Numbers in italics are electronic ground state values taken from Linnartz et al. (1999) and Gottlieb et al. (2010) and are kept fixed in the fitting routine (with the exception for $^{13}C_6H$). Tentative mode assignments are enclosed in square brackets [].

Table 4.2: *continued.*

	γ'' (10^{-3})	A'	A''	Relative energy	Isotopic shift ^c	Assignment ^d
C₆H						
I, II ^e	-7.12	-23.69(2)	-15.04	0.0	...	0 ₀ ⁰
III ^e	-0.628	77.1	...	$\mu\{11\}_1^1$ bend
IV	-0.628	207.5	...	$\mu\{10\}_1^1 \mu\{11\}_1$ bend
V	-0.628	230.5	...	$\kappa\{10\}_1^1 \mu\{11\}_1$ bend
VI	-0.628	294.2	...	$[\mu\{9\}_1^1 \mu\{11\}_1]$ bend
VII	-7.12	-14.6 ^{f,g}	-15.04	308.8	...	
VIII	336.7	...	
IX, X	-7.12	-23.77(2)	-15.04	439.5	...	
XI	462.0	...	
XII	-0.628	496.3	...	$[\mu\{8\}_1^1 \mu\{11\}_1]$ bend
XIII, XIV	...	-8.0 ^f	-15.04	603.3	...	
XV, XVI	...	-24.4 ^f	-15.04	658.9	...	$\{6\}_0^1$ stretch
XVII	...	-14.50 ^f	-15.04	936.6	...	
XVIII	-7.12	-20.3 ^f	-15.04	1637.4	...	$[\{4\}_0^1]$ stretch
XIX	-7.12	-16.8 ^f	-15.04	2080.8	...	$\{3\}_0^1$ stretch
¹³C₆H						
I, II ^h	...	-20.78(13)	-11.62(13)	0.0	2.3	0 ₀ ⁰
III	-4(3)	74.9	0.1	$\mu\{11\}_1^1$ bend
IV	-4	200.0	-5.2	$\mu\{10\}_1^1 \mu\{11\}_1$ bend
V	-4	223.1	-5.1	$\kappa\{10\}_1^1 \mu\{11\}_1$ bend
VI	-4	282.1	-9.8	$[\mu\{9\}_1^1 \mu\{11\}_1]$ bend
VII	...	-11.40 ^{f,g}	-11.62	296.5	-9.9	
VIII	324.3	-10.0	
C₆D						
I, II ^e	-3.85	-24.07(2)	-15.13	0.0	51.5	0 ₀ ⁰
III ^e	-0.631	74.3	48.7	$\mu\{11\}_1^1$ bend
IV	-0.631	202.0	45.9	$\mu\{10\}_1^1 \mu\{11\}_1$ bend
V	-0.631	230.2	51.2	$\kappa\{10\}_1^1 \mu\{11\}_1$ bend
VI	-0.631	285.8	43.1	$[\mu\{9\}_1^1 \mu\{11\}_1]$ bend
VII	...	-14.68 ^{f,g}	-15.13	300.9	43.6	

^b Resulting values from the fitting routine, but the absolute uncertainty is limited to 0.02 cm⁻¹ from I₂ calibration. ^c Relative to the corresponding band in C₆H. ^d The notation, e.g. $\kappa\{10\}_1^1 \mu\{11\}_1$, denotes a transition from the μ component of the $\nu_{11} = 1$ vibrational mode of the lower electronic state to the κ component of the $\nu_{10} = 1$ mode of the upper electronic state. The mode numbering is adopted from [Brown et al. \(1999\)](#). ^e Data from [Zhao et al. \(2011a\)](#). ^f Value obtained from band contour simulation. ^g Tentative value, derived from the assumption that the $^2\Pi_{1/2}$ component overlaps the $^2\Pi_{3/2}$ component. ^h Data from [Bacalla et al. \(2015\)](#).

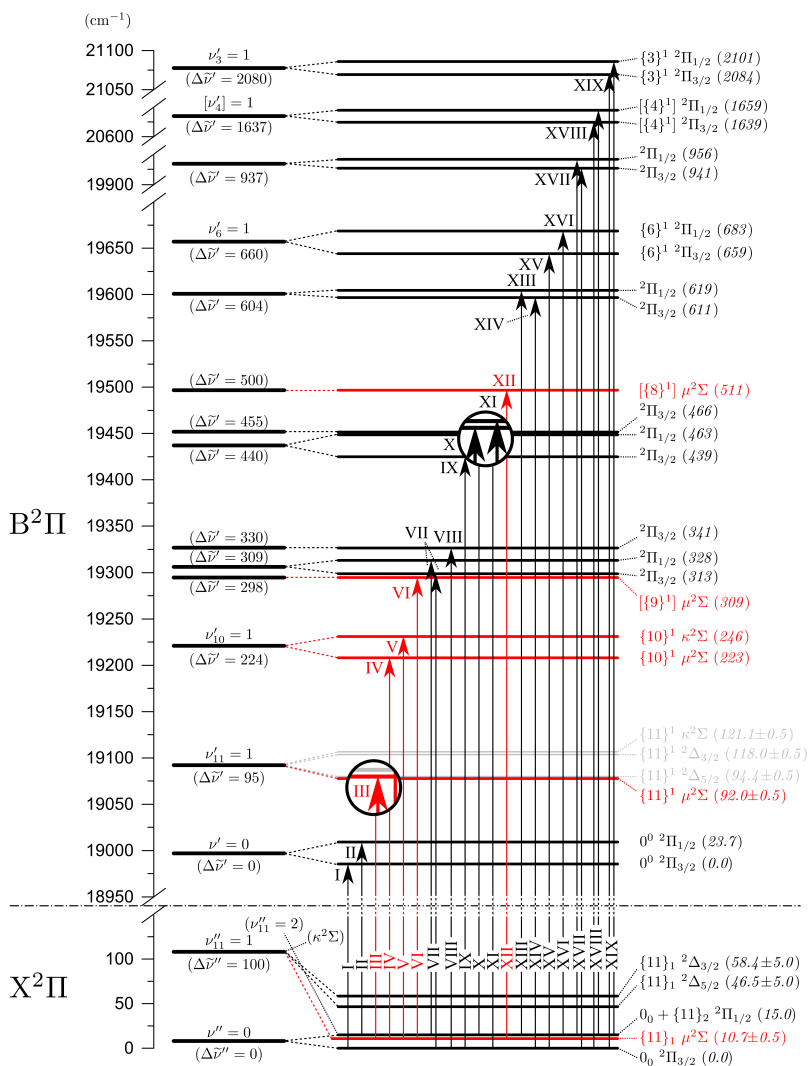


Figure 4.18: Energy level diagram for C_6H . The line cutting across the diagram separates the ground $X^2\Pi$ electronic state from the excited $B^2\Pi$ state. As plasma jets produce vibrationally cold molecules, all observed transitions originate from the lowest lying states: $0_0 \ ^2\Pi_{3/2}$, $0_0 \ ^2\Pi_{1/2}$, and $\{11\}_1 \ \mu^2\Sigma$, with the $^2\Sigma - ^2\Sigma$ transitions in red. Numbers in parentheses () are the vibrational (left) and vibronic (right) frequencies expressed relative to the respective vibrational and vibronic ground states for each of the electronic states. States that are thus far unobserved experimentally are indicated in gray. Tentative mode identifications are given in square brackets []. Vibrational eigenmodes are according to the numbering by Brown et al. (1999).

CHAPTER 5

Cosmic ray ionization rates in diffuse clouds from near-UV observations of interstellar OH⁺

We report cosmic ray ionization rates toward ten reddened stars studied within the framework of the EDIBLES (ESO diffuse interstellar bands large exploration survey) program, using the VLT-UVES. For each sightline, between two and ten individual rotational lines of OH⁺ have been detected in its (0,0) and (1,0) $A^3\Pi - X^3\Sigma^-$ electronic band system. This allows constraining of OH⁺ column densities toward different objects. Results are also presented for 28 additional sightlines for which only one or rather weak signals are found. An analysis of these data makes it possible to derive the primary cosmic ray ionization rate ζ_p in the targeted diffuse interstellar clouds. For the ten selected targets, we obtain a range of values for ζ_p equal to $(3.9 - 16.4) \times 10^{-16} \text{ s}^{-1}$. These values are higher than the numbers derived in previous detections of interstellar OH⁺ in the far-infrared / submillimeter-wave regions and in other near-ultraviolet studies. This difference is a result of using new OH⁺ oscillator strength values and a more complete picture of all relevant OH⁺ formation and destruction routes (including the effect of proton recombinations on PAHs), and the relatively high $N(\text{OH}^+)$ seen toward those ten targets.



This chapter is based on the work of Bacalla, X. L., Linnartz, H., Cox, N. L. J., Cami, J., Roueff, E., Smoker, J. V., Farhang, A., Bouwman, J., and Zhao, D. “The EDIBLES survey IV. Cosmic ray ionization rates in diffuse clouds from near-ultraviolet observations of interstellar OH⁺” in *Astron. Astrophys.* **622** (2019) A31.

5.1 Introduction

The hydroxyl cation, OH^+ , is an important reactive intermediate in the gas phase formation of water in the diffuse interstellar medium (ISM) (van Dishoeck et al. 2013), where ion-neutral molecule reactions are found to dominate (van Dishoeck & Black 1986, Le Petit et al. 2004). The formation mechanism of this ion involves the cosmic ray ionization of atomic or molecular hydrogen, followed by hydrogenation and oxygenation (Federman et al. 1996, Hollenbach et al. 2012). Thus, apart from playing a role in interstellar water chemistry, OH^+ can also be used as a probe of the primary¹ cosmic ray ionization rate ζ_p in these dilute regions of molecular gas (Hollenbach et al. 2012, Porras et al. 2014, Indriolo et al. 2015).

Rodebush & Wahl (1933) first observed spectral lines of the OH^+ molecule in the laboratory and the recorded transitions were subsequently assigned by Loomis & Brandt (1936) to the $A^3\Pi - X^3\Sigma^-$ electronic band system in the near-UV. de Almeida & Singh (1981) calculated the transition probabilities and oscillator strengths for these bands and suggested a number of wavelength positions where interstellar OH^+ is likely to manifest itself. de Almeida (1990) also provided values for the rotational hyperfine transitions in the fundamental electronic state at submillimeter wavelengths. In searching for the 909 GHz (0.33 mm) transition of OH^+ , Wyrowski et al. (2010) detected this ion for the first time in space using the Atacama Pathfinder EXperiment (APEX) telescope directed at Sagittarius B2(M). The 972 GHz (0.31 mm) transition was observed in a couple of bright continuum sources (in W31C by Gerin et al. 2010 and in W49N by Neufeld et al. 2010) through the Heterodyne Instrument for the Far-Infrared (HIFI) aboard the Herschel space observatory. Krełowski et al. (2010a) detected a weak line at 3583.769 Å in the spectra of a sample of interstellar sightlines obtained using the Ultraviolet and Visible Echelle Spectrometer (UVES) of the very large telescope (VLT) that is due to an isolated rotational transition in the $A^3\Pi - X^3\Sigma^-$ electronic origin band system of OH^+ . Porras et al. (2014) observed this same near-UV transition in a few other sightlines, and used it to estimate the value of ζ_p as was done in other work using submm transitions (e.g., by Hollenbach et al. 2012).

Recently, Zhao et al. (2015) detected (in four different sightlines) up to six of the near-UV OH^+ transitions initially provided by Merer et al. (1975), including two new (hitherto unidentified) interstellar features reported by Bhatt & Cami (2015) in the same year. The detection of more than one transition makes it possible to derive a better constrained value for the OH^+ column density than that based on the detection of one transition only. The Zhao et al. (2015) results showed good agreement with previous measurements of ζ_p that were based not only on detections of OH^+ , but also on detections of other cosmic ray ionization tracers in diffuse clouds like H_2O^+ , H_3O^+ , H_3^+ , and ArH^+ (Neufeld et al. 2010, Indriolo et al. 2012, 2015, Le Petit et al. 2004,

¹ The “primary” cosmic ray ionization rate ζ_p denotes the rate of ionization of atomic H that is solely caused by primary cosmic rays that have not interacted with the ISM to produce secondary particles.

Indriolo et al. 2007, Indriolo & McCall 2012, Neufeld & Wolfire 2017). More precise wavelengths and updated line oscillator strengths have also been provided recently through the updated spectral analyses and modeling efforts by Hodges & Bernath (2017) and by Hodges et al. (2018). All of these previous work, and with more OH⁺ lines now detected in the ISM, enable us to infer cosmic ray ionization rates in different sightlines where we have specifically chosen to characterize and know their physical properties as accurately as possible. With the vast spectral database and dedicated target characterization provided for by the ESO diffuse interstellar bands large exploration survey (EDIBLES) (Sec. 5.2), we report in this contribution detections of interstellar OH⁺ via ground-based near-UV observations as a complement to submm-wave observations such as with *Herschel* (e.g., Gerin et al. 2010, Neufeld et al. 2010) that require telluric-free conditions to record the pure rotational transitions of the OH⁺ molecule. Since the OH⁺ spectra are recorded as part of the diffuse interstellar bands (DIBs) survey, this work also holds much potential in providing insight into the nature of the DIBs, as relevant physical parameters such as the cosmic ray ionization rate – characterizing local conditions – are needed to help further constrain the carriers of these enigmatic absorption features (Herbig 1995, Cami & Cox 2014).

5.2 Observations and data processing

The data used in this work were recorded within the framework of EDIBLES, which is a large (250+ hr) filler program (ESO ID 194.C-0833, PI. N.L.J. Cox) using the VLT-UVES in Paranal, Chile. Details are available from Cox et al. (2017). To briefly summarize, in this survey four standard configurations of UVES (Dekker et al. 2000) are employed, with wavelength settings centered at 3460, 4370, 5640, and 8600 Å, covering from about 3042 to 10 420 Å, and with a spectral resolution of $\sim 70\,000$ in the blue (< 4800 Å). A total of 114 unique sightlines are targeted and, as of May 2018, around 80 percent have been observed. For our particular application, we use spectra from the 346-nm setting (3042–3872 Å) to look for and analyze the electronic transitions of OH⁺, as well as the 437-nm setting (3752–4988 Å) comprising the potassium (K I) doublet that is used for estimating total hydrogen column densities (Sect. 5.4.2) in the different sightlines. All spectra presented here have been processed using standard and custom data reduction protocols (wavelength calibration, flat fielding, echelle order merging, etc.; see Cox et al. 2017 for details) and quality control by the EDIBLES team.

We searched the 93 available EDIBLES sightlines for the spectroscopic signature of OH⁺, and clearly detected more than one transition in ten targets. These are listed in Table 5.1 together with their respective galactic coordinates, spectral type, visual extinction A_V , and reddening E_{B-V} . Where available, the column densities for both atomic hydrogen (H or H I) and molecular hydrogen (H₂) are also provided, as derived from measurements of L α and Lyman band absorptions, respectively (Diplas & Savage 1994, Jenkins 2009). Also listed are the calculated column density of the

Table 5.1: EDIBLES targets with measurable OH^+ absorption.

Identifier	Galactic Coordinates	Spectral type	A_V [mag.]	E_{B-V} [mag.]	$N(\text{H I})$ $\times 10^{21} [\text{cm}^{-2}]$	$N(\text{H}_2)$ $\times 10^{21} [\text{cm}^{-2}]$	$N(\text{H}_{\text{tot}})$ $\times 10^{21} [\text{cm}^{-2}]$	f_{H_2}
HD 37367	G179.0–01.0	B2 IV-V	1.49	0.37	1.5	0.34	2.2	0.31
HD 41117	G189.6–00.8	B2 Ia	1.25	0.41	2.5 ^a	0.49	3.5	0.28
HD 75860	G264.1+00.2	BC2 Iab	3.10	0.87
HD 79186	G267.3+02.2	B5 Ia	1.28	0.28	1.5	0.52	2.6	0.41
HD 80558	G273.0–01.4	B6 Ia	2.01	0.57
HD 114886	G305.5–00.8	O9 III+O9.5 III	0.84	0.28	2.2	0.17	2.5	0.13
HD 185418	G053.6–02.1	B0.5 V	1.27	0.42	1.6	0.51	2.6	0.39
HD 185859	G056.6–01.0	B0.5 Ia	1.64	0.56	1.7	...	≥ 1.7	...
HD 186745	G060.2–00.2	B8 Ia	2.98	0.88
HD 186841	G060.4–00.2	B0.5 I	3.01	0.95

Notes. The A_V -values are taken from Valencic et al. (2004) and Wegner (2003), while the E_{B-V} -values are calculated by Cox et al. (2017). $N(\text{H I})$ and $N(\text{H}_2)$ data are taken from Jenkins (2009) which are obtained through vacuum-UV absorption observations. The total hydrogen column density is calculated as $N(\text{H}_{\text{tot}}) = N(\text{H I}) + 2N(\text{H}_2)$ while the molecular hydrogen fraction is calculated as $f_{\text{H}_2} = 2N(\text{H}_2) / N(\text{H}_{\text{tot}})$.

^a Diplás & Savage (1994).

total hydrogen atoms $N(\text{H}_{\text{tot}})$ and the molecular hydrogen fraction f_{H_2} for each of the sightlines. Besides the ten selected targets with strongest detections, OH^+ was also seen along 28 other lines-of-sight. Here, signals were quite weak and typically limited to one transition. In principle, as will be shown, it is also possible to derive the cosmic ray ionization rate for these targets, but the resulting values are obviously much less accurate. (See Appendix A for an overview.)

5.3 OH^+ as a probe of the cosmic ray ionization rate

Cosmic rays are high-energy particles (mostly comprised of protons and helium nuclei) that originate from different astrophysical processes. They are ubiquitous across our galaxy and are one of the main drivers of ionization and chemistry in the ISM (Dalgarno 2006). One of the important chemical processes that is influenced by cosmic ray ionization is the gas-phase formation scheme of water, in which the OH^+ molecule acts as a reactive intermediate. The dominant reaction pathway leading to the formation of OH^+ in diffuse clouds is depicted in Fig. 5.1.

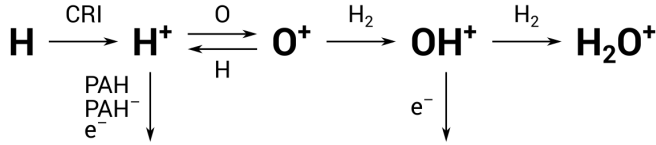


Figure 5.1: Ion-neutral chemistry of OH^+ through the atomic H reaction pathway (van Dishoeck & Black 1986, Hollenbach et al. 2012).

This reaction is initiated by the cosmic ray ionization (CRI) of atomic hydrogen, followed by charge exchange between H^+ and O — producing O^+ which then reacts with H_2 to form OH^+ . The H^+ , however, can also react with electrons and with neutral and negatively charged PAHs. Through this reaction scheme, we can derive the rate of ionization due to cosmic rays by quantifying the abundance of OH^+ in these diffuse molecular environments. In dense molecular clouds, another important OH^+ formation pathway is through the ionization of molecular hydrogen, but we neglect this contribution in our formulation since we assume here that the medium is very diffuse while OH^+ is forming (Hollenbach et al. 2012).

In order to establish a relation between CRI and OH^+ , we must account for all formation and destruction routes that lead to OH^+ , as well as for the intermediate species O^+ and H^+ . These reaction channels are listed in Table 5.2 with their respective reaction coefficients. With these, we build our formulation starting from three rate equations:

Table 5.2: Reaction channels and rate coefficients.

Reaction	Rate coefficient [cm ³ s ⁻¹]	
Charge-transfer:		
H ⁺ + O → O ⁺ + H	k ₁	4.0 × 10 ⁻¹⁰ exp(-227/T) ^a
O ⁺ + H → H ⁺ + O	k ₂	4.0 × 10 ⁻¹⁰ ^a
Ion-molecule reaction:		
O ⁺ + H ₂ → OH ⁺ + H	k ₃	1.7 × 10 ⁻⁹
OH ⁺ + H ₂ → H ₂ O ⁺ + H	k ₄	1.0 × 10 ⁻⁹
H ⁺ and PAH ⁽⁻⁾ recombination:		
H ⁺ + PAH → PAH ⁺ + H	α	7.0 × 10 ⁻⁸ Φ _{PAH}
H ⁺ + PAH ⁻ → PAH + H	α ⁻	8.1 × 10 ⁻⁷ Φ _{PAH} · (T/300) ^{-0.50}
Radiative recombination:		
H ⁺ + e ⁻ → H + hν	β _{H⁺}	3.5 × 10 ⁻¹² · (T/300) ^{-0.75}
Dissociative recombination:		
OH ⁺ + e ⁻ → O + H	β _{OH⁺}	3.8 × 10 ⁻⁸ · (T/300) ^{-0.50}
Cosmic ray ionization:		
H + CR → H ⁺ + e ⁻	ζ _H	≡ 1.5ζ _p [s ⁻¹] ^b

Notes. Rate coefficients are based on Hollenbach et al. (2012) and references therein.

^a Chabaud et al. (1980).

^b Glassgold & Langer (1974).

$$\begin{aligned}
 \frac{d \text{OH}^+}{dt} &= k_3[\text{O}^+][\text{H}_2] - k_4[\text{OH}^+][\text{H}_2] - \beta_{\text{OH}^+}[\text{OH}^+][\text{e}^-], \\
 \frac{d \text{O}^+}{dt} &= k_1[\text{H}^+][\text{O}] - k_2[\text{O}^+][\text{H}] - k_3[\text{O}^+][\text{H}_2], \text{ and} \\
 \frac{d \text{H}^+}{dt} &= \zeta_{\text{H}}[\text{H}] - \beta_{\text{H}^+}[\text{H}^+][\text{e}^-] - k_1[\text{H}^+][\text{O}] \\
 &\quad - \alpha[\text{PAH}][\text{H}^+] - \alpha^-[\text{PAH}^-][\text{H}^+],
 \end{aligned}$$

and assuming that the rate of change in the density of atomic H can be neglected as these reactions occur. Setting each one to zero (for the steady-state condition) and combining all the terms gives

$$[\text{OH}^+] = \frac{k_3[\text{H}_2]k_1[\text{O}]}{\{k_4[\text{H}_2] + \beta_{\text{OH}^+}[\text{e}^-]\} \{k_2[\text{H}] + k_3[\text{H}_2]\}} \times \frac{\zeta_{\text{H}}[\text{H}]}{\{\beta_{\text{H}^+}[\text{e}^-] + k_1[\text{O}] + \alpha[\text{PAH}] + \alpha^-[\text{PAH}^-]\}}.$$

This equation of densities can be further expressed in terms of the fractional abundance x of species X , with respect to the total number of hydrogen atoms per unit volume $n_{\text{H}_{\text{tot}}} (= [\text{H}] + 2[\text{H}_2]) [\text{cm}^{-3}]$, that is, $x(X) = [X]/n_{\text{H}_{\text{tot}}}$. This then results into

$$x(\text{OH}^+) = \frac{k_3 x(\text{H}_2) k_1 x(\text{O})}{\left\{ k_4 x(\text{H}_2) + \beta_{\text{OH}^+} x_{\text{e}^-} \right\} \left\{ k_2 x(\text{H}) + k_3 x(\text{H}_2) \right\}} \times \frac{1.5 \zeta_p x(\text{H})}{n_{\text{H}_{\text{tot}}} \left\{ \beta_{\text{H}^+} x_{\text{e}^-} + k_1 x(\text{O}) + \alpha x(\text{PAH}) + \alpha^- x(\text{PAH}^-) \right\}}.$$

Since OH^+ is formed in a region where the molecular fraction is small, we can take $x(\text{H}) = 10x(\text{H}_2)$ as with [Porrás et al. \(2014\)](#) (see also Sec. 5.5, paragraph 6). Combining this with $1 = x(\text{H}) + 2x(\text{H}_2)$ from above gives $x(\text{H}) = 0.833$ and $x(\text{H}_2) = 0.083$. For the rate coefficients [$\text{cm}^3 \text{s}^{-1}$], assuming a kinetic temperature of $T = 100 \text{ K}$ for diffuse clouds, we take these values: $k_1 = 4.1 \times 10^{-11}$; $k_2 = 4.0 \times 10^{-10}$; $k_3 = 1.7 \times 10^{-9}$; $k_4 = 1.0 \times 10^{-9}$; $\beta_{\text{H}^+} = 8.0 \times 10^{-12}$; $\beta_{\text{OH}^+} = 6.6 \times 10^{-8}$. For the $\text{PAH}^{(-)}$ interactions, we adopt the scaling factor $\Phi_{\text{PAH}} = 0.5$ that takes care of the uncertainties in the PAH sizes and abundances ([Wolfire et al. 2003](#)), yielding $\alpha = 3.5 \times 10^{-8} \text{ cm}^3 \text{s}^{-1}$ and $\alpha^- = 7.0 \times 10^{-7} \text{ cm}^3 \text{s}^{-1}$. Then we take the total hydrogen density as $n_{\text{H}_{\text{tot}}} = 100 \text{ cm}^{-3}$, the fractional ionization as $x_{\text{e}^-} = 2 \times 10^{-4}$, and the fractional abundance of O as $x(\text{O}) = 3 \times 10^{-4}$. Finally, we adopt the fractional abundances of PAHs and PAH anions as $x(\text{PAH}) = 1.85 \times 10^{-7}$ and $x(\text{PAH}^-) = 1.5 \times 10^{-8}$, respectively ([Hollenbach et al. 2012](#)). Substituting all values gives us the expression for $\zeta_p [\text{s}^{-1}]$ in terms of the column densities of OH^+ and of the total hydrogen H_{tot} :

$$\zeta_p \approx 6.5 \times 10^{-8} \cdot \frac{N(\text{OH}^+)}{N(\text{H}_{\text{tot}})}. \quad (5.1)$$

With this equation it is possible to calculate the primary cosmic ray ionization rate. This requires that for the individual sightlines, $N(\text{OH}^+)$ is determined and that for $N(\text{H}_{\text{tot}})$ the corresponding values are taken from Table 5.1 where $N(\text{H}_{\text{tot}}) = N(\text{H I}) + 2N(\text{H}_2)$ or, alternatively, derived using the methods described in Sec. 5.4.2 and 5.4.2.

We want to stress that care is needed to compare the values that will be presented in the next section with those reported in the (recent) past. Eq. 5.1 has a different prefactor than used before because of incorporating different assumptions for the $\text{O}^+ + \text{H}$ charge transfer rate coefficient ($4 \times 10^{-10} \text{ cm}^3 \text{s}^{-1}$ instead of $7 \times 10^{-10} \text{ cm}^3 \text{s}^{-1}$ which is based on [Chamblaud et al. 1980](#) and [Stancil et al. 1999](#)) as well as introducing other sinks for H^+ ions. The temperature dependence of the prefactor is also already quite evident in some of the rate coefficients listed in Table 5.2, and this has a considerable effect on its resulting value. This will be discussed more in detail in Sec. 5.5.

5.4 Results

5.4.1 Equivalent widths and column densities of OH^+

Table 5.3: Rotational transitions in the $A^3\Pi - X^3\Sigma^-$ electronic band system of OH^+ .

Transition	Label	λ [Å]	$f \times 10^{-4}$	
(0,0)	$^rR_{11}(0)$	1	3583.75574(16)	5.27
	$^rQ_{21}(0)$	2	3572.65187(33)	3.12
	$^sR_{21}(0)$	3	3566.4458(11)	1.17
	$^rP_{31}(0)$	4	3565.34592(81)	1.28
	$^sQ_{31}(0)$	5	3559.8062(13)	0.87
	$^tR_{31}(0)$	6	3552.325(12)	0.05
(1,0)	$^rR_{11}(0)$	7	3346.95559(74)	3.52
	$^rQ_{21}(0)$	8	3337.3570(15)	2.06
	$^sR_{21}(0)$	9	3332.177(11)	0.82
	$^rP_{31}(0)$	10	3330.409(11)	0.85
	$^sQ_{31}(0)$	11	3326.369(11)	0.62
	$^tR_{31}(0)$	12	3319.967(11)	0.04

Notes. The wavelengths (in standard air) and the line oscillator strengths are taken from [Hodges & Bernath \(2017\)](#) and [Hodges et al. \(2018\)](#). Numbers enclosed in parentheses denote the uncertainty of the last digits.

The OH^+ electronic transitions listed in Table 5.3 were searched for in the reduced spectra from the 346-nm setting (3042–3872 \AA). The procedure of analyzing the spectrum (developed in Python) is visualized in Fig. 5.2 for a selected OH^+ transition in one of the chosen stellar targets. Following heliocentric correction, the spectrum is shifted to the rest frame of one of the components of interstellar sodium (Na I UV at 3302.3686 \AA in air (Kramida et al. [Kramida et al. \(2013\)](#)); panel a in the figure, marked with a red \times). Shown in panel b is a plot where the OH^+ line to be analyzed (the 3584 \AA transition) is located (indicated by the red crosshair) with respect to the full spectrum. A narrow wavelength range ($\sim 1\text{--}2$ \AA) is then selected, that includes the OH^+ line, after which data points are chosen where a polynomial (up to the 3rd order) is fitted (panel c). The zero-point velocity set by the Na I UV transition is indicated by the solid vertical gray line. The selected spectrum is then divided by this fitted continuum for normalization. A Voigt function is fitted to the normalized spectrum, with which the equivalent width W_λ is obtained by integrating (via Simpson integration) the area under the interpolated Voigt fit. The line is integrated within ± 17 times

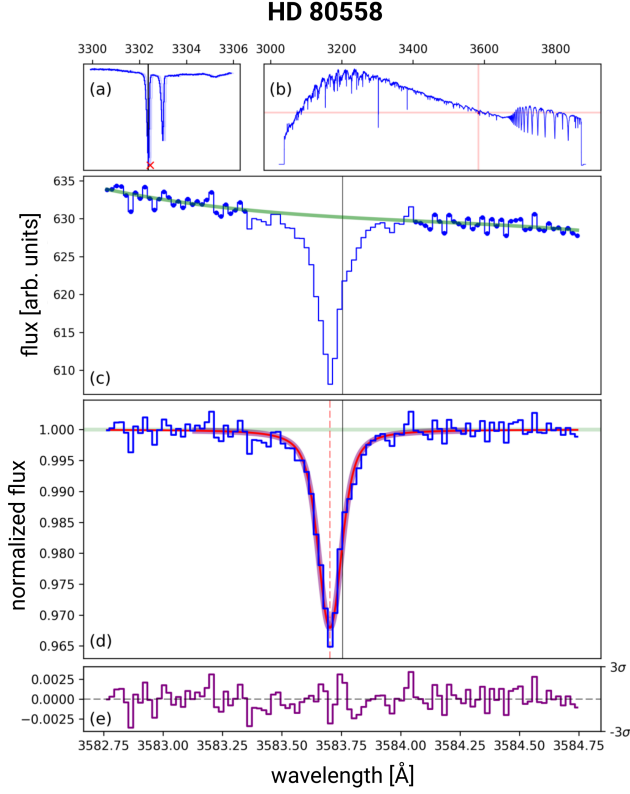


Figure 5.2: Analysis of one OH^+ line (line 1) for HD 80558. Description for each panel (a–e) can be found in the text.

the obtained sigma (= gamma) parameter from the central wavelength of the line.² The fitted profile is shown in panel d with the center wavelength indicated by the broken vertical red line. The corresponding residuals are shown in panel e. The resulting equivalent width is listed in Table 5.4, together with those derived for other transitions and other sightlines. To estimate the uncertainty in the equivalent width calculation, we use the method described in Appendix A in the work of Vos et al. (2011).

The observed OH^+ lines for each of the ten targets are compiled in Fig. 5.3. As can be seen in the figure, between two and ten absorption lines are found in each target,

² The $\pm 17\sigma$ integration bound is obtained empirically and is equivalent in area to $\pm 2 \cdot \text{FWHM}$ used for a Gaussian profile.

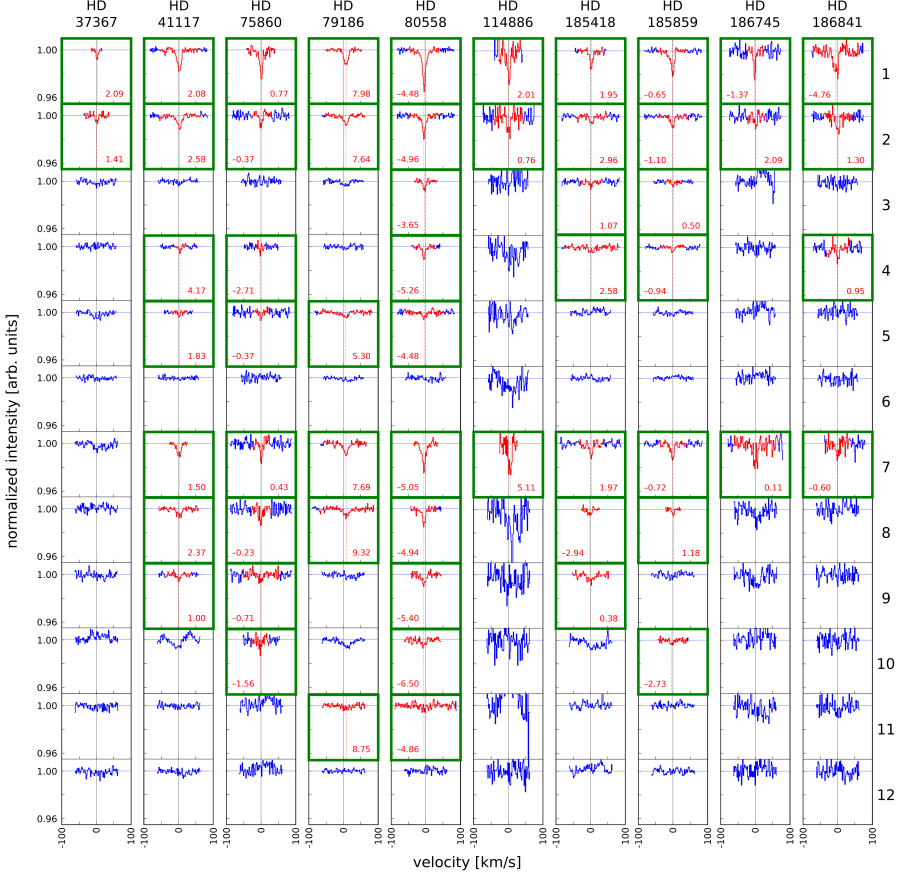


Figure 5.3: OH^+ absorption lines observed (enclosed in green boxes) for each of the ten stellar targets. Every row of boxes is labeled on the right side according to the line labeling in Table 5.3. The solid vertical gray line in each box denotes the zero-point velocity set by the Na I UV transition, while the broken vertical red line denotes the center of the fitted profile. The inset of numbers indicates the velocity difference in km s^{-1} of the OH^+ line from the rest frame of Na I UV. The red-highlighted trace in the spectrum is the region where the fitted Voigt profile is integrated. The y-scaling is uniform to emphasize the relative strengths of each of the lines in one target and among the rest. The relative S/N can also be directly compared.

with lines 1, 2, and 7 being the most intense as expected from the magnitude of their oscillator strengths. The signal-to-noise ratio (S/N) of the spectra in this wavelength range varies from 100 to 1200 per pixel (median value ~ 500) which allows for many of the weaker lines to be observed. In some of the targets, the region where the OH^+ line is observed exhibits a background continuum which can be harder to fit using a low-order polynomial. This can be due to jumps in the spectrum after echelle order merging or blending absorption from other species – stellar lines such as, for example, Fe II at 3566.2 Å, Ti II at 3332.1 Å, or Mn II at 3330.8 Å (Kurucz & Bell 1995) – which also explains why some of the weaker lines show up more than the stronger ones if they are by chance in a region with a better defined continuum. In these cases, care is taken to only include a small part of the spectrum (highlighted in red in the figure) in the equivalent width calculation.

The column density $N(\text{OH}^+)$ along a particular sightline is obtained by plotting the equivalent width [mÅ] of each absorption line against the product of the corresponding oscillator strength and the square of its wavelength [Å]. This is defined by the following approximation, valid for an optically-thin absorber (Spitzer 1978):

$$W_\lambda = N(\text{OH}^+) \cdot 8.853 \times 10^{-18} \cdot \lambda^2 f. \quad (5.2)$$

Eq. 5.2 can be used to fit a linear curve since all involved transitions originate from the same ground state level defined by the angular momentum quantum number $N = 0$. The column density is then obtained from the slope of this equation, as depicted in Fig. 5.4. The linear fit is made to intercept the origin of the graph following the obvious assumption that no equivalent width can be measured if no absorption line exists. The derived column densities for each sightline are listed in Table 5.4. With more than one OH^+ transition observed per sightline, this method allows for a better constraint in the resulting $N(\text{OH}^+)$ -value. As an added advantage, employing more than one transition also reduces the impact of having coincidental stellar contamination on any particular OH^+ line to the final measured $N(\text{OH}^+)$ -value.

As stated before, some 28 additional sightlines show (weak) OH^+ detections, typically comprising of only one transition. In principle, it is possible to derive values for ζ_p through Eq. 5.2. These are listed in Appendix A as well. However, as the Voigt fitting is complicated as some of these lines have multiple components, and the $N(\text{OH}^+)$ -values will only be derived from one OH^+ absorption line, we restrict our main conclusions to the ten targets as listed in Table 5.1. For the non-detections of OH^+ for all available sightlines in EDIBLES, we have derived the 5σ equivalent width upper limit for the strongest OH^+ line, which was estimated as $W_{\lambda(\text{limit})} = 5\sigma \sqrt{N}(\Delta\lambda)$ (Jenkins et al. 1973), with $\Delta\lambda$ as the width of each wavelength bin (binsize = 0.02 Å), N as the number of points included in the sampled $\lambda 3854 \text{ OH}^+$ line ($N = 28$), and σ as the reciprocal of the S/N around the line. An average value of 1.0 mÅ is obtained, corresponding to an upper limit column density $N(\text{OH}^+)_{(\text{limit})}$ of $2.1 \times 10^{13} \text{ cm}^{-2}$ (with a range of $0.7 - 13.5 \times 10^{13} \text{ cm}^{-2}$).

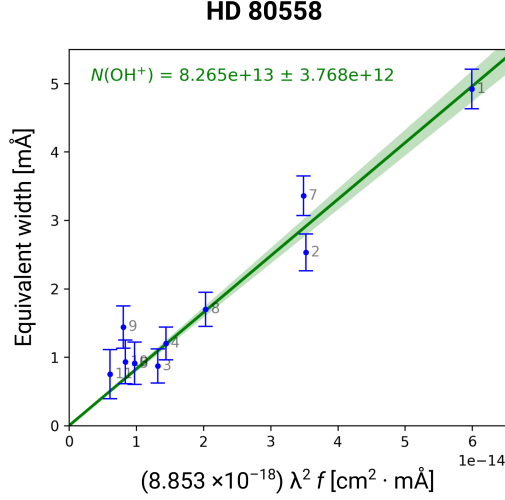


Figure 5.4: OH⁺ column density (shown here for HD 80558) derived from the slope of the line through points, plotting the equivalent width values as function of the transition wavelength and the oscillator strength, using Eq. 5.2. The line through the points is a linear fit weighted to the uncertainty of W_λ which yields a slope of $(8.3 \pm 0.4) \times 10^{13} \text{ cm}^{-2}$. Data points are marked according to the corresponding label for the OH⁺ line (Table 5.3). (See Fig. C.1 in Appendix C for the plots of the other targets.)

5.4.2 Complementary methods for deriving $N(\text{H}_{\text{tot}})$

Now that the $N(\text{OH}^+)$ -values are known, the other quantity that is needed to derive ζ_p (Eq. 5.1) is the total hydrogen column density $N(\text{H}_{\text{tot}})$ along each of the sightlines. As was described shortly in Sec. 5.3, we can directly obtain this from Table 5.1 with $N(\text{H}_{\text{tot}}) = N(\text{H I}) + 2N(\text{H}_2)$. In the next sections we will describe additional ways that we have used for deriving $N(\text{H}_{\text{tot}})$ based on interstellar reddening E_{B-V} or potassium (K I) absorption line measurements. The resulting values are summarized in Table 5.4.

$N(\text{H}_{\text{tot}})$ from interstellar reddening E_{B-V}

$N(\text{H}_{\text{tot}})$ is commonly estimated through interstellar reddening using the relation identified by Bohlin et al. (1978) for diffuse clouds: $N(\text{H}_{\text{tot}}) = 5.8 \times 10^{21} \cdot E_{B-V} \text{ cm}^{-2}$. As in the work done by Jenkins (2009), these values and relations of $N(\text{H}_{\text{tot}})$ with interstellar reddening were determined using $\text{L}\alpha$ absorption line measurements. Since the entire sightline is also considered in these measurements, the total number of hy-

drogen atoms associated with the production and destruction of OH^+ in the local interstellar cloud(s) may be overestimated. Nevertheless, these $N(\text{H}_{\text{tot}})$ -values can be easily derived, using the E_{B-V} -values listed in Table 5.1.

$N(\text{H}_{\text{tot}})$ from potassium absorption line measurements

Another independent way of deriving $N(\text{H}_{\text{tot}})$ is through an absorption line measurement of the interstellar K I doublet at 4044.1422 and 4047.2132 Å, with $f_{4044} = 5.69 \times 10^{-3}$ and $f_{4047} = 2.63 \times 10^{-3}$, respectively (Kramida et al. 2013). This approach is based on the empirical relation presented by Welty & Hobbs (2001), derived from high resolution spectral observations, that is,

$$\log[N(\text{K I})] = A + B \cdot \log[N(\text{H}_{\text{tot}})]. \quad (5.3)$$

Here, the values chosen for coefficients A and B are -26.30 ± 1.09 and 1.79 ± 0.16 , respectively. These numbers were obtained when all stars in their sample were included in the analysis (Table 5 in Welty & Hobbs 2001). The column density $N(\text{K I})$ is obtained via a similar manner as with $N(\text{OH}^+)$, that is, using the same fitting routine. The equivalent width of each of the two doublet components is then fitted with a line through the origin as defined by Eq. 5.2. This linear fit can be used since the majority of the measured W_λ -values for the K I doublet follows the ratio of their oscillator strengths, that is, $W_{4044} : 2W_{4047} \approx f_{4044} : 2f_{4047}$, which indicates that the absorption lines are well within the thin-absorber approximation. The results of these calculations are summarized in Table 5.4.

5.5 Discussion

The calculated cosmic ray ionization rates are summarized in Table 5.4. When we compare the resulting ζ_p -values using the different procedures of deriving $N(\text{H}_{\text{tot}})$, we see a range of values around $(3.9 - 24.6) \times 10^{-16} \text{ s}^{-1}$. In sightlines where information on both K I and literature values for $N(\text{H}_{\text{tot}})$ are available, some discrepancy is found between the calculated ζ_p using the two procedures, varying from a factor of 0.7 (HD 79186) to ≤ 2.0 (HD 185859). On the other hand, it is interesting to find that the values derived using E_{B-V} are not very different to those obtained through K I measurements (within 20 percent), apart from the data of HD 75860, knowing that the corresponding $N(\text{H}_{\text{tot}})$ -values can be over- or underestimated. Overall, there exists a reasonable agreement for the different approaches discussed here which is also evident in the weighted averages of the ζ_p -values. However, when comparing with other work below, we instead quote $(3.9 - 16.4) \times 10^{-16} \text{ s}^{-1}$, with a weighted average of $8.5(4) \times 10^{-16} \text{ s}^{-1}$; this result only includes the ζ_p -values derived using the $N(\text{H}_{\text{tot}})$ from Table 5.1 since these come from more reliable and direct vacuum-UV measurements of $N(\text{H I})$ and $N(\text{H}_2)$. These $N(\text{H}_{\text{tot}})$ -values serve as upper limits to the actual amount of hydrogen that is involved in the formation of OH^+ .

Table 5.4: *continued.*

Identifier	OH ⁺		K I		$N(\text{H}_{\text{tot}}) \times 10^{21} [\text{cm}^{-2}]$		$\zeta_p \times 10^{-16} [\text{s}^{-1}]$	
	$W_\lambda [\text{m}]$ (0,0)	$N(\text{OH}^+) \times 10^{13} [\text{cm}^{-2}]$	$W_\lambda [\text{m}]$	$N(\text{K I}) \times 10^{13} [\text{cm}^{-2}]$	Table 1	E_{B-V}	Table 1	E_{B-V}
HD 185418	1 1.9(5) 2 0.9(5) 3 0.5(4) 4 0.9(7)	3.3(3)	7 1.3(4) 8 0.7(5) 9 1.4(7)	0.132(3)	2.6	2.44	2.9(1)	8.4(8) 8.9(8) 7.4(7)
HD 185859	1 3.0(4) 2 1.5(4) 3 0.4(3) 4 0.5(4)	4.3(4)	7 1.7(4) 8 0.5(3) 10 0.5(4)	0.175(1)	≥ 1.7	3.25	3.40(1)	≤ 16.4 8.6(8) 8.2(8)
HD 186745	1 1.9(7) 2 0.9(7)	3.4(8)	7 3.0(1.1)	0.38(7)	...	5.10	5.3(1.0)	...
HD 186841	1 4.1(1.2) 2 1.8(1.0) 4 1.3(8)	5.3(9)	7 1.3(8)	0.395(1)	...	5.51	5.37(1)	...
ζ_p weighted average:					8.5(4)	8.5(3)	7.5(4)	

Notes. For the OH⁺ equivalent width measurements in column 2, each of the values is preceded with a number labeling the absorption line as listed in Table 5.3; for the K I W_λ -values, labels 1 and 2 represent the 4044 Å and the 4047 Å components, respectively. The total hydrogen column density $N(\text{H}_{\text{tot}})$ is obtained via three ways: derived from Table 5.1 where $N(\text{H}_{\text{tot}}) = N(\text{H I}) + 2N(\text{H}_2)$, from E_{B-V} , and from $N(\text{K I})$ (columns 7–9). The corresponding cosmic ray ionization rates ζ_p calculated using each of these $N(\text{H}_{\text{tot}})$ -values are listed in columns 10–12. Numbers enclosed in parentheses denote the uncertainty of the last digit(s); for example, $1.2(3) \equiv 1.2 \pm 0.3$, whereas $4.3(2.1) \equiv 4.3 \pm 2.1$.

Before we can start comparing our results with other near-UV studies, we note that [Porrás et al. \(2014\)](#) and [Zhao et al. \(2015\)](#) have adopted a similar formula (Eq. 5.1) but with a prefactor ($\sim 1.3 \times 10^{-8} \text{ s}^{-1}$) which is five times smaller, based on the rate equations provided by [Federman et al. \(1996\)](#). As discussed in Sec. 5.3, in these studies the recombination of protons on PAHs was not taken into account. We have also left out the He^+ recombination rate found in their formulation after considering the reaction channels listed in Table 5.2. Apart from the new prefactor, it should also be noted that new OH^+ line oscillator strengths from [Hodges et al. \(2018\)](#) were used for updating the results obtained from previous near-UV work ([Porrás et al. 2014](#), [Zhao et al. 2015](#)) for a fully consistent comparison. The updated results are listed in Table B.1 together with the original values previously reported.

The adapted ζ_p -values from [Zhao et al. \(2015\)](#), with a range of $(6.6 - 11.1) \times 10^{-16} \text{ s}^{-1}$ and a weighted average of $8.6(2) \times 10^{-16} \text{ s}^{-1}$, are consistent and in the same order as our results. We also find a similar agreement with the adapted results of [Porrás et al. \(2014\)](#) with a range of ζ_p -values equal to $(2.2 - 20.6) \times 10^{-16} \text{ s}^{-1}$, though the average value is about 50 percent higher ($12.1 \times 10^{-16} \text{ s}^{-1}$). The exceptions are three interstellar velocity components in the sightlines toward HD 149404, HD 154368, and HD 183143. In those cases, the OH^+ lines are very weak (not even the CH^+ counterpart³ is detected), suggesting that these extreme values should be viewed with caution. Also, care must be taken in directly comparing the results obtained from individual velocity components and from total sightline measurements (as in this work). Despite the seemingly similar ranges, it should be noted that these comparisons should not be taken at face value since individual targets are likely to be in quite unique physical environments, as shown by the differences in ζ_p of up to more than an order of magnitude. A thorough statistical treatment of the data may help distinguish any difference in the distribution of the sightlines.

As for the 28 targets with (weak) single- OH^+ line detection (Appendix A), we get a range of $(1.3 - 9.4) \times 10^{-16} \text{ s}^{-1}$ which overlaps with or is close to our results for the ten main targets but does so on the lower side of the range. The disparity becomes more clear when comparing weighted averages; the single-line targets have an average ζ_p -value of $3.0(3) \times 10^{-16} \text{ s}^{-1}$ which is about three times lower than what we have for the multiline targets. Looking at the OH^+ column densities, we see that the results for the ten selected lines-of-sight with multiple transitions (Fig. 5.3) are systematically higher ($(1.3 - 8.3) \times 10^{13} \text{ cm}^{-2}$) than those derived for the 28 lines-of-sight for which only one transition (line 1) is observed ($(0.5 - 2.4) \times 10^{13} \text{ cm}^{-2}$). This difference cannot be attributed by having a [more accurate] multiple line fit, as focusing only on the transition with the largest oscillator strength (line 1) in these lines-of-sight results in comparable (though less accurate) $N(\text{OH}^+)$ -values. The selection of targets with multiple OH^+ transitions comes with a bias, namely, that the $N(\text{OH}^+)$ -values measured for those environments are larger. The $N(\text{OH}^+)$ abundances clearly span a

³ This is based on studies by, for example, [Krełowski et al. \(2010a\)](#) and [Porrás et al. \(2014\)](#), which suggest that OH^+ and CH^+ are associated with each other.

range of values somewhat more than an order of magnitude and this results in a range of ζ_p -values as well; similarly, variations in $N(\text{H}_{\text{tot}})$ also affect the derived ζ_p -values. When the ten main and 28 additional targets are taken together, we get an average ζ_p -value of $5.1(3) \times 10^{-16} \text{ s}^{-1}$.

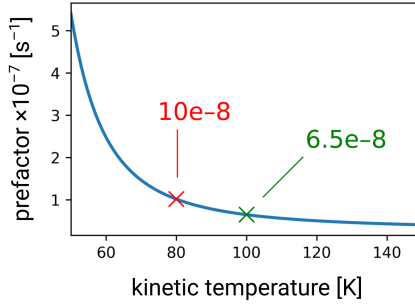


Figure 5.5: Effect of the temperature dependence of the reaction rate constants to the resulting prefactor in Eq. 5.1. The prefactor for $T = 80 \text{ K}$ and $T = 100 \text{ K}$ are highlighted in red and green, respectively.

We can also compare our work with other cosmic ray ionization rate investigations using other methods and tracers. Noting that ζ_p is approximately related to the cosmic ray ionization rates of atomic and molecular hydrogen by $\zeta_p = \zeta_{\text{H}}/1.5 = \zeta_{\text{H}_2}/2.3$ (Glassgold & Langer 1974), we find that our results are generally higher. These comparisons include detections of OH^+ and H_2O^+ in the submm region (Neufeld et al. 2010, Indriolo et al. 2012) which give $\zeta_p \sim (0.4 - 3.0) \times 10^{-16} \text{ s}^{-1}$ and H_3^+ in the infrared (Le Petit et al. 2004, Indriolo et al. 2007, Indriolo & McCall 2012, Indriolo et al. 2012, 2015, Neufeld & Wolfire 2017) which give $\zeta_p \sim (0.5 - 4.6) \times 10^{-16} \text{ s}^{-1}$. Although McCall et al. (2003) had derived a high ζ_p -value of $12 \times 10^{-16} \text{ s}^{-1}$ using H_3^+ observations along the sightline towards ζ Persei, this was subsequently updated to a much lower value of $2.5 \times 10^{-16} \text{ s}^{-1}$ by Le Petit et al. (2004) with a more detailed photodissociation region (PDR) cloud model.

Comparing results obtained using the same tracer can shed some light on the possible environmental differences in the various sightlines studied thus far. Another useful exercise is to see how different tracers of the cosmic ray ionization rate compare for the same sightline. This will indicate how well our existing models for different tracers are able to describe the mechanism behind the processes taking place in these environments. In Table D.1, we list sightlines from our EDIBLES data set (as well as from Krelowski et al. 2010a and Porras et al. 2014) where we have OH^+ data (or upper limits) with corresponding H_3^+ data (or upper limits) from the work of Indriolo & McCall (2012) and Albertsson et al. (2014). All of the targets listed have a single OH^+ absorption line measured apart from HD 41117 where we have detected seven

lines. For this target, the ζ_p -value we get from our work is about five times higher than the value obtained by Albertsson et al. Other targets with both OH^+ and H_3^+ detection show more or less the same, overlapping values (HD 24398, HD 110432, HD 154368, HD 169454). For HD 183143, a measurement by Porras et al. and by Indriolo & McCall corresponds to the same velocity component ($v_{\odot} = -10 \text{ km s}^{-1}$ and $v_{\text{LSR}} = 7 \text{ km s}^{-1}$, respectively), but the derived ζ_p -values differ by about five times. As for upper limits, care should be taken in comparing them. It should be kept in mind that the cosmic ray ionization rate values deduced will rely on specific assumptions regarding, for example, density and temperature. However, the general trend that the ζ_p -values derived from OH^+ observations is larger than that derived from H_3^+ may reflect an actual decrease of this quantity from the edge of these molecular clouds toward the center which may be exhibited thanks to the spatial stratification of the OH^+ and H_3^+ molecular ions. Such a possibility was raised independently by [Rimmer et al. \(2011\)](#) in order to understand the presence of carbon chains in the illuminated part of the Horsehead nebula. A recent theoretical study on the penetration of cosmic rays in diffuse clouds by [Phan et al. \(2018\)](#) also points out to that possibility. The results we obtained for diffuse clouds follow the general trend of values being an order of magnitude larger than the cosmic ray ionization rates found in dense molecular clouds ([van der Tak & van Dishoeck 2000](#), [Kulesa 2002](#)).

With all of these comparisons it is important to realize how, in our formulation, the prefactor in Eq. 5.1 is influenced by a variety of parameters. One of these is the assumption made regarding the relative fractional abundances of hydrogen, that is, $x(\text{H}) = 10x(\text{H}_2)$. As can be seen in Table 5.1, the relative hydrogen column densities do not necessarily follow this relationship, and most of them fall short on a factor 10. Thus, if we use the actual measured column densities of H I and H_2 in our formulation, this would yield a unique prefactor in Eq. 5.1 for every sightline. Other factors such as the O and the $\text{PAH}^{(-)}$ abundances may also play crucial roles in the resulting ζ_p -values. Clearly, there exists a need for a thorough investigation on how these parameters, as well as the properties of the individual sightlines, dictate the numbers that we get.

Another factor worth considering is the temperature dependence of the prefactor, mainly driven by the $\text{H}^+ + \text{O}$ charge-exchange rate coefficient k_1 . This charge-exchange takes place with atomic oxygen in its $J = 2$ ground level and has an $\exp(-227/T)$ temperature dependence, corresponding to the endothermicity of the reaction. It can be seen from the abundance equation for OH^+ (Sec. 5.3) that k_1 is the only T -dependent factor in the numerator of $x(\text{OH}^+)$ and dominates the denominator at higher T which causes the steep rise in the prefactor as T falls below 60 K and the gradual decline as T rises above 100 K (with other reactions having weaker T -dependence). The overall T -dependence is shown in Fig. 5.5 – a change in T from 80 K to 100 K can give a difference in the prefactor by about 1.5 times. (For our case, we take a temperature of $T = 100 \text{ K}$ as the typical temperature in diffuse clouds.) Four of our sightlines have data for T_{01} ([Rachford et al. 2002, 2009](#), [Sheffer et al. 2008](#)) which range from 59 K for HD 41117 and 101 K for HD 185418, and these correspond

to cosmic ray ionization rates which may vary by about a factor of four. Moreover, reactions between molecular hydrogen and O^+/OH^+ have also been recently studied in ion trap experiments at low temperatures (Kovalenko et al. 2018, Tran et al. 2018). The derived rate coefficients corresponding to k_3 and k_4 are within the same order of magnitude as with previous values, which give differences in the calculated ζ_p by at most 20 percent. (We keep the values of k_3 and k_4 used by other authors for the purpose of a consistent comparison with other near-UV studies.) Given these existing dependencies, care is needed in using specific cosmic ray ionization rates.

Searching for these near-UV OH^+ transitions in other galaxies is also promising. There have already been a number of extragalactic detections of OH^+ , which include studies by van der Werf et al. (2010), González-Alfonso et al. (2013), Riechers et al. (2013), and recently by Muller et al. (2016) who have found slightly higher values of ζ_p for the $z = 0.89$ absorber PKS 1830-211 measured within a similar galactocentric radius as in studies of the Milky Way (Indriolo et al. 2015); they attributed this to the higher star formation rate in the former. They got values of $\zeta_p \sim 130 \times 10^{-16}$ and $20 \times 10^{-16} \text{ s}^{-1}$, along sightlines located at $\sim 2 \text{ kpc}$ and $\sim 4 \text{ kpc}$ to either side of the galactic center, respectively. Recently, Indriolo et al. (2018) have also reported ζ_p -values ranging from the high $\sim 10^{-17}$ to 10^{-15} toward the $z \sim 2.3$ lensed galaxies SMM J2135-0102 and SDP 17b from observations of both OH^+ and H_2O^+ . All of these studies have so far looked at the submm transitions of OH^+ , and thus, having complementary observations in the near-UV and in the optical for these [high-redshift] extragalactic (albeit faint) targets would help us in probing variations of the cosmic ray ionization rate over cosmic timescales.

5.6 Conclusions

In this contribution, we have determined cosmic ray ionization rates along ten diffuse interstellar sightlines through the measurement of OH^+ abundances which are constrained better with the detection of more near-UV OH^+ electronic transitions. The explicit incorporation of proton recombinations on PAHs increases the historically used prefactor for the $N(\text{OH}^+)/N(\text{H}_{\text{tot}})$ ratio and results in larger cosmic ray ionization rates. We obtain a range of ζ_p -values equal to $(3.9 - 16.4) \times 10^{-16} \text{ s}^{-1}$, which is generally much higher than what was derived in previous studies from detections of interstellar OH^+ in the far-infrared / submillimeter-wave regions but is comparable to measurements in the near-ultraviolet using a reformulated abundance equation for interstellar OH^+ , as introduced here. An additional constraint on the physical conditions prevailing in these diffuse lines-of-sight, and on the derived primary cosmic ray ionization rate, could be obtained through the detection of H_2O^+ absorption transitions which occur in the visible (Lew 1976, Gredel et al. 2001). This ion has been detected in the ISM in the infrared by *Herschel* (e.g., Ossenkopf et al. 2010) but not yet in the optical. H_2O^+ is indeed formed directly through the $\text{OH}^+ + \text{H}_2$ reaction and its destruction results from dissociative recombination by electrons and a further

reaction with H₂. These signatures will be searched in the EDIBLES spectra. Finally, it will be interesting to investigate whether the (non)detection of OH⁺ can be linked to the (non)appearance of specific DIBs, as currently is being investigated for EDIBLES data linking selected DIBs to C₂ (Elyajouri et al. 2018).

Acknowledgments

This work is based on observations obtained at the European Organization for Astronomical Research in the Southern Hemisphere under ESO programs 194.C-0833 and 266.D-5655. X.L.B. thanks Edcel Salumbides for fruitful discussions and the whole EDIBLES team for their support and for making the reduced UVES data available. J.C. and A.F. acknowledge support from an NSERC Discovery Grant and a Western Accelerator Award. H.L. acknowledges support through NOVA and NWO. E.R. acknowledges support by the Programme National “Physique et Chimie du Milieu Interstellaire” (PCMI) of CNRS/INSU with INC/INP co-funded by CEA and CNES.

Appendix

A EDIBLES targets with very weak OH⁺ absorptions

Table A.1 is a comprehensive list of additional EDIBLES sightlines that show some weak OH⁺ absorption that can be discerned through visual inspection, but are excluded in the present analysis.

Table A.1: Estimated cosmic ray ionization rates for EDIBLES targets with a single OH^+ absorption ($\lambda 3584$).

Identifier	W_{3584} [m]	$N(\text{OH}^+)$ $\times 10^{13} [\text{cm}^{-2}]$	$N(\text{H}_{\text{tot}})$ $\times 10^{21} [\text{cm}^{-2}]$	ζ_p $\times 10^{-16} [\text{s}^{-1}]$	Identifier	W_{3584} [m]	$N(\text{OH}^+)$ $\times 10^{13} [\text{cm}^{-2}]$	$N(\text{H}_{\text{tot}})$ $\times 10^{21} [\text{cm}^{-2}]$	ζ_p $\times 10^{-16} [\text{s}^{-1}]$
HD 22951	0.4(3)	0.7(5)	1.7	2.7(1.8)	HD 152408	1.4(7)	2.4(1.2)	2.3	6.7(3.3)
HD 23180	0.3(3)	0.5(4)	1.6	2.2(1.7)	HD 152424	1.3(7)	2.1(1.1)	3.8*	3.6(1.8)
HD 24398	0.3(3)	0.5(4)	1.6	2.1(1.8)	HD 154043	0.9(6)	1.5(9)	4.6*	2.2(1.3)
HD 37903	0.5(5)	0.9(8)	2.7	2.0(1.9)	HD 155806	0.7(3)	1.1(4)	1.4	5.4(2.0)
HD 75309	0.9(6)	1.6(1.0)	1.5	6.9(4.4)	HD 166937	0.8(2)	1.4(3)	1.3*	7.1(1.5)
HD 111934	0.7(6)	1.2(9)	2.0*	4.0(3.1)	HD 167264	0.7(3)	1.1(5)	1.8	4.1(1.9)
HD 113904	0.5(3)	0.8(6)	1.3	3.8(2.7)	HD 167838	0.6(6)	0.9(1.0)	4.1*	1.5(1.7)
HD 122879	0.4(4)	0.6(6)	2.2	1.9(1.8)	HD 169454	0.8(9)	1.4(1.4)	6.9*	1.3(1.4)
HD 145502	0.5(4)	0.8(7)	1.3	3.8(3.3)	HD 170740	0.7(3)	1.1(5)	2.5	2.8(1.2)
HD 148937	0.8(6)	1.4(1.0)	5.0	1.8(1.2)	HD 171957	0.8(4)	1.4(6)	1.6*	5.8(2.5)
HD 149038	1.3(1.1)	2.3(1.8)	1.6	9.4(7.3)	HD 172694	1.4(5)	2.3(8)	2.0*	7.6(2.5)
HD 149404	0.7(3)	1.2(5)	3.9*	1.9(8)	HD 180554	0.4(2)	0.7(4)
HD 151804	0.9(5)	1.6(8)	1.6	6.4(3.1)	HD 184915	0.3(2)	0.6(3)	1.1	3.3(1.9)
HD 152248	0.6(4)	1.0(7)	≥ 1.7	≤ 3.9	HD 303308	0.9(8)	1.7(1.3)	3.0	3.6(2.8)

Notes. For weak absorption features with multiple components, an integrated area over ~ 1 centered at $\lambda 3584$ is reported; these values are indicated by the italicized numbers. The $N(\text{H}_{\text{tot}})$ -values are derived from Cox et al. (Cox et al. (2017)); the ones with an asterisk (*) are derived (as described in Sec. 5.4.2) from the E_{B-V} -values taken from the same reference. Numbers enclosed in parentheses denote the uncertainty of the last digit(s); for example, 1.2(3) $\equiv 1.2 \pm 0.3$, whereas 4.3(2.1) $\equiv 4.3 \pm 2.1$.

B Compilation of estimates of ζ_p derived from OH⁺ detections in the near-UV

Table B.1: Literature values for $N(\text{OH}^+)$ together with the [estimated] $N(\text{H}_{\text{tot}})$ column densities and the corresponding ζ_p , both the values reported originally and the values adapted here to follow Eq. 5.1.

Target	scaled $N(\text{OH}^+)$ $\times 10^{13} [\text{cm}^{-2}]$	$N(\text{H}_{\text{tot}})$ $\times 10^{21} [\text{cm}^{-2}]$	original ζ_p $\times 10^{-16} [\text{s}^{-1}]$	adapted ζ_p $\times 10^{-16} [\text{s}^{-1}]$
<u>Porras et al. (2014)</u>				
BD-14 5037	0.58	0.22	1.6	17.3
	1.9	2.3	0.5	5.4
HD 149404	0.41	1.2	0.2	2.2
	0.87 ^a	0.095 ^a	5.5 ^a	59.5 ^a
HD 154368	1.1	0.54	1.2	13.0
	0.65	0.30	1.3	14.1
	0.37 ^a	0.067 ^a	3.3 ^a	35.7 ^a
	0.91	1.1	0.5	5.4
HD 183143	0.35	0.16	1.3	14.1
	2.4	0.75	1.9	20.6
	0.61 ^a	0.060 ^a	6.1 ^a	66.0 ^a
	0.67	0.25	1.6	17.3
<u>Zhao et al. (2015)</u>				
CD-32 4348	6.3(3)	5.7	0.8	7.2(3)
HD 63804	7.7(3)	4.5	1.2	11.1(4)
HD 78344	4.0(4)	4.0	0.8	6.6(7)
HD 80077	4.2(6)	3.7	0.9	7.3(1.0)

Notes. The OH⁺ column densities reported by Porras et al. (2014) were derived from a single electronic transition ($\lambda 3584$) while those of Zhao et al. (2015) result from a line fit through multiple OH⁺ absorption lines, as in this work. These values have been scaled according to the recently updated line oscillator strengths provided by Hodges et al. (2018). Numbers enclosed in parentheses denote the uncertainty of the last digit(s); for example, 1.2(3) $\equiv 1.2 \pm 0.3$, whereas 4.3(2.1) $\equiv 4.3 \pm 2.1$.

^a Values reported for these components correspond to very weak OH⁺ absorption components with no corresponding CH⁺ detections. The associated $N(\text{H}_{\text{tot}})$ is likely underestimated leading to overestimated values for ζ_p .

C Linear regression results for $N(\text{OH}^+)$

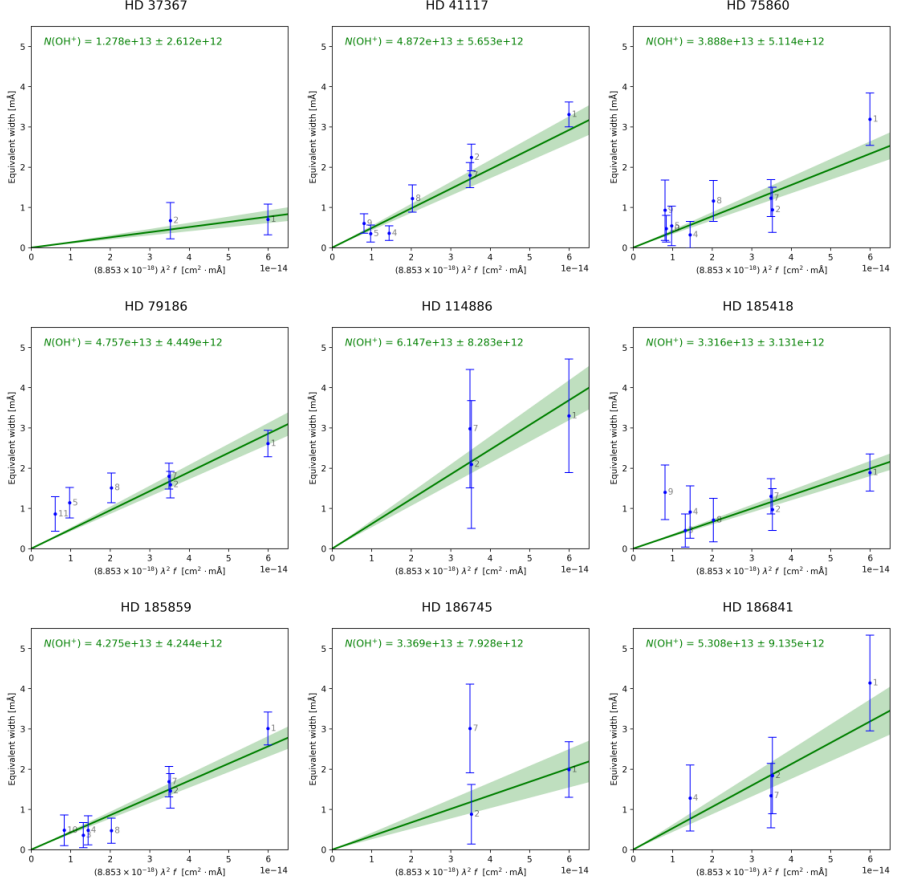


Figure C.1: Weighted linear fits for deriving $N(\text{OH}^+)$ for all targets except HD 80558 (Fig. 5.4). A couple of outliers can be noticed for some of the sightlines as in the cases for HD 185418 and HD 186745 which could well be caused by poor S/N (see Fig. 5.3) and/or possible contamination with some weak absorption features. This behavior is also seen in the measurements for the weaker OH^+ lines in HD 79186. Setting the intercept to zero helps constrain the effect of these biases.

Table D.1: A comparison of primary cosmic ray ionization rates ζ_p among targets which have detections for both OH^+ (This work; Krelowski et al. 2010a; Porras et al. 2014) and H_3^+ (Indriolo & McCall 2012; Albertsson et al. 2014).

Identifier	$\text{OH}^+ \zeta_p \times 10^{-16} \text{ s}^{-1}$		$\text{H}_3^+ \zeta_p \times 10^{-16} \text{ s}^{-1}$	
	This work	Krelowski et al. (2010a)	Porras et al. (2014)	Indriolo & McCall (2012) Albertsson et al. (2014)
HD 22951	2.7(1.8)	≤ 1.2 ...
HD 23180	2.2(1.7)	≤ 1.8 ...
HD 24398	2.1(1.8)	2.4(1.4) ...
HD 27778	≤ 9.8	≤ 4.5 2.3(3)
HD 41117	10.3(8)	≤ 6.0 2.3(7)
HD 43384	≤ 8.6 1.1(3)
HD 110432	...	2.7(1.4)	...	1.7(9) ...
HD 147888	≤ 2.2	≤ 20.1 ...
HD 147889	≤ 15.7	≤ 0.8 ...
HD 149038	9.4(7.3)	≤ 2.4 ...
HD 149404	1.9(8)	6.1(3.1)	2.2, 59.5, ^a 13.0, 14.1	≤ 1.9 ...
HD 149757	≤ 5.3	≤ 0.8 ...
HD 154368	...	3.4(2.0)	35.7, ^a 5.4, 14.1	1.8(1.1) ...
HD 169454	1.3(1.4)	1.1(8) ...
HD 183143	20.6*, 66.0, ^a 17.3	4.6(3.6)*, 3.4(2.6) ...
BD-14 5037	17.3, 5.4	≤ 0.3 ...

Notes. The HD 149404 data from Porras et al. (2014) come from four velocity components, while the HD 154368 and HD 183143 data come from three. The HD 183143 data from Indriolo & McCall (2012) come from two velocity components, one of which, at $v_{\text{LSR}} = 7 \text{ km s}^{-1}$, corresponds to a component measured by Porras et al. at $v_{\odot} = -10 \text{ km s}^{-1}$ (each component marked with an asterisk). Upper limits reported by Indriolo & McCall are expressed here as 5σ results. Values reported in the last column have been computed with the same assumptions as in Indriolo & McCall (2012). Numbers enclosed in parentheses denote the uncertainty of the last digit(s); for example, 1.2(3) $\equiv 1.2 \pm 0.3$, whereas 4.3(2.1) $\equiv 4.3 \pm 2.1$.

^a Values reported for these components correspond to very weak OH^+ absorption components with no corresponding CH^+ detections. The associated $N(\text{H}_{\text{tot}})$ is likely underestimated leading to overestimated values for ζ_p .

Bibliography

- Adams, W. S. "Some results with the Coudé spectrograph of the Mount Wilson Observatory." *Astrophys. J.* **93** (1941) 11.
- Albertsson, T., Indriolo, N., Kreckel, H., et al. "First time-dependent study of H_2 and H_3^+ ortho-para chemistry in the diffuse interstellar medium: Observations meet theoretical predictions." *Astrophys. J.* **787** (2014) 44.
- Allamandola, L. J., Tielens, A. G. G. M., & Barker, J. R. "Polycyclic aromatic hydrocarbons and the unidentified infrared emission bands — Auto exhaust along the Milky Way." *Astrophys. J.* **290** (1985) L25.
- Allen, M. & Robinson, G. W. "The molecular composition of dense interstellar clouds." *Astrophys. J.* **212** (1977) 396.
- Araki, M., Cias, P., Denisov, A., et al. "Electronic spectroscopy of the nonlinear carbon chains C_4H_4^+ and C_8H_4^+ ." *Can. J. Chem.* **82** (2004) 848–853.
- Bacalla, X., Zhao, D., Salumbides, E. J., et al. "The $\text{B}^2\Pi\text{--X}^2\Pi$ electronic origin band of $^{13}\text{C}_6\text{H}$." *J. Mol. Spectrosc.* **308-309** (2015) 41–44.
- Bacalla, X. L. "The $\text{B}^2\Pi\text{--X}^2\Pi$ electronic origin transition of the $^{13}\text{C}_6\text{H}$ isotopologue." Master's thesis, University of San Carlos (2014).
- Barlow, M. J., Swinyard, B. M., Owen, P. J., et al. "Detection of a noble gas molecular ion, $^{36}\text{ArH}^+$, in the Crab Nebula." *Science* **342** (2013) 1343–1345.
- Beals, C. S. & Blanchet, G. H. "A line at $\lambda 4430.5$ of possibly interstellar origin." *Publ. Astron. Soc. Pac.* **49** (1937) 224.
- Belloche, A., Garrod, R. T., Muller, H. S. P., et al. "Detection of a branched alkyl molecule in the interstellar medium: iso-propyl cyanide." *Science* **345** (2014) 1584–1587.
- Berden, G. & Engeln, R. (eds.). *Cavity Ring-Down Spectroscopy*. John Wiley and Sons Ltd (2009). ISBN 1405176881.
- Berden, G., Peeters, R., & Meijer, G. "Cavity ring-down spectroscopy: Experimental schemes and applications." *Int. Rev. Phys. Chem.* **19** (2000) 565–607.
- Berné, O., Mulas, G., & Joblin, C. "Interstellar C_{60}^+ ." *Astron. Astrophys.* **550** (2013) L4.
- Berné, O., Cox, N. L. J., Mulas, G., et al. "Detection of buckminsterfullerene emission

- in the diffuse interstellar medium.” *Astron. Astrophys.* **605** (2017) L1.
- Bhatt, N. H. & Cami, J. “A sensitive spectral survey of interstellar features in the near-UV [3050–3700 Å].” *Astrophys. J. Suppl. S.* **216** (2015) 22.
- Birza, P., Khoroshev, D., Chirokolava, A., et al. “Lifetime broadening in the gas phase $B^2\Pi-X^2\Pi$ electronic spectrum of C_8H .” *Chem. Phys. Lett.* **382** (2003) 245–248.
- Bohlin, R. C., Savage, B. D., & Drake, J. F. “A survey of interstellar H I from L-alpha absorption measurements. II.” *Astrophys. J.* **224** (1978) 132–142.
- Bonaca, A. & Bilalbegović, G. “Optical spectrum of proflavine and its ions.” *Chem. Phys. Lett.* **493** (2010) 33–36.
- Bregman, J. D., Dinerstein, H. L., Goebel, J. H., et al. “Observations of NGC 7027 from 5.2 to 7.5 microns — The detection of Ni II and additional dust features.” *Astrophys. J.* **274** (1983) 666.
- Brown, S. T., Rienstra-Kiracofe, J. C., & Schaefer III, H. F. “A systematic application of density functional theory to some carbon-containing molecules and their anions.” *J. Phys. Chem. A* **103** (1999) 4065–4077.
- Cami, J. & Cox, N. L. J. (eds.). *The Diffuse Interstellar Bands*, IAU Symposium **297**. Cambridge Univ. Press, Cambridge (2014).
- Cami, J., Sonnentrucker, P., Ehrenfreund, P., et al. “Diffuse interstellar bands in single clouds: New families and constraints on the carriers.” *Astron. Astrophys.* **326** (1997) 822–830.
- Cami, J., Bernard-Salas, J., Peeters, E., et al. “Detection of C_{60} and C_{70} in a young planetary nebula.” *Science* **329** (2010) 1180.
- Cami, J., Cox, N. L. J., Farhang, A., et al. “The ESO Diffuse Interstellar Band Large Exploration Survey (EDIBLES).” *The Messenger* **171** (2018) 31–36.
- Campbell, E. K., Holz, M., Gerlich, D., et al. “Laboratory confirmation of C_{60}^+ as the carrier of two diffuse interstellar bands.” *Nature* **523** (2015) 322–323.
- Campbell, E. K., Holz, M., Maier, J. P., et al. “Gas phase absorption spectroscopy of C_{60}^+ and C_{70}^+ in a cryogenic ion trap: Comparison with astronomical measurements.” *Astrophys. J.* **822** (2016a) 17.
- Campbell, E. K., Holz, M., & Maier, J. P. “ C_{60}^+ in diffuse clouds: Laboratory and astronomical comparison.” *Astrophys. J. Lett.* **826** (2016b) L4.
- Cao, Z. & Peyerimhoff, S. D. “Electronic spectra of linear isoelectronic species HC_6H^+ , C_6H , HC_5N^+ .” *Phys. Chem. Chem. Phys.* **3** (2001) 1403–1406.
- Cardelli, J. A., Clayton, G. C., & Mathis, J. S. “The relationship between infrared, optical, and ultraviolet extinction.” *Astrophys. J.* **345** (1989) 245.
- Carruthers, G. R. “Rocket observation of interstellar molecular hydrogen.” *Astrophys. J.* **161** (1970) L81.
- Cernicharo, J. & Guélin, M. “Metals in IRC+10216 — Detection of NaCl, AlCl, and KCl, and tentative detection of AlF.” *Astron. Astrophys.* **183** (1987) L10–L12.
- Cernicharo, J., Guélin, M., Menten, K. M., et al. “ C_6H : Astronomical study of its fine and hyperfine structure.” *Astron. Astrophys.* **181** (1987) L1–L4.
- Cernicharo, J., Goicoechea, J. R., & Caux, E. “Far-infrared detection of C_3 in Sagit-

- tarius B2 and IRC+10216." *Astrophys. J.* **534** (2000) L199–L202.
- Cernicharo, J., Guélin, M., Agúndez, M., et al. "Detection of C_5N^- and vibrationally excited C_6H in IRC+10216." *Astrophys. J.* **688** (2008) L83–L86.
- Chambaud, G., Levy, B., Millie, P., et al. "Charge exchange and fine-structure excitation in $O-H^+$ collisions." *J. Phys. Pt. B Atom. M. P.* **13** (1980) 4205–4216.
- Chang, C.-H., Agarwal, J., Allen, W. D., et al. "Sub-doppler infrared spectroscopy and formation dynamics of triacetylene in a slit supersonic expansion." *J. Chem. Phys.* **144** (2016) 074301.
- Cheung, A. C., Rank, D. M., Townes, C. H., et al. "Detection of water in interstellar regions by its microwave radiation." *Nature* **221** (1969) 626–628.
- Cohen, M., Anderson, C. M., Cowley, A., et al. "The peculiar object HD 44179 ('The Red Rectangle')." *Astrophys. J.* **196** (1975) 179.
- Cordiner, M. A. & Sarre, P. J. "The CH_2CN^- molecule: carrier of the $\lambda 8037$ diffuse interstellar band?" *Astron. Astrophys.* **472** (2007) 537–545.
- Cordiner, M. A., Cox, N. L. J., Trundle, C., et al. "Detection of diffuse interstellar bands in M31." *Astron. Astrophys.* **480** (2008) L13–L16.
- Cordiner, M. A., Cox, N. L. J., Lallement, R., et al. "Searching for interstellar C_{60}^+ using a new method for high signal-to-noise HST/STIS spectroscopy." *Astrophys. J.* **843** (2017) L2.
- Cordiner, M. A., Linnartz, H., Cox, N. L. J., et al. "Confirming interstellar C_{60}^+ using the Hubble Space Telescope." *Astrophys. J. Lett.* **875** (2019) L28.
- Cox, N. L. J., Ehrenfreund, P., Foing, B. H., et al. "Linear and circular spectropolarimetry of diffuse interstellar bands." *Astron. Astrophys.* **531** (2011) A25.
- Cox, N. L. J., Cami, J., Kaper, L., et al. "VLT/X-Shooter survey of near-infrared diffuse interstellar bands." *Astron. Astrophys.* **569** (2014) A117.
- Cox, N. L. J., Cami, J., Farhang, A., et al. "The ESO Diffuse Interstellar Bands Large Exploration Survey (EDIBLES)." *Astron. Astrophys.* **606** (2017) A76.
- Crawford, M. K., Tielens, A. G. G. M., & Allamandola, L. J. "Ionized polycyclic aromatic hydrocarbons and the diffuse interstellar bands." *Astrophys. J.* **293** (1985) L45.
- Crawford, T. M. "Error sources in the 'ring down' optical cavity decay time mirror reflectometer." In: Stotlar, S. C. (ed.), *Southwest Conference on Optics '85, SPIE* **0540** (1985) .
- Dalgarno, A. "Interstellar chemistry special feature: The galactic cosmic ray ionization rate." *P. Natl. Acad. Sci. USA* **103** (2006) 12269–12273.
- Danks, A. C. & Lambert, D. L. "Line profiles of the diffuse interstellar lines at 5780 Å, 5797 Å." *Mon. Not. R. Astron. Soc.* **174** (1976) 571–586.
- Davis, L., Jr. & Greenstein, J. L. "The polarization of starlight by aligned dust grains." *Astrophys. J.* **114** (1951) 206.
- de Almeida, A. A. "Possible OH^+ submillimeter emission in Orion-KL." *Rev. Mex. Astron. Astrofis.* **21** (1990) 499–503.
- de Almeida, A. A. & Singh, P. D. "The OH^+ molecule in interstellar clouds: Absolute

- oscillator strengths and equivalent widths for OH^+ ($A^3\Pi_i - X^3\Sigma^-$) bands.” *Astron. Astrophys.* **95** (1981) 383.
- Dekker, H., D’Odorico, S., Kaufer, A., et al. “Design, construction, and performance of UVES, the echelle spectrograph for the UT2 Kueyen Telescope at the ESO Paranal Observatory.” In: Iye, M. & Moorwood, A. F. (eds.), *Optical and IR Telescope Instrumentation and Detectors*, *SPIE* **4008** (2000) 534–545.
- Denisov, A. “Electronic spectroscopy of unsaturated hydrocarbons and sulfur-terminated carbon chains by cavity ringdown.” Ph.D. thesis, Universität Basel (2006).
- Dickens, J. E., Irvine, W. M., Ohishi, M., et al. “Detection of interstellar ethylene oxide ($\text{c-C}_2\text{H}_4\text{O}$).” *Astrophys. J.* **489** (1997) 753–757.
- Diplas, A. & Savage, B. D. “An IUE survey of interstellar $\text{H I Ly}\alpha$ absorption. I: Column densities.” *Astrophys. J. Suppl. S.* **93** (1994) 211–228.
- Douglas, A. E. “Origin of diffuse interstellar lines.” *Nature* **269** (1977) 130–132.
- Douglas, A. E. & Herzberg, G. “Band spectrum and structure of the CH^+ molecule: Identification of three interstellar lines.” *Can. J. Res.* **20a** (1942) 71–82.
- Doyle, T., Shen, L., Rittby, C., et al. “A $\text{C}\equiv\text{C}$ stretching vibration of the C_6H (hexatriynyl) radical in Ar at 10 K.” *J. Chem. Phys.* **95** (1991) 6224–6228.
- Ehrenfreund, P., Cami, J., Jiménez-Vicente, J., et al. “Detection of diffuse interstellar bands in the magellanic clouds.” *Astrophys. J.* **576** (2002) L117–L120.
- Elyajouri, M., Lallement, R., Cox, N. L. J., et al. “The EDIBLES survey. III. C_2 -DIBs and their profiles.” *Astron. Astrophys.* **616** (2018) A143.
- Federman, S. R., Weber, J., & Lambert, D. L. “Cosmic ray-induced chemistry toward Perseus OB2.” *Astrophys. J.* **463** (1996) 181.
- Ferrière, K. M. “The interstellar environment of our galaxy.” *Rev. Mod. Phys.* **73** (2001) 1031–1066.
- Fiedler, S. E. “Incoherent broad-band cavity-enhanced absorption spectroscopy.” Ph.D. thesis, Technical University of Berlin (2005).
- Fiedler, S. E., Hese, A., & Ruth, A. A. “Incoherent broad-band cavity-enhanced absorption spectroscopy.” *Chem. Phys. Lett.* **371** (2003) 284–294.
- Foing, B. H. & Ehrenfreund, P. “Detection of two interstellar absorption bands coincident with spectral features of C_{60}^+ .” *Nature* **369** (1994) 296–298.
- Foing, B. H. & Ehrenfreund, P. “New evidences for interstellar C_{60}^+ .” *Astron. Astrophys.* **317** (1997) L59–L62.
- Forney, D., Fulara, J., Freivogel, P., et al. “Electronic absorption spectra of linear carbon chains in neon matrices. I. C_6^- , C_6 , and C_6H .” *J. Chem. Phys.* **103** (1995) 48–53.
- Freivogel, P., Fulara, J., Jakobi, M., et al. “Electronic absorption spectra of linear carbon chains in neon matrices. II. C_{2n}^- , C_{2n} , and C_{2n}H .” *J. Chem. Phys.* **103** (1995) 54–59.
- Friedman, S. D., York, D. G., McCall, B. J., et al. “Studies of diffuse interstellar bands V. Pairwise correlations of eight strong dibs and neutral hydrogen, molecular

- hydrogen, and color excess." *Astrophys. J.* **727** (2010) 33.
- Fulara, J., Jakobi, M., & Maier, J. P. "Electronic and infrared spectra of C_{60}^+ and C_{60}^- in neon and argon matrices." *Chem. Phys. Lett.* **211** (1993a) 227–234.
- Fulara, J., Lessen, D., Freivogel, P., et al. "Laboratory evidence for highly unsaturated hydrocarbons as carriers of some of the diffuse interstellar bands." *Nature* **366** (1993b) 439–441.
- Furton, D. G. & Witt, A. N. "Extended red emission from dust in planetary nebulae." *Astrophys. J.* **386** (1992) 587.
- Galazutdinov, G. & Krelowski, J. "Looking for the weak members of the C_{60}^+ family in the interstellar medium." *Acta Astronomica* **67** (2017) 159–169.
- Galazutdinov, G., Lee, B.-C., Song, I.-O., et al. "A search for interstellar naphthalene and anthracene cations." *Mon. Not. R. Astron. Soc.* (2011) 1259–1264.
- Galazutdinov, G. A., LoCurto, G., & Krelowski, J. "High-resolution profiles of diffuse interstellar bands." *Astrophys. J.* **682** (2008) 1076–1086.
- Galazutdinov, G. A., Shimansky, V. V., Bondar, A., et al. " C_{60}^+ — looking for the bucky-ball in interstellar space." *Mon. Not. R. Astron. Soc.* **465** (2017) 3956–3964.
- Geballe, T. R. "The diffuse interstellar bands — A brief review." *J. Phys. Conf. Ser.* **728** (2016) 062005.
- Geballe, T. R., Najarro, F., Figer, D. F., et al. "Infrared diffuse interstellar bands in the galactic centre region." *Nature* **479** (2011) 200–202.
- Gerin, M., Luca, M. D., Black, J., et al. "Interstellar OH^+ , H_2O^+ and H_3O^+ along the sight-line to G10.6–0.4." *Astron. Astrophys.* **518** (2010) L110.
- Glassgold, A. E. & Langer, W. D. "Model calculations for diffuse molecular clouds." *Astrophys. J.* **193** (1974) 73–91.
- González-Alfonso, E., Fischer, J., Bruderer, S., et al. "Excited OH^+ , H_2O^+ , and H_3O^+ in NGC 4418 and Arp 220." *Astron. Astrophys.* **550** (2013) A25.
- Gottlieb, C. A., McCarthy, M. C., & Thaddeus, P. "Vibrationally excited C_6H ." *Astrophys. J. Suppl. S.* **189** (2010) 261–269.
- Gredel, R., Black, J. H., & Yan, M. "Interstellar C_2 and CN toward the Cyg OB2 association." *Astron. Astrophys.* **375** (2001) 553–565.
- Greenberg, J. M. & Stoeckly, R. "Shape of the diffuse interstellar bands." *Nature Physical Science* **230** (1971) 15–16.
- Guélin, M., Cernicharo, J., Gomez-Gonzalez, J., et al. "Detection of a heavy radical in IRC+10216: The hexatriynyl radical C_6H ?" *Astron. Astrophys.* **175** (1987) L5–L8.
- Haddad, M. "Cavity ring-down laser spectroscopy of carbon-chain molecules." Ph.D. thesis, Vrije Universiteit Amsterdam (2014).
- Haddad, M., Zhao, D., Linnartz, H., et al. "The $^2\Pi - \tilde{X}^2\Pi$ electronic spectra of the long carbon-chain $^{13}C_{2n}H/D$ molecules for ($n = 4 - 6$)." *Mol. Phys.* **113** (2015) 2063–2072.
- Hall, J. S. "Observations of the polarized light from stars." *Science* **109** (1949) 166–167.
- Hartmann, J. "Investigations on the spectrum and orbit of δ Orionis." *Astrophys. J.*

- 19 (1904) 268.
- Heger, M. L. "The spectra of certain class B stars in the regions 5630Å–6680Å and 3280Å–3380Å." *Lick Observatory Bulletin* **10** (1922) 146–147.
- Herbig, G. H. "The diffuse interstellar bands. I. A possible identification of λ 4430." *Astrophys. J.* **137** (1963) 200.
- Herbig, G. H. "The diffuse interstellar bands. IV — The region 4400–6850 Å." *Astrophys. J.* **196** (1975) 129.
- Herbig, G. H. "The diffuse interstellar bands." *Annu. Rev. Astron. Astrophys.* **33** (1995) 19–73.
- Herbst, E. & Klemperer, W. "The formation and depletion of molecules in dense interstellar clouds." *Astrophys. J.* **185** (1973) 505.
- Herbst, E. & van Dishoeck, E. F. "Complex organic interstellar molecules." *Annu. Rev. Astron. Astr.* **47** (2009) 427–480.
- Herriott, D. R. & Schulte, H. J. "Folded optical delay lines." *Appl. Opt.* **4** (1965) 883.
- Herzberg, G. *Molecular Spectra and Molecular Structure I. Spectra of Diatomic Molecules*. D. Van Nostrand, New York (1950).
- Herzberg, G. *Molecular Spectra and Molecular Structure III. Electronic Spectra and Electronic Structure of Polyatomic Molecules*. D. Van Nostrand, New York (1966).
- Herzberg, G. "Remarks on the diffuse interstellar lines." In: van Woerden, H. (ed.), *Radio Astronomy and the Galactic System, IAU Symposium* **31** (1967) 91.
- Hiltner, W. A. "On the presence of polarization in the continuous radiation of stars. II." *Astrophys. J.* **109** (1949) 471.
- Hobbs, L. M., York, D. G., Thorburn, J. A., et al. "Studies of the diffuse interstellar bands. III. HD 183143." *Astrophys. J.* **705** (2009) 32–45.
- Hodges, J. N. & Bernath, P. F. "Fourier transform spectroscopy of the $A^3\Pi - X^3\Sigma^-$ transition of OH^+ ." *Astrophys. J.* **840** (2017) 81.
- Hodges, J. N., Bittner, D. M., & Bernath, P. F. "Improved ultraviolet and infrared oscillator strengths for OH^+ ." *Astrophys. J.* **855** (2018) 21.
- Hollenbach, D., Kaufman, M. J., Neufeld, D., et al. "The chemistry of interstellar OH^+ , H_2O^+ , and H_3O^+ : Inferring the cosmic-ray ionization rates from observations of molecular ions." *Astrophys. J.* **754** (2012) 105.
- Holmlid, L. "Rydberg matter as the diffuse interstellar band (DIB) carrier in interstellar space: the model and accurate calculations of band centres." *Phys. Chem. Chem. Phys.* **6** (2004) 2048.
- Hoshina, K., Kohguchi, H., Ohshima, Y., et al. "Laser-induced fluorescence spectroscopy of the C_4H and C_4D radicals in a supersonic jet." *J. Chem. Phys.* **108** (1998) 3465–3478.
- Hougen, J. T. "Rotational energy levels of a linear triatomic molecule in a $^2\Pi$ electronic state." *J. Chem. Phys.* **36** (1962) 519–534.
- Iglesias-Groth, S., Machado, A., García-Hernández, D. A., et al. "Evidence for the naphthalene cation in a region of the interstellar medium with anomalous microwave emission." *Astrophys. J.* **685** (2008) L55–L58.

- Iglesias-Groth, S., Manchado, A., Rebolo, R., et al. "A search for interstellar anthracene towards the perseus anomalous microwave emission region." *Mon. Not. R. Astron. Soc.* **407** (2010) 2157–2165.
- Indriolo, N. & McCall, B. J. "Investigating the cosmic-ray ionization rate in the galactic diffuse interstellar medium through observations of H_3^+ ." *Astrophys. J.* **745** (2012) 91.
- Indriolo, N. & McCall, B. J. "Cosmic-ray astrochemistry." *Chem. Soc. Rev.* **42** (2013) 7763.
- Indriolo, N., Geballe, T. R., Oka, T., et al. " H_3^+ in diffuse interstellar clouds: A tracer for the cosmic-ray ionization rate." *Astrophys. J.* **671** (2007) 1736–1747.
- Indriolo, N., Neufeld, D. A., Gerin, M., et al. "Chemical analysis of a diffuse cloud along a line of sight toward W51: Molecular fraction and cosmic-ray ionization rate." *Astrophys. J.* **758** (2012) 83.
- Indriolo, N., Neufeld, D. A., Gerin, M., et al. "Herschel survey of galactic OH^+ , H_2O^+ , and H_3O^+ : Probing the molecular hydrogen fraction and cosmic-ray ionization rate." *Astrophys. J.* **800** (2015) 40.
- Indriolo, N., Bergin, E. A., Falgarone, E., et al. "Constraints on the cosmic-ray ionization rate in the $z \sim 2.3$ lensed galaxies SMM J2135-0102 and SDP 17b from observations of OH^+ and H_2O^+ ." *Astrophys. J.* **865** (2018) 127.
- Ityaksov, D. "Cavity ring-down optical extinction measurements of atmospheric molecules." Ph.D. thesis, Vrije Universiteit Amsterdam (2009).
- Jenkins, E. B. "A unified representation of gas-phase element depletions in the interstellar medium." *Astrophys. J.* **700** (2009) 1299–1348.
- Jenkins, E. B., Drake, J. F., Morton, D. C., et al. "Spectrophotometric results from the copernicus satellite. V. Abundances of molecules in interstellar clouds." *Astrophys. J. Lett.* **181** (1973) L122.
- Jenniskens, P. & Désert, F.-X. "A survey of diffuse interstellar bands (3800–8680 Å)." *Astron. Astrophys. Suppl. Ser.* **106** (1994) 39–78.
- Jochnowitz, E. B. & Maier, J. P. "Electronic spectroscopy of carbon chains." *Annu. Rev. Phys. Chem.* **59** (2008) 519–544.
- Jog, C. J. "Starbursts triggered by cloud compression in interacting galaxies." In: Barnes, J. E. & Sanders, D. B. (eds.), *Galaxy Interactions at Low and High Redshift*, *IAU Symposium* **186** (1999) 235.
- Junkkarinen, V. T., Cohen, R. D., Beaver, E. A., et al. "Dust and diffuse interstellar bands in the $z_a = 0.524$ absorption system toward AO 0235+164." *Astrophys. J.* **614** (2004) 658–670.
- Kaur, D., de Souza, A. M., Wanna, J., et al. "Multipass cell for molecular beam absorption spectroscopy." *Appl. Opt.* **29** (1990) 119.
- Kawaguchi, K., Kasai, Y., Ishikawa, S.-I., et al. "A spectral-line survey observation of IRC+10216 between 28 and 50 GHz." *Publ. Astron. Soc. Jpn.* **47** (1995) 853–876.
- Knöckel, H., Bodermann, B., & Tiemann, E. "High precision description of the rovibronic structure of the I_2 B-X spectrum." *Eur. Phys. J. D* **28** (2004) 199–209.

- Kogut, A., Banday, A. J., Bennett, C. L., et al. "Microwave emission at high galactic latitudes in the four-year DMR sky maps." *Astrophys. J.* **464** (1996) L5–L9.
- Kotterer, M. & Maier, J. P. "Electronic spectrum of C_6H : $^2\Pi-X^2\Pi$ in the gas-phase detected by cavity ringdown." *Chem. Phys. Lett.* **266** (1997) 342–346.
- Kovalenko, A., Dung Tran, T., Rednyk, S., et al. " OH^+ formation in the low-temperature $O^+(^4S) + H_2$ reaction." *Astrophys. J.* **856** (2018) 100.
- Kramida, A., Ralchenko, Y., Reader, J., et al. NIST Atomic Spectra Database (ver. 5.1) [Online], Available: <http://physics.nist.gov/asd>, National Institute of Standards and Technology, Gaithersburg, MD (2013).
- Krätschmer, W. "Carbon molecules as possible carrier of the diffuse interstellar bands." *Astrophys. Space Sci.* **128** (1986) 93–99.
- Krelowski, J. & Walker, G. A. H. "Three families of diffuse interstellar bands?" *Astrophys. J.* **312** (1987) 860.
- Krelowski, J., Beletsky, Y., & Galazutdinov, G. A. "Hydroxyl cation in translucent interstellar clouds." *Astrophys. J. Lett.* **719** (2010a) L20–L22.
- Krelowski, J., Beletsky, Y., Galazutdinov, G. A., et al. "Evidence for diacetylene cation as the carrier of a diffuse interstellar band." *Astrophys. J.* **714** (2010b) L64–L67.
- Krelowski, J., Galazutdinov, G., & Kołos, R. "Can H_2CCC be the carrier of broad diffuse bands?" *Astrophys. J.* **735** (2011) 124.
- Kroto, H. W. "The stability of the fullerenes C_n , with $n = 24, 28, 32, 36, 50, 60$ and 70 ." *Nature* **329** (1987) 529–531.
- Kroto, H. W. & Jura, M. "Circumstellar and interstellar fullerenes and their analogues." *Astron. Astrophys.* **263** (1992) 275–280.
- Kuhn, M., Renzler, M., Postler, J., et al. "Atomically resolved phase transition of fullerene cations solvated in helium droplets." *Nat. Commun.* **7** (2016).
- Kulesa, C. A. "Molecular hydrogen and its ions in dark interstellar clouds and star forming regions." Ph.D. thesis, The University of Arizona (2002).
- Kurucz, R. L. & Bell, B. *Atomic line list*. Smithsonian Astrophysical Observatory, Cambridge, MA (1995).
- Lallement, R., Cox, N. L. J., Cami, J., et al. "The EDIBLES survey II. The detectability of C_{60}^+ bands." *Astron. Astrophys.* **614** (2018) A28.
- Le Petit, F., Roueff, E., & Herbst, E. " H_3^+ and other species in the diffuse cloud towards ζ Persei: A new detailed model." *Astron. Astrophys.* **417** (2004) 993–1002.
- Leger, A. & d'Hendecourt, L. "Are polycyclic aromatic hydrocarbons the carriers of the diffuse interstellar bands in the visible?" *Astron. Astrophys.* **146** (1985) 81–85.
- Leger, A., D'Hendecourt, L., Verstraete, L., et al. "Remarkable candidates for the carrier of the diffuse interstellar bands - C_{60}^+ and other polyhedral carbon ions." *Astron. Astrophys.* **203** (1988) 145–148.
- Leitch, E. M., Readhead, A. C. S., Pearson, T. J., et al. "An anomalous component of galactic emission." *Astrophys. J.* **486** (1997) L23–L26.

- Lepp, S., Dalgarno, A., van Dishoeck, E. F., et al. "Large molecules in diffuse interstellar clouds." *Astrophys. J.* **329** (1988) 418.
- Lew, H. "Electronic spectrum of H_2O^+ ." *Can. J. Phys.* **54** (1976) 2028–2049.
- Linnartz, H., Motylewski, T., Vaizert, O., et al. "Electronic ground and excited state spectroscopy of C_6H and C_6D ." *J. Mol. Spectrosc.* **197** (1999) 1–11.
- Linnartz, H., Bossa, J.-B., Bouwman, J., et al. "Solid state pathways towards molecular complexity in space." In: Cernicharo, J. & Bachiller, R. (eds.), *The Molecular Universe, IAU Symposium* **280**. Cambridge University Press (CUP) (2011) 390–404.
- Linnartz, H., Ioppolo, S., & Fedoseev, G. "Atom addition reactions in interstellar ice analogues." *Int. Rev. Phys. Chem.* **34** (2015) 205–237.
- Liszt, H., Sonnentrucker, P., Cordiner, M., et al. "The abundance of C_3H_2 and other small hydrocarbons in the diffuse interstellar medium." *Astrophys. J.* **753** (2012) L28.
- Liu, R., Zhou, X., & Pulay, P. "Ab initio study of the geometry, stretching, vibrations, and assignment of the observed frequencies of the ground state C_6H (hexatriynyl) radical." *J. Chem. Phys.* **97** (1992) 1602–1605.
- Lloyd, G. M. & Ewart, P. "High resolution spectroscopy and spectral simulation of C_2 using degenerate four-wave mixing." *J. Chem. Phys.* **110** (1999) 385–392.
- Loomis, F. W. & Brandt, W. H. "The band spectrum of OH^+ ." *Phys. Rev.* **49** (1936) 55–67.
- Maier, J., Walker, G., Bohlender, D., et al. "Identification of H_2CCC as a diffuse interstellar band carrier." *Astrophys. J.* **726** (2011a) 41.
- Maier, J. P., Chakrabarty, S., Mazzotti, F. J., et al. "Assignment of 5069 Å diffuse interstellar band to HC_4H^+ : Disagreement with laboratory absorption band." *Astrophys. J. Lett.* **729** (2011b) L20.
- Martin, F., Bacis, R., Churassy, S., et al. "Laser-induced-fluorescence fourier transform spectrometry of the XO_g^+ state of I_2 : Extensive analysis of the $\text{BO}_u^+ \rightarrow \text{XO}_g^+$ fluorescence spectrum of $^{127}\text{I}_2$." *J. Mol. Spectrosc.* **116** (1986) 71–100.
- Martin, P. G., Illing, R., & Angel, J. R. P. "Discovery of interstellar circular polarization in the direction of the Crab nebula." *Mon. Not. R. Astron. Soc.* **159** (1972) 191–201.
- McCall, B., Thorburn, J., Hobbs, L., et al. "Rejection of the C_7 -diffuse interstellar band hypothesis." *Astrophys. J. Lett.* **559** (2001) L49.
- McCall, B. J. & Griffin, R. E. "On the discovery of the diffuse interstellar bands." *P. Roy. Soc. A-Math. Phys.* **469** (2013) 2012.0604.
- McCall, B. J., Huneycutt, A. J., Saykally, R. J., et al. "An enhanced cosmic-ray flux towards ζ Persei inferred from a laboratory study of the $\text{H}_3^+ \cdot \text{e}^-$ recombination rate." *Nature* **422** (2003) 500–502.
- McCarthy, M., Gottlieb, C., Gupta, H., et al. "Laboratory and astronomical identification of the negative molecular ion C_6H^- ." *Astrophys. J. Lett.* **652** (2006) L141.
- McCarthy, M. C. & Thaddeus, P. "Rotational spectrum and carbon-13 hyperfine struc-

- ture of the C_3H , C_5H , C_6H , and C_7H radicals." *J. Chem. Phys.* **122** (2005) 174308.
- McGuire, B. A. "2018 Census of interstellar, circumstellar, extragalactic, protoplanetary disk, and exoplanetary molecules." *Astrophys. J. Suppl. Ser.* **239** (2018) 17.
- McGuire, B. A., Carroll, P. B., Loomis, R. A., et al. "Discovery of the interstellar chiral molecule propylene oxide (CH_3CHCH_2O)." *Science* **352** (2016) 1449–1452.
- McKellar, A. "Evidence for the molecular origin of some hitherto unidentified interstellar lines." *Publ. Astron. Soc. Pac.* **52** (1940) 187.
- McKellar, A. "Some topics in molecular astronomy." *J. R. Astron. Soc. Can.* **54** (1960) 97.
- McManus, J. B., Kebabian, P. L., & Zahniser, M. S. "Astigmatic mirror multipass absorption cells for long-path-length spectroscopy." *Appl. Opt.* **34** (1995) 3336.
- Menten, K. M. & Wyrowski, F. "Molecules detected in interstellar space." In: Yamada, K. M. T. & Winnewisser, G. (eds.), *Interstellar Molecules, Springer Tracts in Modern Physics* **241** (2011) 27–42.
- Merer, A. J., Malm, D. N., Martin, R. W., et al. "The ultraviolet emission spectra of OH^+ and OD^+ . Rotational structure and perturbations in the $A^3\Pi_i - X^3\Sigma^-$ transition." *Can. J. Phys.* **53** (1975) 251.
- Merrill, P. W. "Unidentified interstellar lines." *Publ. Astron. Soc. Pac.* **46** (1934) 206.
- Merrill, P. W. & Wilson, O. C. "Unidentified interstellar lines in the yellow and red." *Astrophys. J.* **87** (1938) 9.
- Motylewski, T. & Linnartz, H. "Cavity ring down spectroscopy on radicals in a supersonic slit nozzle discharge." *Rev. Sci. Instrum.* **70** (1999) 1305–1312.
- Motylewski, T., Linnartz, H., Vaizert, O., et al. "Gas-phase electronic spectra of carbon-chain radicals compared with diffuse interstellar band observations." *Astrophys. J.* **531** (2000) 312.
- Moutou, C., Krelowski, J., D'Hendecourt, L., et al. "On correlations between diffuse interstellar bands." *Astron. Astrophys.* **351** (1999) 680–688.
- Muller, S., Müller, H. S. P., Black, J. H., et al. " OH^+ and H_2O^+ absorption toward PKS 1830–211." *Astron. Astrophys.* **595** (2016) A128.
- Nagarajan, R. & Maier, J. P. "Electronic spectra of carbon chains and derivatives." *Int. Rev. Phys. Chem.* **29** (2010) 521–554.
- Neufeld, D. A. & Wolfire, M. G. "The cosmic-ray ionization rate in the galactic disk, as determined from observations of molecular ions." *Astrophys. J.* **845** (2017) 163.
- Neufeld, D. A., Goicoechea, J. R., Sonnentrucker, P., et al. "Herschel/HIFI observations of interstellar OH^+ and H_2O^+ towards W49N: A probe of diffuse clouds with a small molecular fraction." *Astron. Astrophys.* **521** (2010) L10.
- Öberg, K. I. "Photochemistry and astrochemistry: Photochemical pathways to interstellar complex organic molecules." *Chem. Rev.* **116** (2016) 9631–9663.
- O'Keefe, A. & Deacon, D. A. "Cavity ring-down optical spectrometer for absorption measurements using pulsed laser sources." *Rev. Sci. Instrum.* **59** (1988) 2544–2551.
- Ossenkopf, V., Müller, H. S. P., Lis, D. C., et al. "Detection of interstellar oxidaniumyl: Abundant H_2O^+ towards the star-forming regions DR21, Sgr B2, and NGC6334."

- Astronomy and Astrophysics* **518** (2010) L111.
- Pauzat, F. & Ellinger, Y. "The lowest two electronic states of the hexatriynil radical: C_6H ." *Astron. Astrophys.* **216** (1989) 305–309.
- Pearson, J. C., Gottlieb, C. A., Woodward, D. R., et al. "Laboratory detection of the C_6H radical." *Astron. Astrophys.* **189** (1988) L13–L15.
- Pflüger, D., Motylewski, T., Linnartz, H., et al. "Rotationally resolved $A^2\Pi_u - X^2\Pi_g$ electronic spectrum of tetraacetylene cation." *Chem. Phys. Lett.* **329** (2000) 29–35.
- Phan, V. H. M., Morlino, G., & Gabici, S. "What causes the ionization rates observed in diffuse molecular clouds? The role of cosmic ray protons and electrons." *Mon. Not. R. Astron. Soc.* **480** (2018) 5167–5174.
- Porras, A. J., Federman, S. R., Welty, D. E., et al. " OH^+ in diffuse molecular clouds." *Astrophys. J. Lett.* **781** (2014) L8.
- Puget, J. L., Leger, A., & Boulanger, F. "Contribution of large polycyclic aromatic molecules to the infrared emission of the interstellar medium." *Astron. Astrophys.* **142** (1985) L19–L22.
- Puspitarini, L., Lallement, R., Babusiaux, C., et al. "The Gaia-ESO survey: Extracting diffuse interstellar bands from cool star spectra." *Astron. Astrophys.* **573** (2015) A35.
- Rachford, B. L., Snow, T. P., Tumlinson, J., et al. "A far ultraviolet spectroscopic explorer survey of interstellar molecular hydrogen in translucent clouds." *Astrophys. J.* **577** (2002) 221–244.
- Rachford, B. L., Snow, T. P., Destree, J. D., et al. "Molecular hydrogen in the far ultraviolet spectroscopic explorer translucent lines of sight: The full sample." *Astron. and Astrophys. Suppl. Ser.* **180** (2009) 125–137.
- RaghuNandan, R., Mazzotti, F. J., & Maier, J. P. "Electronic spectra of C_6H^+ and $C_6H_3^+$ in the gas phase." *J. Am. Soc. Mass Spectr.* **21** (2010) 694–697.
- Rice, C. A. & Maier, J. P. "Electronic spectroscopy of carbon chains and rings of astrophysical interest." *J. Phys. Chem. A* **117** (2013) 5559–5566.
- Riechers, D. A., Bradford, C. M., Clements, D. L., et al. "A dust-obscured massive maximum-starburst galaxy at a redshift of 6.34." *Nature* **496** (2013) 329–333.
- Rimmer, P. B., Herbst, E., Morata, O., et al. "Observing a column-dependent ζ in dense interstellar sources: the case of the Horsehead nebula." *Astron. Astrophys.* **537** (2011) A7.
- Rodebush, W. H. & Wahl, M. H. "The reactions of the hydroxyl radical in the electrodeless discharge in water vapor." *J. Chem. Phys.* **1** (1933) 696–702.
- Romanini, D., Ventrillard, I., Méjean, G., et al. "Introduction to cavity enhanced absorption spectroscopy." In: Gagliardi, G. & Loock, H. (eds.), *Cavity-Enhanced Spectroscopy and Sensing, Springer Series in Optical Sciences* **179**. Springer-Verlag, Berlin Heidelberg. ISBN 978-3-642-40002-5 (2014) .
- Russell, R. W., Soifer, B. T., & Willner, S. P. "The 4 to 8 micron spectrum of NGC 7027." *Astrophys. J.* **217** (1977) L149.
- Saha, M. N. "Molecules in interstellar space?" *Nature* **139** (1937) 840–840.

- Salama, F., Galazutdinov, G., Krelowski, J., et al. "Polycyclic aromatic hydrocarbons and the diffuse interstellar bands: A survey." *Astrophys. J.* **526** (1999) 265.
- Salama, F., Galazutdinov, G. A., Krelowski, J., et al. "Polycyclic aromatic hydrocarbons and the diffuse interstellar bands: A survey." *Astrophys. J.* **728** (2011) 154.
- Sarre, P., Miles, J., Kerr, T., et al. "Resolution of intrinsic fine structure in spectra of narrow diffuse interstellar bands." *Mon. Not. R. Astron. Soc.* **277** (1995) L41–L43.
- Sarre, P. J. "Diffuse bands in emission." *Nature* **351** (1991) 356–356.
- Sarre, P. J. "The diffuse interstellar bands: A major problem in astronomical spectroscopy." *J. Mol. Spectrosc.* **238** (2006) 1–10.
- Searles, J. M., Destree, J. D., Snow, T. P., et al. "Searching for naphthalene cation absorption in the interstellar medium." *Astrophys. J.* **732** (2011) 50.
- Sellgren, K., Werner, M. W., Ingalls, J. G., et al. "C₆₀ in reflection nebulae." *Astrophys. J.* **722** (2010) L54–L57.
- Sheffer, Y., Rogers, M., Federman, S. R., et al. "Ultraviolet survey of CO and H₂ in diffuse molecular clouds: The reflection of two photochemistry regimes in abundance relationships." *Astrophys. J.* **687** (2008) 1075–1106.
- Shnitko, I., Fulara, J., Batalov, A., et al. "³Σ[−] – ³Σ[−] electronic transition of linear C₆H⁺ and C₈H⁺ in neon matrixes." *J. Phys. Chem. A* **110** (2006) 2885–2889.
- Smith, I. W. "Laboratory astrochemistry: Gas-phase processes." *Annu. Rev. Astron. Astr.* **49** (2011) 29–66.
- Snow, T. P. "Diffuse interstellar bands: Past and present." In: *The Diffuse Interstellar Bands, IAU Symposium* **297** (2014) 3–12.
- Snow, T. P. & McCall, B. J. "Diffuse atomic and molecular clouds." *Annu. Rev. Astron. Astr.* **44** (2006) 367–414.
- Snow, T. P., Zukowski, D., & Massey, P. "The intrinsic profile of the 4428 Å diffuse interstellar band." *Astrophys. J.* **578** (2002) 877–884.
- Snow, T. P., Jr. & Cohen, J. G. "Diffuse interstellar band formation in dense clouds." *Astrophys. J.* **194** (1974) 313.
- Sobolewski, A. L. & Adamowicz, L. "Ab initio characterization of electronically excited states in highly unsaturated hydrocarbons." *J. Chem. Phys.* **102** (1995) 394–399.
- Solomon, P. M. & Wickramasinghe, N. C. "Molecular and solid hydrogen in dense interstellar clouds." *Astrophys. J.* **158** (1969) 449.
- Sonnentrucker, P., York, B., Hobbs, L. M., et al. "A modern census of the broadest diffuse interstellar bands." *Astrophys. J. Suppl. Ser.* **237** (2018) 40.
- Sorokin, P., Glowina, J., & Ubachs, W. "Current status of the H₂ diffuse interstellar bands theory." *Farad. Discuss.* **109** (1998) 137–163.
- Sorokin, P. P. & Glowina, J. H. "Nonlinear spectroscopy in astronomy: assignment of diffuse interstellar absorption bands to L(α)-induced, two-photon absorption by H₂ molecules." *Chem. Phys. Lett.* **234** (1995) 1–6.
- Spieler, S., Kuhn, M., Postler, J., et al. "C₆₀⁺ and the diffuse interstellar bands: An

- independent laboratory check.” *Astrophys. J.* **846** (2017) 168.
- Spitzer, L. *Physical processes in the interstellar medium*. New York Wiley-Interscience (1978).
- Stancil, P. C., Schultz, D. R., Kimura, M., et al. “Charge transfer in collisions of O^+ with H and H^+ with O.” *Astron. Astrophys. Suppl. Ser.* **140** (1999) 225–234.
- Stecher, T. P. “Interstellar extinction in the ultraviolet.” *Astrophys. J.* **142** (1965) 1683.
- Suzuki, H., Ohishi, M., Kaifu, N., et al. “Detection of the interstellar C_6H radical.” *Publ. Astron. Soc. Jpn.* **38** (1986) 911–917.
- Swings, P. “A note on molecular absorption in interstellar space.” *Mon. Not. R. Astron. Soc.* **97** (1937) 212.
- Swings, P. & Rosenfeld, L. “Considerations regarding interstellar molecules.” *Astrophys. J.* **86** (1937) 483–486.
- Taylor, T. R., Xu, C., & Neumark, D. M. “Photoelectron spectra of the $C_{2n}H^-$ ($n = 1 - 4$) and $C_{2n}D^-$ ($n = 1 - 3$) anions.” *J. Chem. Phys.* **108** (1998) 10018–10026.
- Thoma, M. L., Kaschow, R., & Hindelang, F. J. “A multiple-reflection cell suited for absorption measurements in shock tubes.” *Shock Waves* **4** (1994) 51–53.
- Thorburn, J. A., Hobbs, L. M., McCall, B. J., et al. “Some diffuse interstellar bands related to interstellar C_2 molecules.” *Astrophys. J.* **584** (2003) 339–356.
- Tielens, A. G. G. M. & Hagen, W. “Model calculations of the molecular composition of interstellar grain mantles.” *Astron. Astrophys.* **114** (1982) 245–260.
- Tran, T. D., Rednyk, S., Kovalenko, A., et al. “Formation of H_2O^+ and H_3O^+ cations in reactions of OH^+ and H_2O^+ with H_2 : Experimental studies of the reaction rate coefficients from $T = 15$ to 300 K.” *Astrophys. J.* **854** (2018) 25.
- Trumpler, R. J. “Preliminary results on the distances, dimensions and space distribution of open star clusters.” *Lick Observatory Bulletins* **14** (1930) 154–188.
- Tulej, M., Kirkwood, D., Pachkov, M., et al. “Gas-phase electronic transitions of carbon chain anions coinciding with diffuse interstellar bands.” *Astrophys. J. Lett.* **506** (1998) L69.
- Ubachs, W., Hinnen, P. C., & Reinhold, E. “Observation of inter-Rydberg transitions in H_2 coinciding with diffuse interstellar bands.” *Astrophys. J.* **476** (1997) L93–L96.
- Valencic, L. A., Clayton, G. C., & Gordon, K. D. “Ultraviolet extinction properties in the Milky Way.” *Astrophys. J.* **616** (2004) 912–924.
- van der Tak, F. F. S. & van Dishoeck, E. F. “Limits on the cosmic-ray ionization rate toward massive young stars.” *Astron. Astrophys.* **358** (2000) L79–L82.
- van der Werf, P. P., Isaak, K. G., Meijerink, R., et al. “Black hole accretion and star formation as drivers of gas excitation and chemistry in Markarian 231.” *Astron. Astrophys.* **518** (2010) L42.
- van der Zwet, G. P. & Allamandola, L. J. “Polycyclic aromatic hydrocarbons and the diffuse interstellar bands.” *Astron. Astrophys.* **146** (1985) 76–80.
- van Dishoeck, E. F. & Black, J. H. “Comprehensive models of diffuse interstellar clouds — Physical conditions and molecular abundances.” *Astrophys. J. Suppl. S.*

- 62** (1986) 109–145.
- van Dishoeck, E. F., Herbst, E., & Neufeld, D. A. “Interstellar water chemistry: From laboratory to observations.” *Chem. Rev.* **113** (2013) 9043–9085.
- van Winckel, H., Cohen, M., & Gull, T. R. “The ERE of the ‘Red Rectangle’ revisited.” *Astron. Astrophys.* **390** (2002) 147–154.
- Vázquez-Semadeni, E. “Are there phases in the ISM?” *EAS Publications Series* **56** (2012) 39–49.
- Verbraak, H., Verdes, D., & Linnartz, H. “A systematic study of ion and cluster ion formation in continuous supersonic planar plasma.” *Int. J. Mass Spectrom.* **267** (2007) 248–255.
- Vos, D. A. I., Cox, N. L. J., Kaper, L., et al. “Diffuse interstellar bands in upper Scorpius: probing variations in the DIB spectrum due to changing environmental conditions.” *Astron. Astrophys.* **533** (2011) A129.
- Walker, G. A. H. “Photoelectric measures of the 4430 Å diffuse interstellar band.” *Mon. Not. R. Astron. Soc.* **125** (1962) 141–167.
- Walker, G. A. H., Bohlender, D. A., Maier, J. P., et al. “Identification of more interstellar C_{60}^+ bands.” *Astrophys. J.* **812** (2015) L8.
- Walker, G. A. H., Campbell, E. K., Maier, J. P., et al. “Gas-phase absorptions of C_{60}^+ : A new comparison with astronomical measurements.” *Astrophys. J.* **831** (2016) 130.
- Walker, G. A. H., Campbell, E. K., Maier, J. P., et al. “The 9577 and 9632 Å diffuse interstellar bands: C_{60}^+ as carrier.” *Astrophys. J.* **843** (2017) 56.
- Walsh, A., Zhao, D., Ubachs, W., et al. “Optomechanical shutter modulated broadband cavity-enhanced absorption spectroscopy of molecular transients of astrophysical interest.” *J. Phys. Chem. A* **117** (2013) 9363–9369.
- Watson, J. K. G. “Assignment of the λ 1369.13 diffuse interstellar absorption band and three other far-ultraviolet interstellar absorption lines to the CH molecule.” *Astrophys. J.* **555** (2001) 472–476.
- Wegner, W. “The total-to-selective extinction ratio determined from near IR photometry of OB stars.” *Astron. Nachr.* **324** (2003) 219–237.
- Wehres, N., Romanzin, C., Linnartz, H., et al. “ C_2 emission features in the Red Rectangle.” *Astron. Astrophys.* **518** (2010) A36.
- Weinreb, S., Barrett, A. H., Meeks, M. L., et al. “Radio observations of OH in the interstellar medium.” *Nature* **200** (1963) 829–831.
- Welty, D. E. & Hobbs, L. M. “A high-resolution survey of interstellar K I absorption.” *Astron. Astrophys. Suppl. Ser.* **133** (2001) 345–393.
- Western, C. “PGOPHER (version 8.0), a Program for Simulating Rotational Structure.” (2014).
- Wheeler, M. D., Newman, S. M., Orr-Ewing, A. J., et al. “Cavity ring-down spectroscopy.” *J. Chem. Soc., Faraday Trans.* **94** (1998) 337–351.
- White, J. U. “Long optical paths of large aperture.” *J. Opt. Soc. Am.* **32** (1942) 285.
- Wolfire, M. G., McKee, C. F., Hollenbach, D., et al. “Neutral atomic phases of the

- interstellar medium in the galaxy.” *Astrophys. J.* **587** (2003) 278–311.
- Wooden, D. H., Charnley, S. B., & Ehrenfreund, P. *Composition and evolution of interstellar clouds*, 33–66 (2004) .
- Wyrowski, F., Menten, K. M., Güsten, R., et al. “First interstellar detection of OH⁺.” *Astron. Astrophys.* **518** (2010) A26.
- Yuan, H. B. & Liu, X. W. “Detections of diffuse interstellar bands in the SDSS low-resolution spectra.” *Mon. Not. R. Astron. Soc.* **425** (2012) 1763–1771.
- Zagury, F. “Analysis of the Schmidt, Cohen & Margon (1980) features in the Red Rectangle nebula.” *The Open Astronomy Journal* **2** (2009) 26–38.
- Zhao, D., Haddad, M. A., Linnartz, H., et al. “C₆H and C₆D: Electronic spectra and Renner-Teller analysis.” *J. Chem. Phys.* **135** (2011a) 044307.
- Zhao, D., Haddad, M. A., Linnartz, H., et al. “Structure determination of the nonlinear hydrocarbon chains C₉H₃ and C₁₁H₃ by deuterium labeling.” *J. Chem. Phys.* **135** (2011b) 074201.
- Zhao, D., Wehres, N., Linnartz, H., et al. “Electronic spectra and molecular geometry of the non-linear carbon chain C₉H₃.” *Chem. Phys. Lett.* **501** (2011c) 232–237.
- Zhao, D., Linnartz, H., & Ubachs, W. “The electronic spectrum of the C_s-C₁₁H₃ radical.” *J. Chem. Phys.* **136** (2012) 054307.
- Zhao, D., Galazutdinov, G. A., Linnartz, H., et al. “Detection of OH⁺ in translucent interstellar clouds: New electronic transitions and probing the primary cosmic ray ionization rate.” *Astrophys. J. Lett.* **805** (2015) L12.
- Zhou, Z., Sfeir, M. Y., Zhang, L., et al. “Graphite, tubular PAHs, and the diffuse interstellar bands.” *Astrophys. J.* **638** (2006) L105–L108.

Summary

This year, 2019, marks the centenary of the discovery of the diffuse interstellar bands or DIBs. The origin of these circa 500 absorption features which appear in the spectra of starlight through interstellar clouds of dust and gas have since eluded the understanding of many astronomers. Through the years, various proposals for the absorbers or ‘carriers’ that cause the DIBs have been put forth, from microscopic dust particles to molecules both large and small. The strongest contenders among these candidates include families of long carbon chains and rings, polycyclic aromatic hydrocarbons (PAHs), and fullerenes. This consensus has resulted from the collective effort of astronomers, experimentalists, theorists, and modelers. In 2015, two (to five) DIBs were attributed to the buckminsterfullerene cation C_{60}^+ , which was confirmed recently in space-based observations. This development breathes new life into DIB research and leads us closer to the next piece to the puzzle.

In this thesis, the electronic spectra of carbon chains are measured and analyzed in the laboratory, and the abundance of molecules in the diffuse interstellar regions of our Galaxy is quantified to provide some insight on the nature of the DIB carriers and of the environments where they are found.

Chapter 2 describes the experimental techniques that were employed in recording spectra specific to the study of carbon-chain radicals. These are namely Incoherent Broadband Cavity-Enhanced Absorption Spectroscopy (IBBCEAS) and Cavity Ring-Down Spectroscopy (CRDS). The two methods are used in a complementary fashion; combining the advantage of the fast data acquisition and wide wavelength coverage of IBBCEAS together with the high resolution of CRDS ensures an efficient search and identification of [new] spectral features that may be directly compared with astronomical DIB spectra. Details on the synthesis of molecules through hydrocarbon plasma expansions are also provided.

Chapters 3 and 4 focus on the hexatriynyl radical, C_6H and its heavier isotopologue, $^{13}C_6H$. The C_6H carbon chain was first found in space before its spectra was even recorded in the laboratory using millimeter-wave spectroscopy. Despite failing the criteria for a DIB carrier, the electronic spectrum of this molecule is rich with information unraveled using high-resolution CRDS which can nevertheless provide

insight on how, for instance, band profiles can change with subtle intramolecular interactions. In these chapters, the electronic origin band of $^{13}\text{C}_6\text{H}$ is reported, and an extensive energy level scheme for C_6H is formulated on the basis of rovibronic assignments and literature data (mm-wave, matrix isolation, and hollow-cathode spectra, ab-initio calculations, and isotopic substitution). Additionally, a Renner-Teller analysis is invoked to explain and assign the different electronic transitions.

Finally, in Chapter 5, electronic transitions of the hydroxyl cation OH^+ are searched for in astronomical spectra from the ESO Diffuse Interstellar Bands Large Exploration Survey (EDIBLES). The interstellar abundance of OH^+ is quantified and from this the rate of cosmic-ray ionization (CRI) in diffuse-translucent clouds is inferred. This quantity is especially important for modeling the chemical evolution of various interstellar species in these environments which may well include the molecular DIB carriers. It is found that the rates are higher than what was previously derived through submillimeter, infrared, and UV observations. This is due to a revised formulation of the OH^+ abundance – CRI rate relation using updated oscillator strength values for the OH^+ transitions. It is possible, however, that these sightlines have inherently high concentrations of OH^+ , and thus, lead to a high rate of CRI derived. Nevertheless, the results serve as a complementary check to other methods of deriving the CRI rate, using ground-based observations of multiple OH^+ transitions in the UV.

All in all, the identification of the DIB carriers is as important as ever, now that C_{60}^+ has, thus far, withstood scrutiny as a candidate. Pinning down the identity of the DIB carriers may shed light on our Galactic carbon budget as several of the accumulated DIB studies point to carbon-based species. Thus, having a fast and sensitive spectrometer to survey various carbon-based gas mixtures will definitely aid in screening potential candidates. High-resolution spectra will also be useful for learning more about the molecule, and spectroscopic constants derived from it can be used for simulating absorption features under interstellar conditions. Lastly, other known molecules can be used as probes for the physi-chemical properties of DIB carrier environments.

As we try to unravel the nature of DIBs, we try to unravel the properties of the interstellar medium of our Galaxy.

Samenvatting

Het jaar 2019 markeert het eeuwfeest van de ontdekking van de diffuse interstellaire bands of DIB's. De oorsprong van deze circa 500 absorptiesignalen die zichtbaar zijn in de spectra van sterrenlicht dat interstellaire wolken van gas en stof doorkruist zijn sindsdien een raadsel gebleven voor astronomen. Door de jaren heen zijn er verschillende voorstellen gedaan voor de absorbers of 'dragers' die de DIB's veroorzaken, van microscopische stofdeeltjes tot moleculen, zowel groot als klein. De meest waarschijnlijke dragers onder deze kandidaten zijn families met lange koolstofketens en ringen, polycyclische aromatische koolwaterstoffen (PAK's) en fullerenen. Deze consensus is het resultaat van de gezamenlijke inspanning van astronomen, experimentalisten, theoretici en modelleerders. In 2015 werden twee (tot vijf) DIB's toegeschreven aan het buckminsterfullerene-kation C_{60}^+ , dat onlangs werd bevestigd middels waarnemingen vanuit de ruimte. Deze ontwikkeling blaast het DIB-onderzoek nieuw leven in en brengt ons dicht bij het volgende stuk van de puzzel.

In dit proefschrift worden de elektronische spectra van koolstofketens gemeten en geanalyseerd in het laboratorium om verder inzicht te verschaffen in de aard van de DIB-dragers en van de omgevingen waar ze zich bevinden.

Hoofdstuk 2 beschrijft de experimentele technieken die zijn gebruikt bij het opnemen van spectra specifiek voor de studie van radicale koolstofketens. Dit zijn namelijk Incoherent Broadband Cavity-Enhanced Absorption Spectroscopy (IBBCEAS) en Cavity Ring-Down Spectroscopy (CRDS). De twee methoden worden op een complementaire manier gebruikt; de snelle gegevensacquisitie en grote golflengtedekking van IBBCEAS samen met de hoge resolutie van CRDS zorgen voor een efficiënte werkwijze en identificatie van [nieuwe] spectrale kenmerken die direct kunnen worden vergeleken met astronomische DIB-spectra. Tevens worden details over de synthese van moleculen in koolwaterstof plasma expansies verkregen.

Hoofdstukken 3 en 4 richten zich op het hexatriynylradicaal, C_6H en zijn zwaardere isotopoloog, $^{13}C_6H$. Deze C_6H koolstofketen werd voor het eerst in de ruimte gevonden zelfs voordat de spectra in het laboratorium werden gemeten met millimetergolf-spectroscopie. Ondanks het feit dat de spectra niet voldoen aan de criteria voor een DIB-drager, zijn de elektronische spectra van dit molecuul rijk aan informatie. Deze

is ontrafeld met behulp van CRDS met hoge resolutie, en biedt inzicht in hoe bijvoorbeeld bandprofielen kunnen veranderen als gevolg van subtiele intramoleculaire interacties. In deze hoofdstukken wordt de elektronische oorsprongsband van $^{13}\text{C}_6\text{H}$ gerapporteerd en een uitgebreid energieniveauschema voor C_6H geformuleerd op basis van rovibronische toewijzingen en literatuurgegevens (mm-golf, matrix isolatie en holle-kathodespectra, ab-initio-berekeningen en isotoop substitutie). Bovendien wordt een Renner-Teller-analyse beschreven om de verschillende elektronische overgangen uit te leggen en toe te wijzen.

Tenslotte worden in hoofdstuk 5 elektronische overgangen van het hydroxylkation OH^+ gezocht in astronomische spectra uit het ESO Diffuse Interstellar Bands Large Exploration Survey (EDIBLES). De interstellaire abundantie van OH^+ wordt gekwantificeerd en daaruit wordt de efficiëntie van kosmisch-straal ionisatie (CRI) in transparante interstellaire wolken afgeleid. Deze parameter is vooral belangrijk voor het modelleren van de chemische evolutie van verschillende interstellaire moleculen in deze omgevingen, waaronder de moleculaire DIB-dragers. Het is gebleken dat de percentages hoger zijn dan wat eerder was afgeleid door submillimeter, infrarood en UV-waarnemingen. Dit komt door een herziene formulering van de OH^+ abundantie in verband met een CRI-efficiëntierelatie met behulp van bijgewerkte oscillatorsterktewaarden voor de OH^+ overgangen. Het is echter mogelijk dat deze zichtlijnen inherent hoge concentraties van OH^+ hebben en dus leiden tot een hoog percentage CRI. Desalniettemin dienen de resultaten als een complementaire controle op andere methoden voor het afleiden van de CRI-efficiëntie die afgeleid zijn van op grond gebaseerde waarnemingen van meervoudige OH^+ overgangen in het UV.

Al met al is de identificatie van de DIB-dragers net zo belangrijk als voorheen, zeker nu C_{60}^+ een DIB drager lijkt te zijn. De identificatie van de DIB-dragers kan licht werpen op ons Galactische koolstofbudget, omdat meerdere van de DIB onderzoeken duiden op DIB dragers met een koolstof basis. Het gebruik van een snelle en gevoelige spectrometer om verschillende koolstofgebaseerde gasmengsels te onderzoeken, zal dus zeker helpen bij het screenen van potentiële kandidaten. Hoge-resolutiespectra zullen ook nuttig zijn om meer over het molecuul zelf te leren, en spectroscopische constanten die daarvan zijn afgeleid, kunnen worden gebruikt voor het simuleren van spectra voor verschillende interstellaire omstandigheden. Ten slotte kunnen andere bekende moleculen worden gebruikt als probes voor de fysi-chemische eigenschappen van DIB-drageromgevingen.

In ons streven om de oorsprong van DIBs te ontrafelen, kunnen we gelijktijdig meer leren over het interstellaire medium in onze Melkweg.

List of publications

The following papers are included in this thesis:

- **The B²Π – X²Π electronic origin band of ¹³C₆H**
Bacalla, X., Zhao, D., Salumbides, E. J., Haddad, M. A., Linnartz, H., and Ubachs, W.
Journal of Molecular Spectroscopy **308–309** (2015) 41–44.
CHAPTER 3
- **Spectroscopic survey of electronic transitions of C₆H, ¹³C₆H, and C₆D**
Bacalla, X., Salumbides, E. J., Linnartz, H., Ubachs, W., and Zhao D.
The Journal of Physical Chemistry A **120** (2016) 6402–6417.
CHAPTER 4
- **The EDIBLES survey IV. Cosmic ray ionization rates in diffuse clouds from near-ultraviolet observations of interstellar OH⁺**
Bacalla, X. L., Linnartz, H., Cox, N. L. J., Cami, J., Roueff, E., Smoker, J. V., Farhang, A., Bouwman, J., and Zhao, D.
Astronomy and Astrophysics **622** (2019) A31.
CHAPTER 5

The author has also contributed to the writing of:

- **C₆₀⁺ and the diffuse interstellar bands: an independent laboratory check**
Spieler, S., Kuhn, M., Postler, J., Simpson, M., Wester, R., Scheier, P., et al.
The Astrophysical Journal **846** (2017) 168.
- **The ESO Diffuse Interstellar Band Large Exploration Survey (EDIBLES)**
Cami, J., Cox, N. L., Farhang, A., Smoker, J., Elyajouri, M., Lallement, R., et al.
The Messenger **171** (March 2018) 31–36.

Curriculum Vitae

I was born on the 14th day of September, 1989, in the island of Cebu, Philippines. I went to Mabolo Elementary School for my primary education from 1996 to 2002. It was during this time that I had developed an interest in science (which was also reinforced by a visit to a brief and temporary science exhibition / museum in one of the malls in our city). Then I got a scholarship to attend Cebu City National Science High School (2002–2006). Here I did not like mathematics, though I eventually appreciated it by the end of this period and also after learning that it cannot be ignored when one decides to take a science or engineering course for university. After graduating, I was awarded a scholarship from our national department of science and technology, which allowed me to pursue a bachelor's degree in applied physics in the University of San Carlos (USC) (2006–2011). For my thesis, I worked with Dr. Raymund Sarmiento on monitoring ethylene gas emissions in climacteric fruits through photoacoustic spectroscopy, which I did together with Dexter Manalili (who is also currently doing his PhD research here in the Netherlands).

A couple of months after graduation, I stayed in our [laser spectroscopy and interferometry / optics] group as a research assistant. Then I applied as a physics instructor in the same department. For the next two and a half years, I taught introductory physics and laboratory courses to undergraduate students. Within my teaching stint, I managed to acquire a scholarship and pursued a master's degree in physics (2012–2014). I had the opportunity to do my thesis research here in the Netherlands for six months with Dr. Edcel Salumbides (my former teacher in USC) and Prof. dr. Wim Ubachs who both work in the LaserLaB at the VU University Amsterdam. My project was on recording the first-ever spectrum of the $^{13}\text{C}_6\text{H}$ isotopologue, which I adopted for my thesis and defended in USC. This introduced me to the cavity ring-down spectroscopy (CRDS) and its possible applications to astrochemistry, and also to Prof. dr. Harold Linnartz who would be one of my supervisors for my PhD studies.

Harold and Wim have since had a longstanding collaboration on the spectroscopy of carbon-based molecules in relation to the problem of the diffuse interstellar bands (DIBs). Building on my previous MSc work, I succeeded (in November 2014) the then-candidate Dr. Mohammad Ali Haddad as the PhD student working on the CRDS

setup in the LaserLaB, and worked in Amsterdam for the first year of my PhD. During this time I measured electronic spectra of C_6H using the CRD technique and analyzed them with the PGOPHER software, with the help of Edcel and Dr. Dongfeng Zhao. In the laboratory for astrophysics in Leiden, Dongfeng introduced me to the incoherent broadband cavity-enhanced absorption spectroscopy (IBBCEAS) setup from which I measured spectra of other carbon chains such as C_8H and $C_{10}H$. Thus far, I had quite an experience with operating the pinhole and slit plasma discharge nozzles; I worked with Dr. Jordy Bouwman in employing the electron impact ionization source with IBBCEAS. For a good half of my stay in the Observatory, I was also involved in a large consortium of DIB astronomers (i.e., the EDIBLES team, lead by Dr. Nick Cox and Dr. Jan Cami) where I utilized telescope data for deriving the cosmic-ray ionization rates in diffuse interstellar clouds. I have presented all my work on various (inter)national conferences and meetings, and published them in peer-reviewed journals, which are described in this dissertation.

For my next career step, I will go back to the Philippines and help reestablish our optics laboratory in USC, and continue to teach physics.

Acknowledgments

If you found yourself reading this part of the thesis first, then you are excused. After all, this is where you can find the important characters that helped forge this memoir of scientific research and who have contributed immensely to my PhD life (which brought me to defend my thesis—successfully, I hope). Also, I may have forgotten to include your name in the list; please feel free to approach me and I will give you a handshake and/or a hug.

My utmost gratitude goes first to the people of the Netherlands and of the Philippines for enabling me to pursue my studies in physics and astronomy which, otherwise, would not be possible without their hard-earned taxes.

To Harold and Wim, thank you for your guidance and encouragement. Treating me as a colleague who can contribute something to the academic field in which you have both long played an important part is humbling and empowering.

To my direct supervisors, Edcel, Dongfeng, and Jordy, I am grateful for the wisdom you have imparted to me, especially in our musings on spectroscopy and in our experiments in the laboratory.

Many thanks to the staff in both Leiden and Amsterdam who, without hesitation, have always helped me solve my pressing administrative requirements and technical needs: Marjan Balkestein, Evelijn Gerstel, Alexandra Schouten-Voskamp, Yvonne Kluijt, Marja Herronen, Martijn Witlox, Aart Vos, Raymond Koehler, Rob Kortekaas. And to everyone in the FMD, ELD, SCIS, the Observatory Secretariat and Computer Group, thank you all for your support!

Special thanks to Dia Eek, Tugçe Özyurt, and Gerrit Kuik who were instrumental in getting me to the Netherlands for the first time.

I would also like to thank the thesis reading committee for taking the time to review my manuscript (on such a tight schedule), as well as the anonymous reviewers of our publications reproduced in this booklet.

To the group of astronomers who I have worked closely in the production of the OH⁺ paper, and to the whole EDIBLES team, my sincerest thanks for being patient with teaching and guiding me through the process.

Being a member of two research groups with different focus can sometimes be a challenge and may invoke a feeling of being out of place. When I am in the LaserLaB in Amsterdam, I see myself as an astrophysicist surrounded by physicists. On the other hand, in the Laboratory for Astrophysics in Leiden, I am a spectroscopist surrounded by chemists and astronomers. However, this meant that I got to talk to and hear the perspectives of my colleagues from seemingly diverse fields which only enriched my learning experience. For this I am grateful for my fellow PhD students and postdocs who have shared their thoughts and their time with me. The same goes for my colleagues especially in the field of spectroscopy who I've met in various (inter)national conferences, I thank you all for the interesting discussions and fun times. And to those that I have worked with in my experiments in both the CRDS and BB-DIB setup, thank you! (I won't mention all their names for there are quite a lot of them that have since come and gone all throughout my PhD life.)

To the small group of friends that I have accumulated here in Leiden, from the art club, from the physics department, and my neighbors, I thank you for the camaraderie, and may our paths cross again.

Living alone in a foreign land has never been too hard of an ordeal, thanks to all my friends from home who never missed a chance to keep in touch. To JC, Sam, and Mike (and to all my online chat-mates) and to those who had the opportunity to visit personally, thank you very much for spending your time with me. To Therese, thank you for your patience and understanding.

I am especially indebted to my surrogate family here in the Netherlands who took good care of me. *Daghang salamat* to the Bisdaks: Adonis, Jane, Edcel, Marian, Albert, and Dexter. Here's to more board game nights, cycling tours, and boating expeditions along the Amstel! And to all members of our Filipino community who have always been warm and accommodating, I cannot thank you enough.

Lastly, and most importantly, to Panfilo, Antonette, Gladys, and Gracie, many thanks for supporting me all the way despite knowing that I will be away from home for quite some time. You will always be a part of what I do and what good I will accomplish. I will always love you.

The mystery of the diffuse interstellar bands or DIBs is regarded as the most longstanding problem in the whole of astronomical spectroscopy, baffling scientists since a century ago. In this thesis, the electronic spectra of molecules are measured to better understand the nature of these enigmatic features as well as to characterize the physical properties of the interstellar medium of our Galaxy.

ISBN 1234567890

